2021

Mathematical Modeling Of Cell Migration

Maria Jesus Munoz Lopez
University of Pennsylvania

Mathematical Modeling Of Cell Migration

Abstract

Cell migration is an essential process, involved in immune defense, cancer spread, wound healing, and embryo development. This work presents modeling efforts to understand various mechanisms of cell migration. We first discuss the modeling of bleb-driven cell migration, where the cell membrane detaches from the cytoskeleton and generates a protrusion that is completely devoid of structural proteins. Cell migration in this case is driven essentially by pressure and motor contractility exerted by myosin. I will introduce a stochastic model of bleb-driven migration offering support for theories on blebbing cell polarization and the potential involvement of water channels. We then turn to the involvement of ion channels and ionic electrodiffusion in cell processes, first in cell volume control, and then in cell migration, presenting a model that combines electrodiffusion-driven migration with a mechanical model of actin polymerization.

Degree Type

Dissertation

Degree Name

Doctor of Philosophy (PhD)

Graduate Group

Applied Mathematics

First Advisor

Yoichiro Mori

Subject Categories

Applied Mathematics | Mathematics

MATHEMATICAL MODELING OF CELL MIGRATION

María Jesús Muñoz López

A DISSERTATION

in

Applied Mathematics and Computational Science

Presented to the Faculties of the University of Pennsylvania

in

Partial Fulfillment of the Requirements for the

Degree of Doctor of Philosophy

2021

Supervisor of Dissertation

Yoichiro Mori, Calabi-Simons Chair in Mathematics and Biology

Graduate Group Chairperson

Robin Pemantle, Merriam Term Professor of Mathematics

Dissertation Committee

Yoichiro Mori, Calabi-Simons Chair in Mathematics and Biology

Eleni Katifori, Assistant Professor

Vivek Shenoy, Eduardo D. Glandt President's Distinguished Professor

Dedicated to mi familia.

ACKNOWLEDGEMENTS

I would like to thank my advisor, Professor Yoichiro Mori, for his support and guidance throughout graduate school. I would also like to thank Dr. Hyunjoong Kim, for his help and support with my research. And Dr. Bob Anderssen, my first research mentor and the person who got me into mathematical biology.

ABSTRACT

MATHEMATICAL MODELING OF CELL MIGRATION

María Jesús Muñoz López

Yoichiro Mori

Cell migration is an essential process, involved in immune defense, cancer spread, wound healing, and embryo development. This work presents modeling efforts to understand various mechanisms of cell migration. We first discuss the modeling of bleb-driven cell migration, where the cell membrane detaches from the cytoskeleton and generates a protrusion that is completely devoid of structural proteins. Cell migration in this case is driven essentially by pressure and motor contractility exerted by myosin. I will introduce a stochastic model of bleb-driven migration offering support for theories on blebbing cell polarization and the potential involvement of water channels. We then turn to the involvement of ion channels and ionic electrodiffusion in cell processes, first in cell volume control, and then in cell migration, presenting a model that combines electrodiffusion-driven migration with a mechanical model of actin polymerization.

TABLE OF CONTENTS

LIST OF TABLES

LIST OF ILLUSTRATIONS

CHAPTER 1 : Bleb-driven Migration in 1D

1.1 Introduction

Blebs are cellular protrusions that appear as smooth spherical expansions of the membrane formed when it separates from the underlying acting cortex (see Figure 1.1), driven by hydrostatic pressure generated in the cytoplasm by the contractile actomyosin cortex [34], [8], [56]. They were originally associated with cells undergoing apoptosis, but have also been observed in cytokinesis, and in migrating cells in 2D and 3D. Many cell types can use blebs for motility, including mammalian tumour cells [14], which can use blebs to force their way through the endothelium and invade new tissues, and metastatic cells, which can use blebs to escape anti-tumour treatments that rely on protease inhibitors [8]. Bleb expansion is faster than lamellipodial protrusion, and, since blebs have no cortex, can occur in any direction and adapt to the shape of the extracellular environment. There is also data to suggest that bleb growth requires less energy than lamellipodium formation [8].

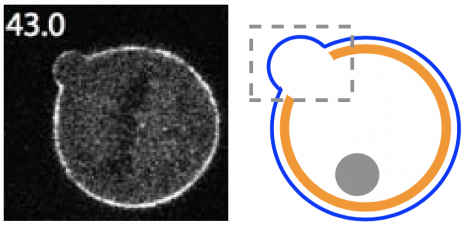

Figure 1.1: Micrograph of a single bleb induced by laser ablation on the surface of a HeLa cell 43 s after initial formation, taken from [1]

The life cycle of the bleb can be divided into three steps: initiation, growth, and retraction (see Figure 1.2). Two mechanisms have been proposed for bleb initiation: a local decrease in membrane-cortex attachment, or a local rupture of the cortex. They could also be functioning together [34]. Both of these have been observed experimentally in both motile and non-motile blebbing cells [8]. The bleb initially appears devoid of filamentous actin, and grows as cytoplasmic fluid fills the protrusion. Bleb inflation is thought to be driven by intracellular pressure transients generated by myosin II contraction of the actin cortex [7].

Over time, the actin cortex reassembles at the bleb plasma membrane, and drives cortex retraction: once expansion ceases, ERM (Ezrin, Radixin, Moesin) proteins (responsible for cortex-membrane adhesion) are recruited to the membrane, followed by actin, actin-bundling proteins, and lastly contractile proteins [7]. In migrating cells, retraction does not always occur, since movement depends on a stable bleb, and instead the cell body moves forward as a result of contraction at the rear of the cell [34]. In such cells, a new bleb often forms after cortex repolymerization under the membrane [8].

Biochemically, cortex composition is dominated by actin, actin-bundling proteins, and myosin II. High myosin II activity is critical for the formation of blebs [40]. The cortex is linked to the membrane by ERM proteins, which can switch from an inactivated closed conformation to an active open conformation that exposes an actin binding site and a membrane-targetting domain [7]. Thus, a decrease in membrane-cortex attachment corresponds to ERM proteins returning to the closed conformation. The actin cortex that remains at the base of the bleb is disassembled by the constitutive turnover of actin [8]. An important question in bleb dynamics is how cortex reassembly begins. One possibility with some experimental support is that cortex assembly is constitutive, but slow compared to bleb expansion, so that it can only catch up when the expansion slows down [7].

An important aspect of bleb initiation and growth is that it can be localized to just a part of the cell, so that different parts of the cell can be mechanically isolated (as they often are chemically) [6]. The precise mechanisms that determine where a bleb is initiated during migration are not known. However, observations suggest that asymmetries in the membrane-cortex attachment could play a role in determining the cell front: in Walker carcinosarcoma cells, the level of Ezrin (a member of the ERM family) is elevated at the back of the cell, and reduced at the leading edge, facilitating bleb formation in the front of the cell [8], [39]. A similar idea is localized water uptake, mediated by polarized distribution of aquaporins, but there is no direct experimental evidence of this [34]. In any case, it is also unclear what the signals are that tell the cell to begin any such polarization, and it appears

that the stimuli leading to blebbing motility are cell-specific [8]. Pure bleb-driven movement can be brought about by mechanical resistance: cells may sense mechanical resistance and use a signaling mechanism to alter the balance between actin polymerization and myosin contractility, increasing the pressure in the cell and favouring the formation of blebs [56]. It has also been observed to be strongly chemotactic [56], [2]. In Zebrafish Primordial Germ Cells, experiments have shown that external gradients of lysophosphatidic acid (LPA) can trigger directional cell polarization by inducing an asymmetric contraction of the cortical cytoskeleton [39].

Bleb-driven migration requires the bleb to be stable for some time, or repeated blebbing. [56] observed that cells often bleb at areas of negative membrane curvature, often on the flanks of earlier blebs, which could be the result of negative curvature producing membrane stress. This is in agreement with [6], who found no strong predictors of expansion or retraction at a site where a bleb had already ocurred, but increase probability of blebbing on the sides of a previous bleb.

In [39], the concept of a stable-bleb is presented: these are blebs which do not heal immediately, but persist for a longer time before retracting. Their results support a mechanical model of stochastic cell polarization based on the amplification of local fluctuations in cortical contractility and a positive feedback mechanism between contractility gradients and continuous cortical flows maintaining polarity in stable-bleb cells.

In extreme cases, blebs give rise to a traveling wave around the cell periphery known as 'circus movement' [6]. This traveling behavior occurs via a simple modification of bleb dynamics: once a bleb forms, an actin cortex is thought to reform asymmetrically, so that when retraction starts, the cytosol is forced into the unconsolidated side of the bleb. This propagates because one side of the bleb is always older than the other, and as it retracts, if forces cytosol into the younger side, promoting further rupture.

Understanding bleb formation and bleb-driven travel is important as treatments are

developed for pathologies where cells may employ this type of migration, such as cancer [8] and immune defficiencies. As a systemic organ, the immune system depends on the continuous movement of cells among different anatomic sites [9], [13]. Newly generated lymphocytes need to travel from the thymus or bone marrow into the blood, and enter the major lymph nodes. When a T-cell enters a lymph node, it looks for antigens to bind to. If no such antigens are found, the T-cell egresses back to the blood. A congenital immunodeficiency, termed X-linked Moesin-Associated Immunodeficiency Disorder (XMAID) has been observed, where a mutation prevents T-cell egress back into the blood. Experiments carried out by the Burkhardt lab at the Children's Hospital of Philadelphia showed that in the presence of S1P, T-cells in the process of exiting a lymph node form blebs, that become the leading edge of the migrating cell [38]. In the experiments, blebbing in wild-type cells was seen to be localized to the leading edge, while in the cells of XMAID affected mice blebbing occurred anywhere around the cell surface, with lower intensity at the rear of the cell. Mutant cells did not have directionality or much displacement, as they blebbed randomly. The precise mechanics of this are not well understood and questions arise such as whether it is possible to explain the motile behavior based on random blebbing except where ERM proteins coat the membrane; or the origin of the pressure that causes the blebs to form.

Theoretical models of blebbing have attempted to capture various aspects of the blebbing process. [26] presents a model of bleb formation and healing that considers the kinetics of the turnover of adhesion proteins through the bleb cycle. Their model allows for the study of the determinants of bleb formation and retraction, but is set up so that the cell membrane and cortex have a fixed reference position, so that there is no net travel. Further, in their model, bleb formation is not spontaneous and requires an externally applied perturbation. On the other hand, [47] and [48] consider a mechanical model in 2D using computational fluid dynamics to understand the initial bleb formation and expansion phase during which cytosolic fluid moves after the expanding membrane. Their model considers the mechanics of the system, but lack the adhesion kinetics, so that the bleb never retracts and the cell cannot travel.

However, a description of cell movement driven by blebs is lacking. Here, we combine the turnover model of [26] with a simple mechanical model that has no reference location, so that the cell travels and we can consider the cell's motion as well as the dynamics of bleb formation. Moreover, our model allows for the formation of spontaneous blebs by incorporating stochasticity into the system. We can then study cell travel in a system that can bleb repeatedly without the need to manually introduce perturbations or periodicity.

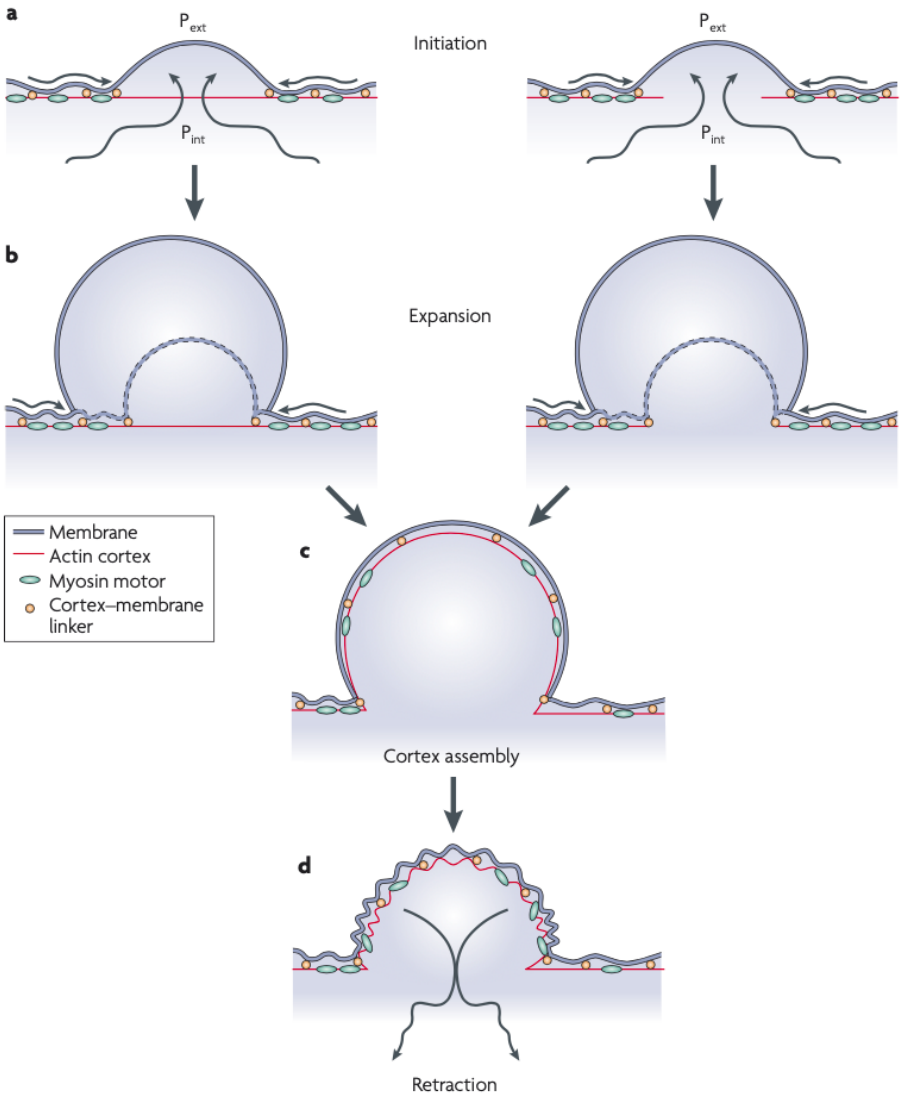

Figure 1.2: The bleb life cycle (reproduced from [8]). The bleb life cycle can be subdivided into three phases: bleb initiation (nucleation), expansion, and retraction. **a** Bleb initiation can result from a local detachment of the cortex from the membrane (left model) or from a local rupture of the cortex (right model). **b** Hydrostatic pressure in the cytoplasm (P_{int}) then drives the membrane expansion by propelling cytoplasmic fluid through the remaining cortex (left model) or through the cortex hole (right model). Concomitantly, the membrane can detach further from the cortex, increasing the diameter of the bleb base (dashed line). **c** As bleb expansion slows down, a new actin cortex reforms under the bleb membrane. **d** Recruitment of myosin to the new cortex is followed by bleb retraction. P_{ext}, extracellular hydrostatic pressure.

1.2 Deterministic Model Formulation

Consider a bounded interval over which the cell lies $x_m^b < x < x_m^f$, where x_m^f is the front membrane position and x_m^b is the back membrane position. In the intracellular region between these two points, the unknowns are the fluid velocity u and hydrostatic pressure p, which we will assume to be spatially constant. Other unknown quantities are the adhesion density a, cortex thickness c, the cortical positions at the front and back $x_c^{f,b}(t)$, and the nucleus location $x_N(t)$. The adhesion and cortex densities (a and c), are defined at the front and back of the cell, denotes a^f, a^b, c^f, c^b. A schematic diagram for our model is given in Figure 1.3.

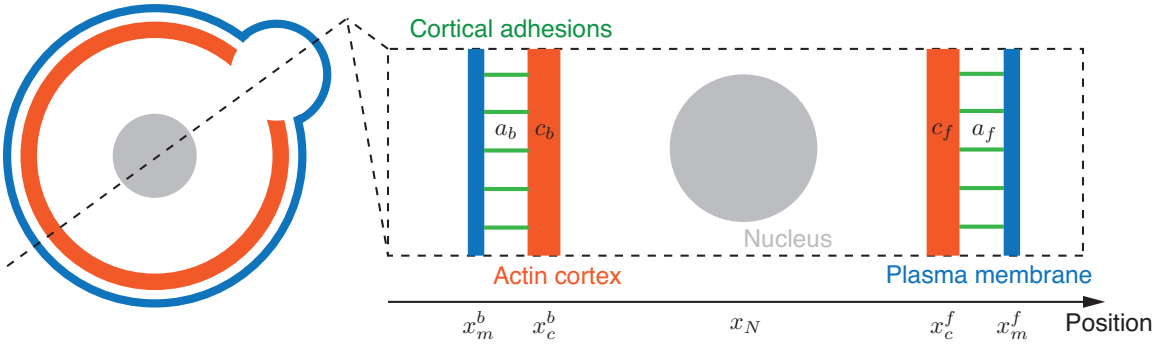

Figure 1.3: Schematic of system.

1.2.1. Assembly and Turnover

We model the cortex thickness c, following [26], assuming simple first-order kinetics,

$$\frac{\partial c}{\partial t} = \omega a - rc, \tag{1.1}$$

where ω governs cortex assembly, and assumes that new cortex requires adhesion to a nearby membrane. The second term describes cortex turnover, with rate r. In this context, c is interpreted as a combination of density and spatial thickness, with arbitrary units.

The cortex is attached to the membrane via exrin-radixin-moesin (ERM) proteins. We refer to the effect of these proteins as "adhesions". We use the model of [26], with similar first-order kinetics for the adhesion assembly and turnover, and three additional assumptions: 1) adhesion assembly saturates at high cortex thickness; 2) adhesion attachment requires proximity between cortex and membrane, with characteristic distance δ, that describes the "reach" of the adhesion molecules; and 3) adhesion detachment is force dependent, with characteristic breaking force f_0. These considerations lead to

$$\frac{\partial a}{\partial t} = \frac{k_{on} c}{c_0 + c} \exp\left(\frac{-|x_m - x_c|}{\delta}\right) - k_{off} a \exp\left(\frac{\kappa |x_m - x_c|}{f_0}\right), \tag{1.2}$$

where k_{on} and k_{off} are the adhesion assembly and turnover rates respectively, and c_0 is the cortex thickness at which adhesion assembly is half-maximal. The numerator $\kappa|x_m - x_c|$ follows from the assumption that adhesions collectively behave like springs with Hookean stiffness κ. Note that adhesion turnover is significantly faster than cortex turnover, leading to a separation of timescales.

Equations 1.1 and 1.2 are the same at the front and back of the cell, with the appropriate superscripts.

1.2.2. Mechanics

Inside the cell, we use Darcy's law for the velocity field:

$$-\frac{\partial p}{\partial x} - \xi u = 0, \tag{1.3}$$

and u is constant in x by incompressibility. Here, ξ is the ratio of dynamic viscosity and permeability. We impose the following boundary conditions at x_m^f and x_m^b:

$$p - (p_\infty + d_g u) = a^f \kappa (x_m^f - x_c^f) + \kappa_m (x_m^f - x_N - l), \tag{1.4}$$

$$p - (p_\infty - d_g u) = -a^b \kappa (x_m^b - x_c^b) - \kappa_m (x_m^b - x_N + l), \tag{1.5}$$

where l is the membrane rest length, p_∞ is the pressure far from the cell, d_g is a drag coefficient, and the force between the membrane and the nucleus is modeled as a Hookean spring with spring constant κ_m with a natural length of l. The drag coefficient d_g as specified above represents the resistance of the exterior fluid to flow, and was used previously in [55]. The force between the membrane and the cortex reflects the spring-like force exerted by the adhesions. The above equations state that the difference in pressure across the membrane at the front is balanced by the adhesion and membrane forces.

At the front and back membranes, we also impose the following conditions:

$$\frac{\partial x_m^f}{\partial t} - u = -\zeta [p]^f, \tag{1.6}$$

$$\frac{\partial x_m^b}{\partial t} - u = \zeta [p]^b. \tag{1.7}$$

The difference in the membrane velocity $dx_m^{f,b}/dt$ and the fluid velocity u is given by the transmembrane water flow. This transmembrane water flow in turn is proportional to the difference in pressure across the membrane interface as given in 1.4 and (1.5), where ζ is the water permeability coefficient.

At the cortex, we have the following force balance equations:

$$\eta_c c^f \frac{\partial x_c^f}{\partial t} = a^f \kappa (x_m^f - x_c^f) - \sigma c^f (x_c^f - x_N - \beta), \tag{1.8}$$

$$\eta_c c^b \frac{\partial x_c^b}{\partial t} = a^b \kappa (x_m^b - x_c^b) - \sigma c^b (x_c^b - x_N + \beta). \tag{1.9}$$

Here, we have assumed that the cortex experiences a drag force with respect to the underlying substrate, whose strength is proportional of the cortical density $c^{f,b}$. This drag force is balanced by the adhesion forces between the cortex and membrane and the force between the nucleus and cortex. The force between the nucleus and cortex is modeled as a spring force proportional whose spring constant is the cortical density $c^{f,b}$. The proportionally constant σ may be viewed as the strength of actomyosin contractility

Table 1.1: Model Parameters

Symbol	Dimensions	Meaning
ω	(A.U.) μm^2 s^{-1}	cortex assembly rate constant
r	s^{-1}	cortex turnover rate constant
k_{on}	μm^{-2}s^{-1}	adhesion assembly rate
k_{off}	s^{-1}	adhesion turnover rate
c_0	(A.U.)	cortex thickness at half-maximal adhesion
δ	μm	adhesion length between cortex and membrane
κ	pN μm^{-1}	adhesion spring constant
f_0	pN	adhesion breaking strength
p_∞	Pa	pressure far from the cell
ξ	Pa s μm^{-2}	ratio of dynamic viscosity and permeability
κ_m	Pa μm^{-1}	hydrostatic pressure scale
d_g	Pa s μm^{-1}	fluid drag constant
ζ	μm s^{-1}Pa^{-1}	water permeability constant
σ	Pa (A.U)$^{-1}$ μm^{-1}	actin-myosin contractility
β	μm	cortex rest length
l	μm	membrane rest length
η_c	Pa s μm^{-1} (A.U)$^{-1}$	cortex drag factor
η_N	Pa s μm^{-1}	nucleus drag factor

The position of the cell nucleus is given by

$$\eta_N \frac{\partial x_N}{\partial t} = \kappa_m(x_m^f - x_N - l) + \kappa_m(x_m^b - x_N + l) + \sigma c^f (x_c^f - x_N - \beta) + \sigma c^b (x_c^b - x_N + \beta) \quad (1.10)$$

where the nucleus is assumed to experience a drag force with respect to the substrate with the drag coefficient η_N.

Physical parameters are summarized in Table 1.1.

1.2.3. Preliminary Analysis

First, we can simplify the fluid equations as follows. Set $p_\infty = 0$. Since u is constant in x, $p(x)$ is linear. Then, subtracting equations (1.5) - (1.4), we get that

$$\left(2d_g + \xi(x_m^f - x_m^b)\right) u = -a^f \kappa(x_m^f - x_c^f) - a^b \kappa(x_m^b - x_c^b) - \kappa_m(x_m^f - x_N - l) - \kappa_m(x_m^b - x_N + l) \tag{1.11}$$

We non-dimensionalize the system choosing characteristic cortex thickness $c_c = c_0$, characteristic density of adhesions $a_c = \frac{k_{on}}{k_{off}}$, characteristic time $t_c = \frac{1}{r} \sim 10$ s [16], characteristic length $l_c = l \sim 10$ μm [50], characteristic pressure $p_c = \kappa_m l$ ($\kappa_m \sim 100$ Paμm^{-1} [6]), and characteristic fluid velocity $u_c = lr$. This results in the non-dimensional system 1.12 - 1.19.

$$\frac{\partial c}{\partial t} = \Omega a - c \tag{1.12}$$

$$\epsilon \frac{\partial a}{\partial t} = \frac{c}{1+c} \exp\left(\frac{-|x_m - x_c|}{D}\right) - a \exp\left(\frac{|x_m - x_c|}{F}\right) \tag{1.13}$$

$$\left(2D_g + \chi(x_m^f - x_m^b)\right) u = -a^f(x_m^f - x_c^f) - a^b(x_m^b - x_c^b) - K_m(x_m^f - x_N - 1) - K_m(x_m^b - x_N + 1) \tag{1.14}$$

$$\gamma_m \left(\frac{\partial x_m^f}{\partial t} - u\right) = -a^f(x_m^f - x_c^f) - K_m(x_m^f - x_N - 1) \tag{1.15}$$

$$\gamma_m \left(\frac{\partial x_m^b}{\partial t} - u\right) = -a^b(x_m^b - x_c^b) - K_m(x_m^b - x_N + 1) \tag{1.16}$$

$$\gamma_c c^f \frac{\partial x_c^f}{\partial t} = a^f(x_m^f - x_c^f) - M c^f(x_c^f - x_N - b) \tag{1.17}$$

$$\gamma_c c^b \frac{\partial x_c^b}{\partial t} = a^b(x_m^b - x_c^b) - M c^b(x_c^b - x_N + b) \tag{1.18}$$

$$\gamma_N \frac{\partial x_N}{\partial t} = K_m(x_m^f - x_N - 1) + K_m(x_m^b - x_N + 1) + M c^f(x_c^f - x_N - b) + M c^b(x_c^b - x_N + b) \tag{1.19}$$

with 12 non-dimensional parameters defined in Table 1.2. Note that we use the same labels for all quantities for simplicity, but these are now non-dimensional. Many of the parameters

were already estimated in [26]. For the remaining parameters, we obtain estimates based on matching the cell velocity with that reported in [38]. In subsequent sections, we will vary γ_c and γ_m within a specified range to determine their impact on model behavior. The parameters χ, D_g and γ_N are set to a small positive value as shown in Table 1.2 unless indicated otherwise. Setting D_g and γ_N to 0 does not lead to appreciably different results in our computations. The behavior of the model with respect to larger values of γ_N and D_g will be briefly discussed at the end of Section 1.3.2.

Table 1.2: Nondimensional Parameters

Symbol	Definition	Interpretation	Estimate	Source
Ω	$\frac{\omega k_{on}}{k_{off} r c_0}$	cortex intensity	$6.5 - 100$	[26]
ϵ	$\frac{r}{k_{off}}$	ratio of cortex turnover and adhesion rates	0.1	[26]
D	$\frac{\delta}{l}$	adhesion reach	$0.15 - 0.23$	[26]
F	$\frac{f_0}{l\kappa}$	adhesion bond strength	$1.0 - 6.3$	[26]
K_m	$\frac{k_{off}\kappa_m}{k_{on}\kappa}$	pressure relative to adhesion strength	$0.016 - 0.1$	[26]
M	$\frac{\sigma c_0 k_{off}}{k_{on}\kappa}$	myosin contractility relative to adhesion strength	$0.007 - 0.43$	[26]
D_g	$\frac{d_g r k_{off}}{k_{on}\kappa}$	fluid drag relative to adhesion strength	$10^{-6} - 10^{-11}$	see text
χ	$\frac{\xi r l}{\kappa_m}$	ratio of viscosity and permeability relative to pressure	10^{-6}	see text
b	$\frac{\beta}{l}$	ratio of cortex and cell lengths	$0 - 0.1$	see text
γ_m	$\frac{r k_{off}}{\zeta k_{on}\kappa}$	ratio of cortex turnover rate and mechanical changes rate	$10^{-2} - 10^{-5}$	see text
γ_c	$\frac{\eta_c c_0 r k_{off}}{k_{on}\kappa}$	drag on cortex relative to adhesion strength	$10^{-2} - 10^{-5}$	see text
γ_N	$\frac{\eta_N r k_{off}}{k_{on}\kappa}$	drag on nucleus relative to adhesion strength	10^{-6}	see text

1.3 Deterministic Model Results

The model 1.12 - 1.19 combines the mechanisms of membrane-cortex interaction (force-sensitive adhesion, cortex contractility, cortex turnover) with force balance in the cell (fluid pressure, membrane and cortex tension). Numerical simulations of the model reveal several classes of dynamics: stable non-blebbing states, stationary blebbing, and bleb-driven migration. Note that throughout this section parameters are the same on both sides of the cell. Without loss of generality, we focus on the effect of perturbations from steady state on the front side, which will then be the 'leading edge' of the cell.

For a bleb to form, enough adhesions have to break so that the membrane and cortex will detach. In non-blebbing states, even if all adhesions are removed, the system returns to steady state without the membrane separating enough from the cortex for the cortex to depolymerize before adhesions reappear. This is a monostable regime, in which the system always returns rapidly to steady state following a perturbation. In blebbing states, small perturbations do not suffice for the membrane and cortex to detach, but large enough perturbations will lead to bleb formation.

A sample simulation for the bleb-driven migration case is shown in Figure 1.4, obtained by setting the system to steady state, and generating a perturbation at the front of the cell by removing 50% of the adhesions. When this perturbation is significant (enough adhesions are removed), as in the case shown in Figure 1.4, the remaining adhesions are destroyed, and the cortex depolymerizes. This leads to the membrane detaching from the cortex and protruding. This initial expansion is very rapid compared with the full life cycle of the bleb, in line with measurements [6]. The adhesions subsequently accumulate under the protruding membrane and the cortex is able to reattach and thicken. Cortex contraction then drives the bleb to heal, returning the system to equilibrium. It is important to note that while a and c will return to the same initial steady state after the bleb heals, the positions of the membrane, cortex, and nucleus will have a new steady state. This is because these positions do not have a reference location, but rather a reference distance between the various points

(in other words, any parallel translation of a steady state will yield a steady state). This motile behaviour is distinct from previous modeling efforts in that the bleb formation and healing generate movement - [26], for instance, models the bleb life cycle, but has a reference configuration such that there is no displacement, while [47] considers bleb formation only.

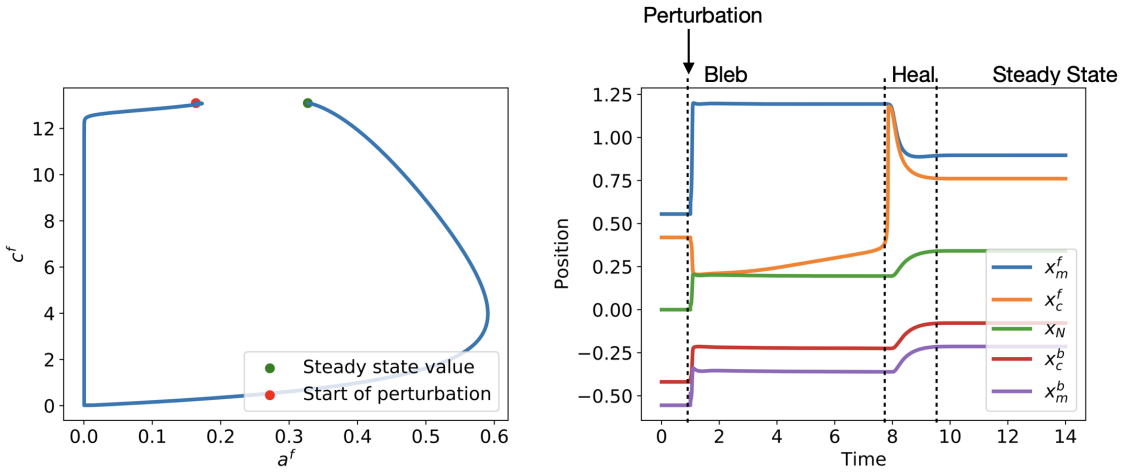

Figure 1.4: Starting at steady state, the system is perturbed by setting $a^f = 0.5 \times a_{ss}^f$, where a_{ss}^f is the value of a^f at steady state. *(left)*: a^f vs c^f trajectory. *(right)*: Membrane, cortex, and nucleus positions. Parameters used here are $\Omega = 40$, $\varepsilon = 0.01$, $D = 0.15$, $F = 0.99$, $M = 0.0081$, $b = 0$, $\gamma_m = 0.8 \times 10^{-3}$, $K_m = 0.1$, $\gamma_N = 10^{-6}$, $\gamma_c = 10^{-4}$, $D_g = 10^{-11}$, $\chi = 10^{-6}$. Time step was set at $\Delta t = 0.0001$.

1.3.1. Model Behaviors

Notably, the blebbing regime can lead to four different behaviors shown in Figure 1.5: bleb formation and healing on the side of the perturbation (Figure 1.5(a)), a bleb forming but never healing (Figure 1.5(b)), a bleb on one side propagating to induce a bleb on the other side (Figure 1.5(c)), or an oscillation where blebs alternate from front to back (Figure 1.5(d)). These behaviors are summarized in Figure 1.6.

We can recover most model behaviours by varying the cortex assembly rate Ω, and the inverse permeability of the cell membrane γ_m. The transitions between behaviours as these parameters are varied is shown in Figure 1.6. We find that larger values of Ω lead to a monostable system, as the cortex reassembly is faster. Increases in γ_m cause

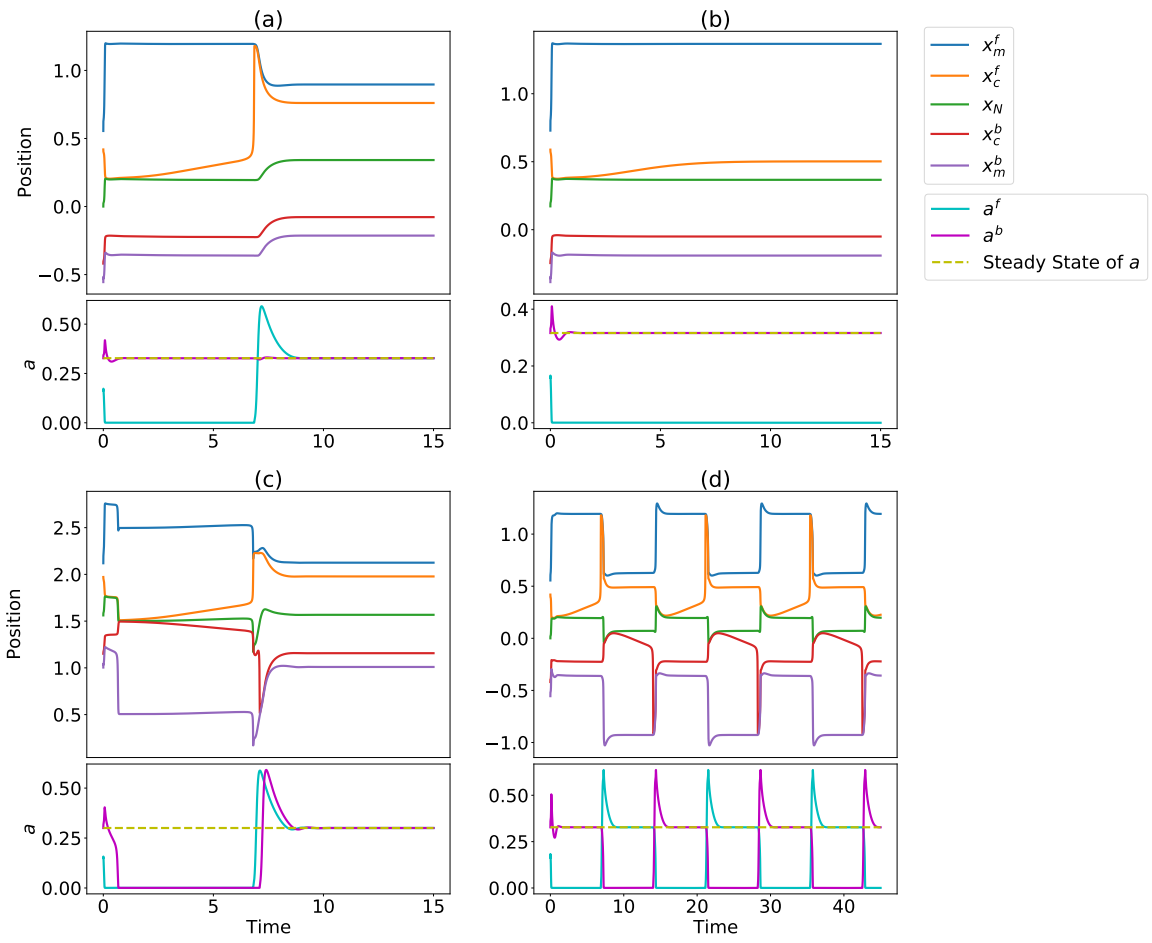

Figure 1.5: Various deterministic model behaviors: *(a)* Single bleb that heals shown in Fig. 1.4. *(b)* Bleb forms but never heals ($M = 0.0084$). *(c)* Front bleb drives a secondary bleb at the back ($\Omega = 44.3$). *(d)* Oscillatory blebbing events alternating from front to back. ($\gamma_m = 0.8 \times 10^{-2}$). Sample paths are initiated at the perturbed $a^f = 0.5 \times a_{ss}^f$. Other parameters are the same as in Fig. 1.4

bleb propagation: when Ω is small, increases in γ_m cause transitions from monostable to excitable and then to bleb propagation with a second bleb forming at the back; when Ω is large, increasing γ_m leads to the oscillatory behaviour.

We find that if D or F are too small, the bleb will not heal (see Figure 1.5(b)). This can be simply explained: if the reach of adhesion molecules is too small, adhesions between membrane and cortex cannot reform; similarly, if F is too small, bonds that do reform are weak and the bleb cannot heal. An increase in K_m does not lead to larger blebs, though it

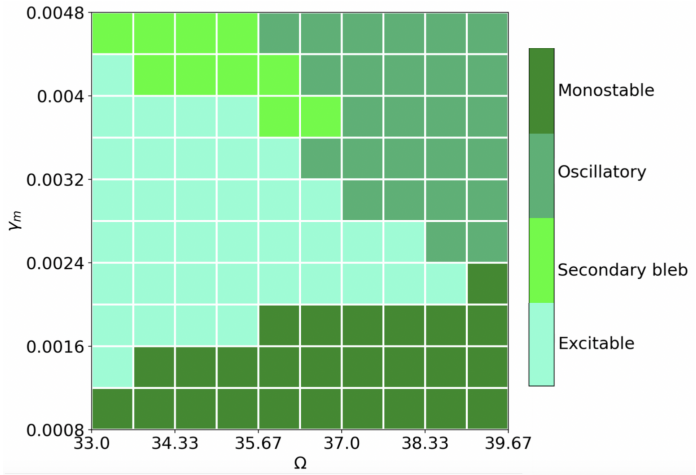

Figure 1.6: Phase diagram of the deterministic model over the Ω - γ_m plane. Other parameters are the same as Fig. 1.4.

does lead to greater displacement. We also find that if M is too small, excitability is lost, while if M is too large, the bleb never heals, suggesting that M, which can be interpreted as myosin contractility, is critical to cell blebbing [51].

The oscillatory behaviour, shown in Figure 1.5(d), appears when γ_m is large. When γ_m is large, Equations 1.2.3 and 1.2.3 show that the boundaries x_m^f and x_m^b both move with velocity u, so that the front and back of the cell are coupled through u due to incompressibility of the fluid, leading to oscillations. The effect of varying γ_m for various values of cortex assembly rate Ω is shown in Figure 1.6. For any value of Ω,, increases in γ_m lead to increases in excitability of the system, as the boundaries move more closely with fluid velocity u. If γ_m is small, then changes in adhesion density are not enough for the membrane to separate from the cortex sufficiently, as any movement of the membrane will be too small and the cortex and adhesions will quickly recover. Figure 1.6 also shows that as Ω increases, the system becomes non-blebbing. This is intuitive: Ω represents the rate of assembly of the cortex, so the higher Ω is, the faster the cortex reassembles and the harder it is for the bleb to form, even under large perturbations in adhesion density. This oscillatory behaviour has been previously observed for protrusions in fibroblasts which, like blebs, are devoid of actin [33].

We further study the effect of varying individual parameters on the size of the bleb and the distance traveled by the cell by fixing all but one at a time, and varying that parameter. Based on this study, we make the predictions shown in Table 1.3. We find that as adhesion reach D increases, healing accelerates - the membrane-cortex distance needed for reattachment is wider, allowing for faster recruitment of adhesions. Similarly, decreases in M lead to faster healing. Increases in K_m lead to smaller bleb size, as the overall force pushing the membrane outward decreases.

Table 1.3: Model Predictions for Experimental Perturbations

Perturbation	Parameter	Prediction
Decrease adhesion strength	$K_m \uparrow$	Smaller blebs
Increase myosin contractility	$M \uparrow$	Slower bleb healing
Increase molecular size of adhesion molecules	$D \uparrow$	Faster healing

1.3.2. Determinants of Distance Travelled

A salient feature of our model, compared with previous efforts to model blebs (for example: [26], [47]), is that the modeled cell is motile, and can employ the bleb to travel. Thus, we may use our model to study what determines whether the cell will travel using a bleb, and what distance may be traversed in a single blebbing event. Thus, we track the total displacement as we vary each parameter within the blebbing regime, using the model to make predictions about the cell's ability to travel. These predictions are summarized in Table 1.4.

Model simulations show that myosin contractility, M, plays a major role in bleb formation and cell travel. In particular, if M is too low, the system is non-blebbing, in line with experimental evidence [51]. When M is above a critical value, the system reaches a blebbing state, with distance traveled increasing as M increases. At the same time, bleb healing becomes slower, with a longer time needed for the cortex to reassemble underneath the membrane (see Figure 1.7). There is a second critical value of M, when it becomes too large and the system transitions to a case where a bleb will form, but not heal. Instead, the

Table 1.4: Predicted Effect of Biophysical Parameters on the Distance Traveled

Perturbation	Parameter	Effect on Distance Traveled
Decrease cortex intensity	$\Omega \downarrow$	Increase
Decrease reach of adhesion molecules	$D \downarrow$	Increase
Decrease adhesion bond strength	$F \downarrow$	Increase
Decrease myosin contractility	$M \downarrow$	Decrease
Increase drag	$D_g \uparrow$, $\chi \uparrow$	Smaller distance traveled
Increase hydrostatic pressure	$K_m \uparrow$	Increase

adhesions do not re-form under the membrane, and the system reaches a new steady state with one side of the membrane permanently detached as shown in Figure 1.5(b).

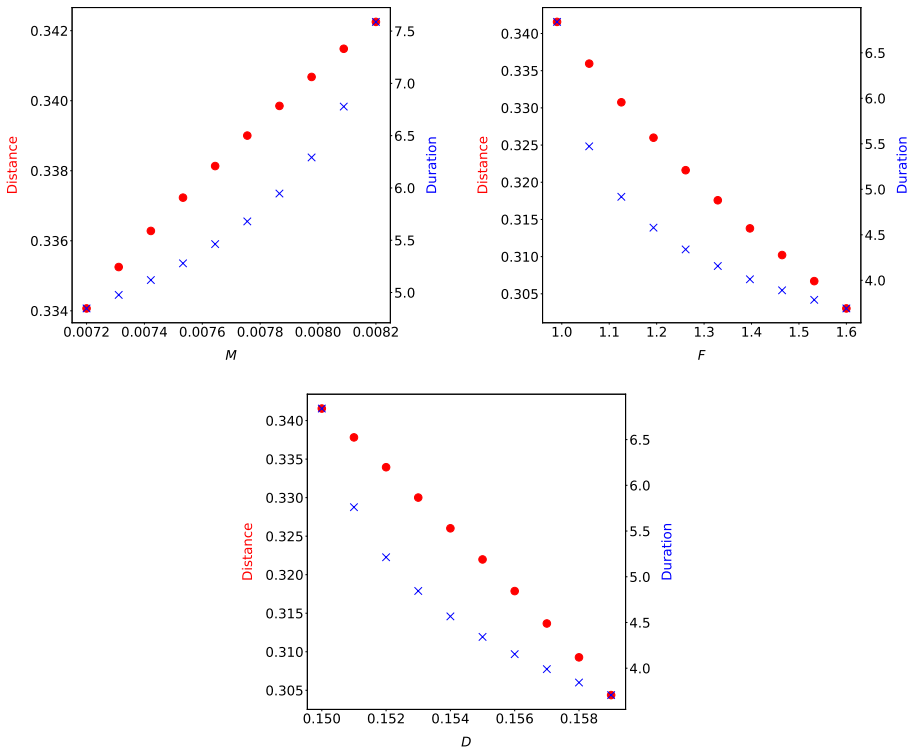

Figure 1.7: Traveling distance and duration for individual blebbing event with various parameters. Other parameters are the same as Fig. 1.4.

Parameters that are intrinsic to the adhesions have significant effects on the distance traveled by the cell. These are the adhesion reach D and the characteristic adhesion-

breaking force F. As D decreases, the total displacement of the cell increases, and bleb healing is slower (see Figure 1.7). It is clear that if the adhesion reach is very large, it is easy (and fast) for the adhesions to re-form and the cortex to reattach, compared with when the adhesion reach is small. However, if D becomes too small, the system reaches a stable non-blebbing state. Similarly, as F decreases, the total displacement of the cell increases, and bleb healing slows down (see Figure 1.7).

Another important parameter is K_m. If K_m is large, we expect that the protrusion formed in the membrane by that pressure when the adhesions are removed will be large, while if the hydrostatic pressure in the cell is low, the membrane expansion will be small. We find that while larger values of K_m lead to greater distances traveled, the bleb size actually decreases. If K_m is too small, the system becomes non-blebbing, while if K_m is too large, the bleb propagates to the other side (Figure 1.5 (c)). K_m can be interpreted as hydrostatic pressure inside the cell pushing the membrane outward.

While variations on the drag in the cortex and nucleus (γ_c and γ_N respectively) do not affect the cell's ability to form a bleb, and the system will remain in the blebbing or non-blebbing regime based on the other parameters, variations in drag can affect the distance traveled. If either drag parameter becomes too large, the net displacement of the cell becomes negligible, even if the bleb does form. Furthermore, changes in γ_c and γ_N can decouple the front and back of the cell, eliminating bleb propagation between the front and back.

Increases in fluid drag D_g decrease the distance traveled, however decreases below 10^{-6} do not have an effect, and setting $D_g = 0$ allows for further simplification of the model.

1.4 Stochastic Model

We now look at modifying the model system 1.12 - 1.19 to include stochastic effects in the adhesion density. Individual adhesion proteins have two possible conformations: open (when they tether the membrane and cortex together), and closed (when they do not).

To formulate the stochastic model, we think of the adhesion dynamics as a birth-death process, with proteins changing conformation so that as the system evolves it may increase or decrease the number of proteins attached and hence the adhesion density. We let $a = \alpha k$, where α is the per-protein adhesion density and k is the number of proteins, and we replace 1.13 with a Markov chain where the probabilities that a new protein will be attached or detached given by g and h respectively, where

$$g(c, a, x_m, x_c) = \frac{c}{1+c} \exp\left(-\frac{1}{D}|x_m - x_c|\right), \tag{1.20}$$

$$h(c, a, x_m, x_c) = a \exp\left(\frac{1}{F}|x_m - x_c|\right). \tag{1.21}$$

To begin the simulation, we choose an initial, or 'base', number of adhesion proteins to be the number of adhesions at steady state at use that to determine α, which is then kept constant. The steady state is computed using the deterministic system. We note that the system is very sensitive to initial conditions, so that a good starting value is required in order to begin the simulation. The stochastic simulations are then run using a continuous-time Gillespie's algorithm to update the number of adhesions attached as the system progresses:

1. Possible events:
    - e_1: adhesion forms ($k \to k+1$)
    - e_2: adhesion breaks ($k \to k-1$)
2. Rates:
    - $r_1 = g(c, a, x_m, x_c)$
    - $r_2 = h(c, a, x_m, x_c)$
3. $r_{total} = r_1 + r_2$

4. Time until next event δt,

$$\int_0^{\delta t} r_{total}(t)\, dt = -\ln(\text{RAND}U[0,1]) \tag{1.22}$$

At each Δt, update the integral using the trapezium rule and check the equality. When it holds, go on.

5. e_j is selected with probability

$$\frac{r_j}{r_{total}} \tag{1.23}$$

to update $a = \alpha k$.

6. Update all other variables.

In contrast with the deterministic system, the stochastic system does not require an initial perturbation to generate a bleb, but can instead be set to steady state of the deterministic system. Then eventually, stochastic fluctuations make the adhesion density become low enough for the membrane and cortex to detach and the system to bleb. An example is shown in Figure 1.8 overlayed on a deterministic simulation for reference.

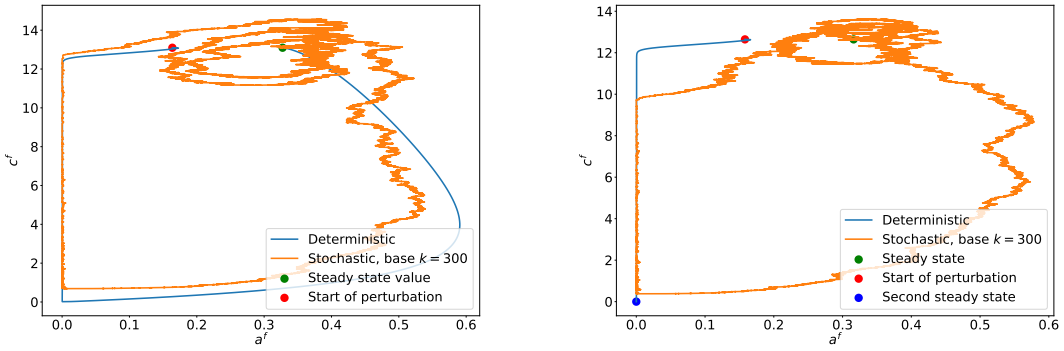

Figure 1.8: Sample stochastic simulation, starting at steady state, with the deterministic case shown for reference. *(left)* Parameters are the same as Fig. 1.4. *(right)* $M = 0.0084$.

A full sample simulation is shown in Figure 1.9. Since the system is symmetric, both sides are equally likely to form a bleb, so that in the long run, the cell does not have an

overall displacement ($\mathbb{E}$[total distance] = 0 for long simulation times).

The choice of base k is key to the frequency of bleb formation, as illustrated in Figure 1.10: if the base value of k is too small, adhesions are removed too easily and the system becomes erratic; if the base value of k is too large, the adhesions never decrease enough for the membrane and cortex to detach and for a bleb to form. We choose a value of k in line with measurements of protein density at the membrane [45].

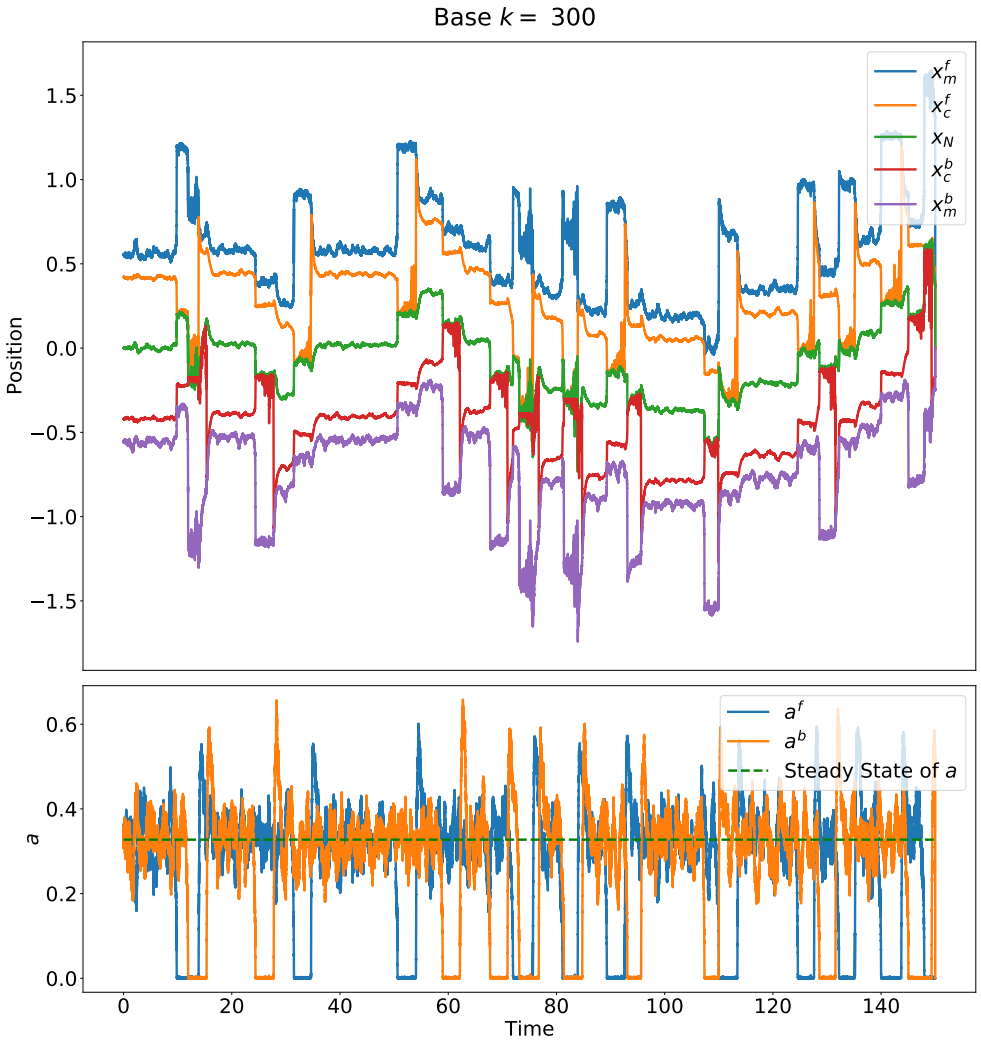

Figure 1.9: Stochastic simulation, starting at steady state. Parameters are the same as Fig. 1.4.

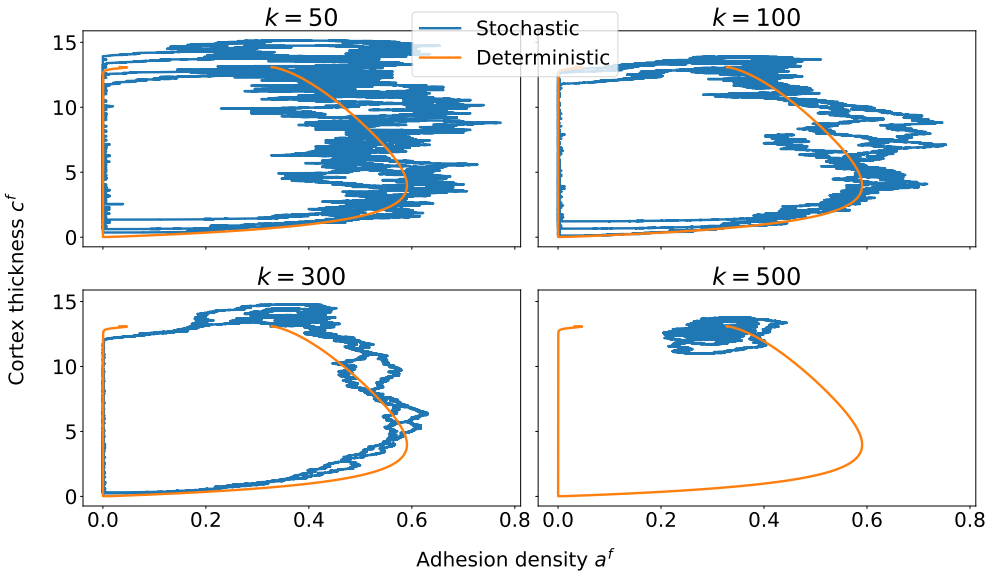

Figure 1.10: Stochastic simulation compared with the deterministic case for various choices of initial number of attached proteins k ($T = 15$). Parameters are the same as Fig. 1.4.

1.4.1. Model Behaviors

In this section, we discuss the differences in system behaviour in the stochastic and deterministic regimes.

In the stochastic regime, bistability (Figure 1.5 (b)) is not a deterrent for the cell to travel, as the system is able to escape also the basin of attraction of the second steady state, as seen in Figure 1.8 (right). Then, even for parameter regimes which would be bistable in the deterministic case, we still get sustained blebbing in the stochastic case.

We find that the onset of oscillations, as shown in Figure 1.5 (d), shifts when we make the system stochastic. We showed in Figure 1.6 that increases in γ_m make the system oscillatory. The onset of this oscillations requires a higher value of γ_m in the stochastic regime than in the deterministic regime. This is likely to be because the steady state is stable, and the stochastic changes push the trajectory out of the oscillatory orbit for lower values of γ_m. A sample stochastic oscillatory simulation is shown in Figure 1.11.

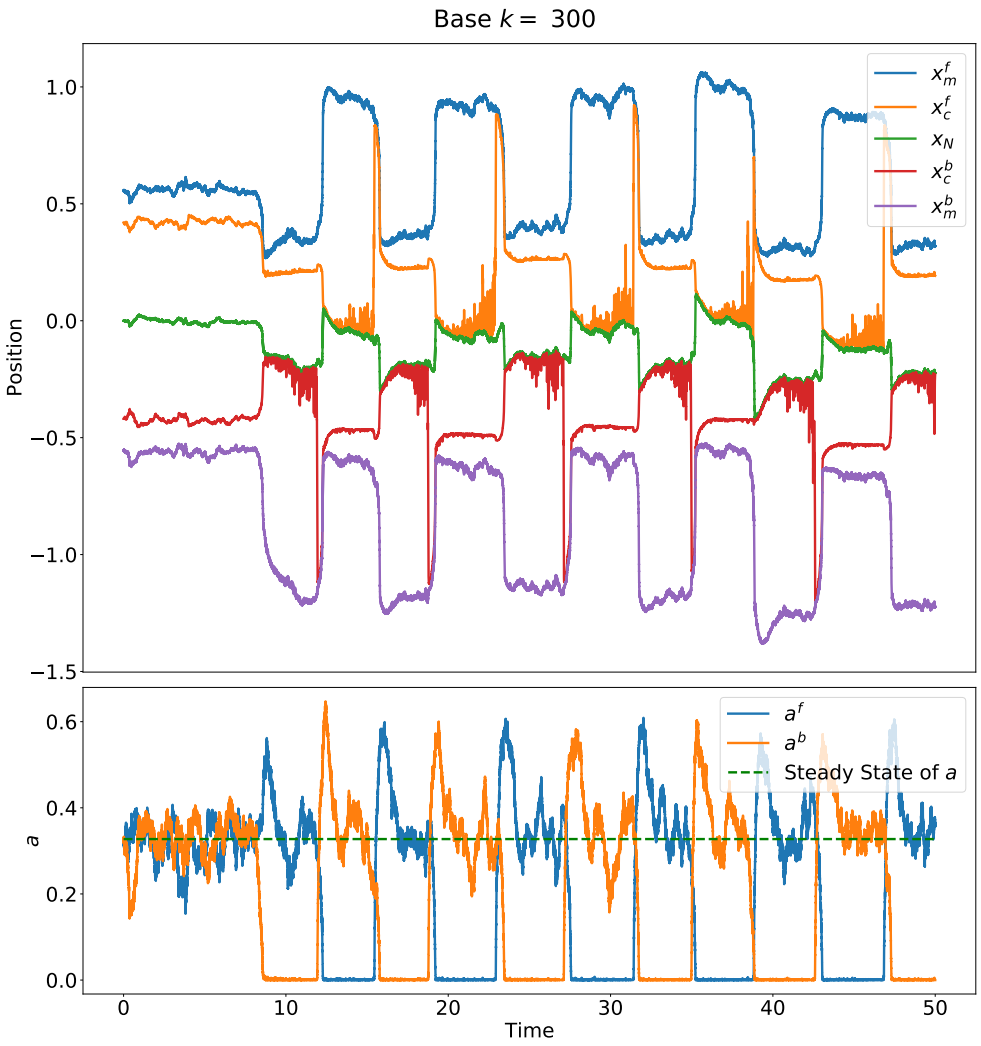

Figure 1.11: Stochastic simulation in the oscillatory regime, starting at steady state. Here, $\gamma_m = 0.8 \times 10^{-1}$, while other parameters are the same as Fig. 1.4.

1.4.2. Introducing Bias

The focus of this study is on the cell's ability to move using blebs. We noted that the system, as simulated in Figure 1.9 is symmetric, so that the cell does not have a significant displacement. Thus, in order to get a net movement and a more realistic system, we bias the cell so that it is more likely to bleb at the front by making the front excitable and the

back monostable in the corresponding deterministic system (the choice of front and back is arbitrary). Then, only the front side will retain the ability to bleb, and the cell will be able to sustain travel in that specific direction.

There are multiple theories regarding the polarization of a blebbing cell. One such theory suggests that there are fewer ERM proteins at the side where the bleb forms [56], [39]. In our model, this corresponds to having a different, smaller, value of a at the front compared to the back. To determine the regime (monostable or excitable/bistable) on each side we use the deterministic system and modify appropriate parameters so that the adhesion densities at the front and back of the cell at steady state are different ($a^f_{ss} \neq a^b_{ss}$). Then, if we set $a^f = \alpha k^f$ and $a^b = \alpha k^b$, where α is equal on both sides, $k^f \neq k^b$. It is then expected that the side with the smaller deterministic steady state value of a (and hence smaller initial k) will be more likely to bleb, as the basin of attraction of the deterministic steady state becomes smaller for smaller steady state values of a. Here, we choose the parameters so that $k^f < k^b$, with the front in the excitable regime (blebbing) and the back in the monostable regime (non-blebbing) as determined in the deterministic setting. At the excitable side (front), noise allows the system to escape the basin of attraction of the steady state, while at the monostable side (back) the basin of attraction cannot be escaped. We note that the biased deterministic simulations still require a manual perturbation for the system to initiate a bleb and travel.

To bias the cell, we change the values of some of the parameters so that they are different at the front and back of the cell (this effectively breaks the symmetry of the system). Since we found that M, F and D control the overall distance traveled, we test these parameters to bias the cell by choosing $M^f \neq M^b$ etc. A sample polarized simulation is shown in Figure 1.12. Varying the parameters at the front and back to get different bias magnitudes showed that if the k^b is less than 4% bigger than k^f the system does not yield a clear cell polarization.

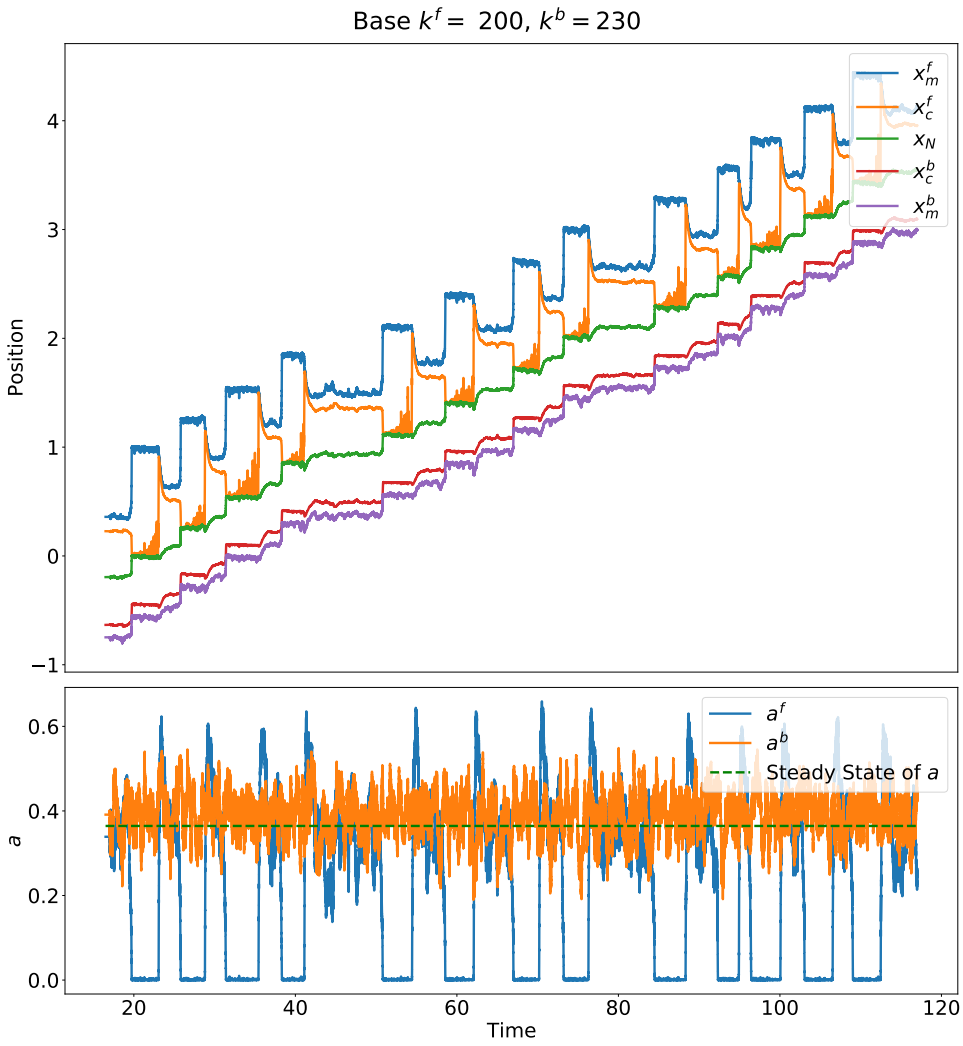

Figure 1.12: Biased stochastic simulation, starting at steady state. $M^f = 0.0078$, $M^b = 0.0065$. Other parameters are the same as Fig. 1.4. Note that the simulation is first run as deterministic to steady state.

1.4.3. Determinants of Distance Traveled

Consider now the biased system in the deterministic case, such that the front is excitable and the back is monostable. In general, low values of myosin contractility M lead to a non-blebbing state, while increasing M takes the system first into the excitable (blebbing) regime and then into the bistable regime. We showed that when both sides are excitable and

have the same parameter values, increases in M lead to increases in the distance traveled in a single event (Figure 1.7). However, if only the front side is excitable, increases in M^f lead to decreases in distance traveled and increases bleb in healing time, as shown in Figure 1.13 (top). When M^f becomes too large, the deterministic system becomes bistable, and the bleb never heals. Note that this threshold does not change when we bias the cell by modifying M^f and M^b. By biasing the cell, we get sustained blebbing in the stochastic case, with cell velocity increasing as M^f increases, as shown in Figures 1.13 (bottom). We find that even though individual events take longer, as seen in the deterministic simulations, the frequency of blebbing also increases in the stochastic simulations, so that the cell travels further.

If we bias the cell by modifying F or D instead ($F^f \neq F^b$, or $D^f \neq D^b$), decreases in F^f or D^f still lead to increases in the distance traveled in a single event (Figures 1.7 and 1.14 (top)). However, the increase in distance is much smaller in the biased case. For changes in F or D, the event duration does not change much between the biased and unbiased settings. Decreasing F^f or D^f any further would lead to the bistable regime. In the stochastic case, cell velocity increases as F^f or D^f decreases, as shown in Figures 1.13 (bottom) and 1.14 (bottom).

1.4.4. Approximation of biased stochastic model

One important feature of the biased stochastic model is that the bleb expansion period has very short time scale than the other states, as seen in Fig. 1.16(a). Such series of bleb events can be approximated by a renewal process [11, 5]. A single bleb event consists of two random variables: the inter-blebbing time Δ and the traveling distance Q. Labeling the bleb events by $n = 1, 2, \cdots$. We collect the statistics of (Δ_n, Q_n) from a total of 10^3 sample paths which initial condition is at the steady-state of the deterministic model. Results shows that the statistics of (Δ_n, Q_n) are independent and identically distributed for all n. It is because each bleb event is generated by stochastically escaping the same deterministic basin of attraction, as shown in Fig. 1.8. Another observation is that Δ_n and Q_n are almost

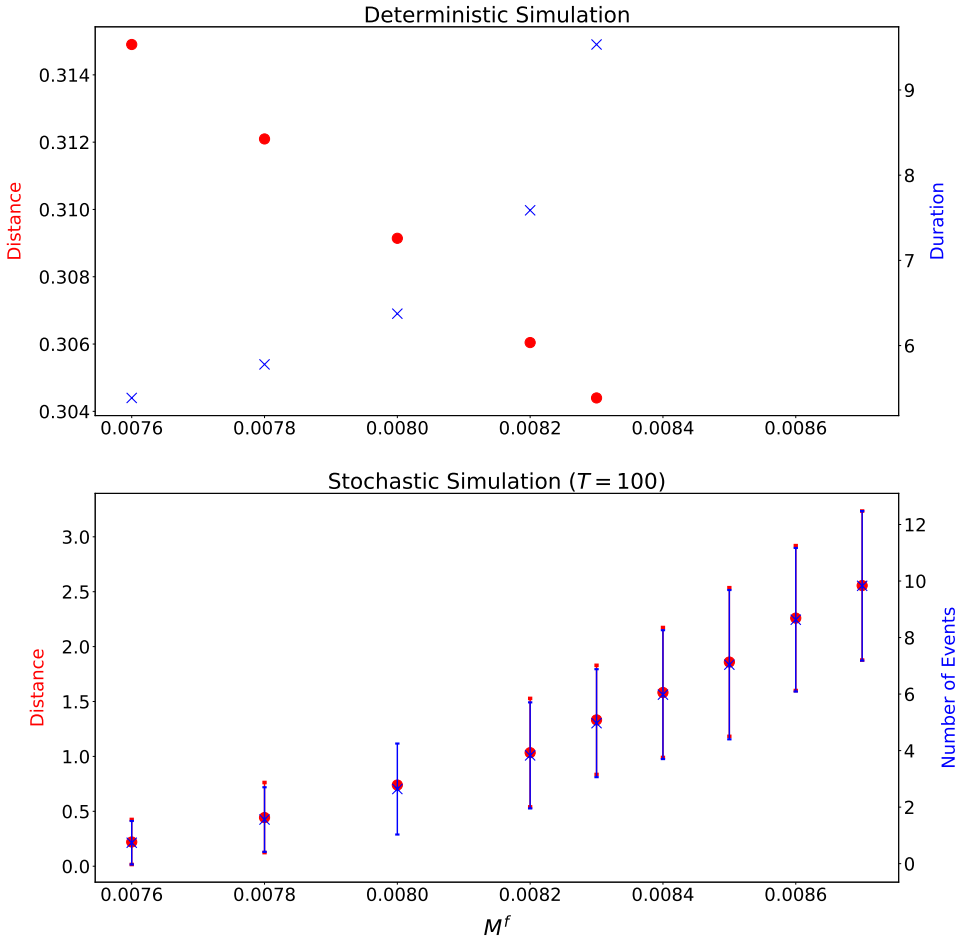

Figure 1.13: Parameters are as in Fig. 1.4. *(top)* Distance traveled and event time for a single bleb in the deterministic case as M^f varies. *(bottom)* Average total distance travelled for time $T = 100$ and number of blebbing events for the stochastic case as M^f varies with $M^b = 0.0065$. Time step was set at $\Delta t = 0.0001$, and the initial number of adhesions was set to $k = 300$.

uncorrelated

$$\left| \frac{\mathrm{Cov}(\Delta_n, Q_n)}{\mathbb{E}[\Delta_n]\mathbb{E}[Q_n]} \right| \sim 0.015,$$

We thus assume that the random variables are independent for the same n. To utilize the discrete data as a continuous information, we approximate the statistics of the random variables by the gamma distributions. That is, the distributions of the random variables

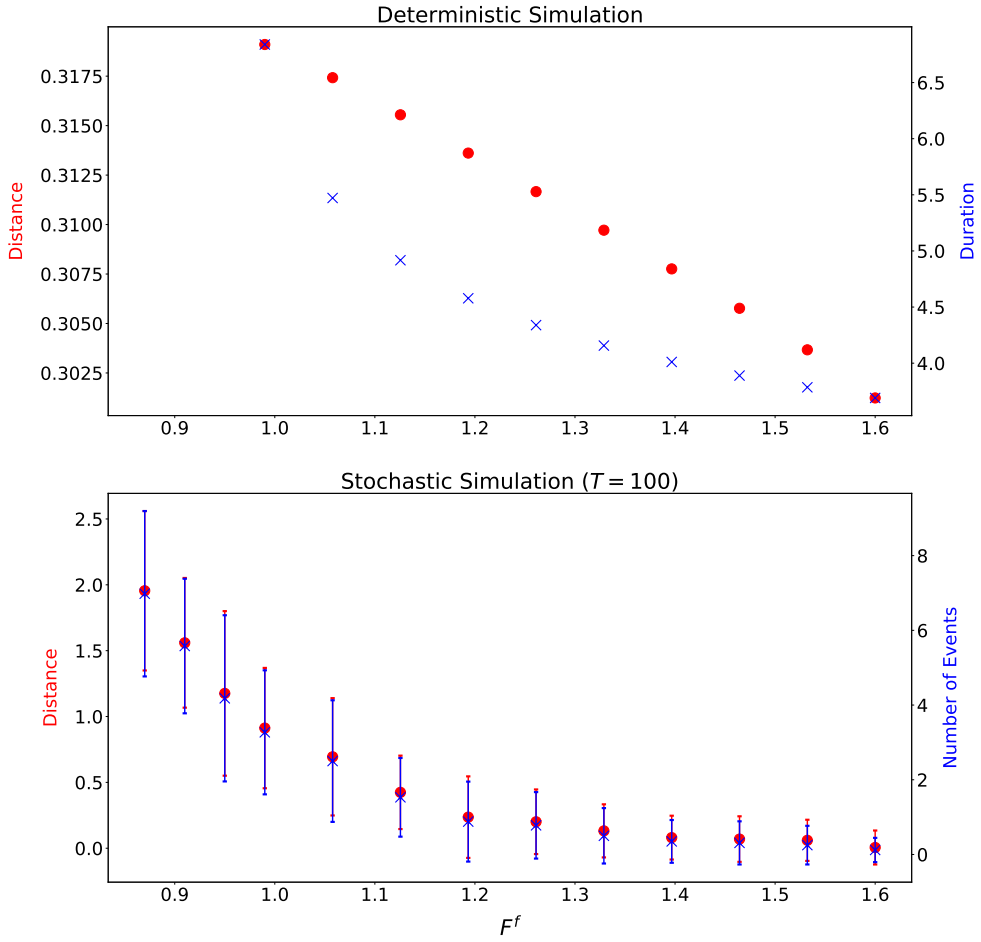

Figure 1.14: Parameters are as in Fig. 1.4. *(top)* Distance traveled and event time for a single bleb in the deterministic case as F^f varies. *(bottom)* Average total distance travelled for time $T = 100$ and number of blebbing events for the stochastic case as F^f varies with $F^b = 1.7$. Time step was set at $\Delta t = 0.0001$, and the initial number of adhesions was set to $k = 300$.

take the form of

$$\mathbb{P}[\Delta_n \leq t] = \int_0^t f_{\Delta_n}(t')dt', \quad \mathbb{P}[Q_n \leq x] = \int_0^x f_{Q_n}(x')dx',$$

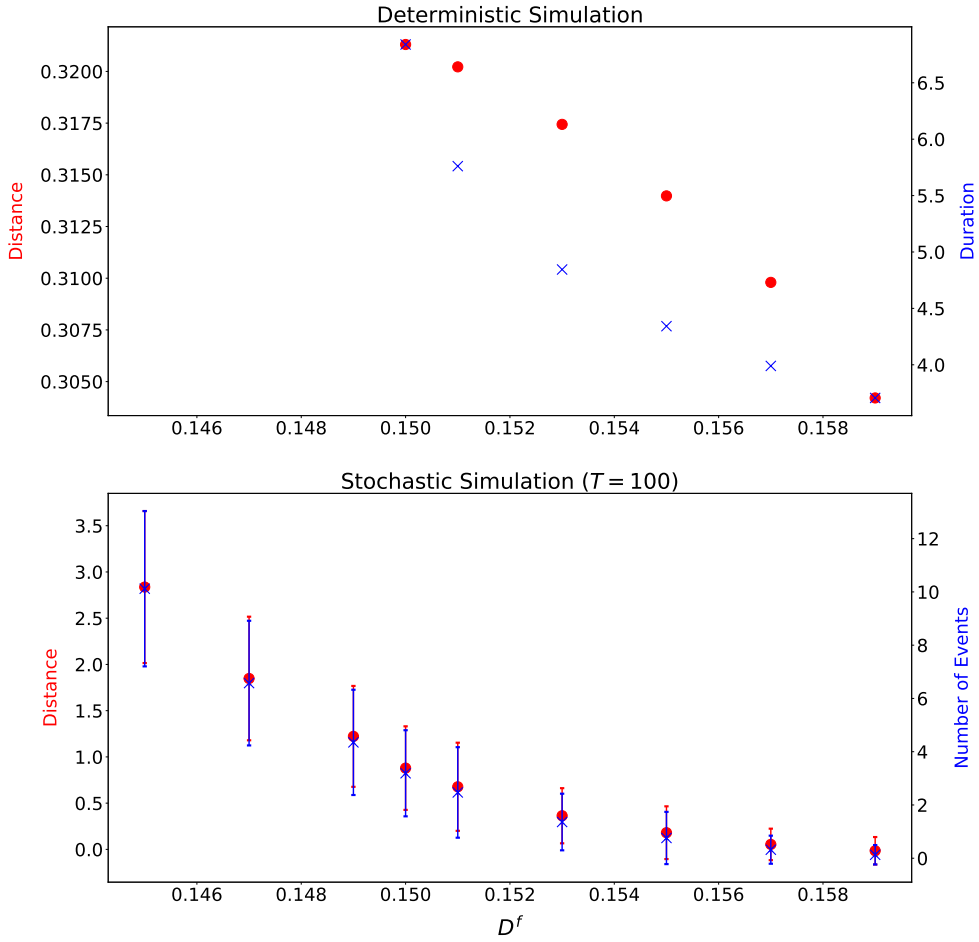

Figure 1.15: Parameters are as in Fig. 1.4. *(top)* Distance traveled and event time for a single bleb in the deterministic case as D^f varies. *(bottom)* Average total distance travelled for time $T = 100$ and number of blebbing events for the stochastic case as D^f varies with $D^b = 0.159$. Time step was set at $\Delta t = 0.0001$, and the initial number of adhesions was set to $k = 300$.

where $f_X(t) = f(t; \alpha_X, \beta_X)$ is the gamma distribution with shape α_X and scale β_X. Therefore, our assumptions deduce that

$$f_{\Delta_n} = f_{\Delta_m} := f_\Delta, \quad f_{Q_n} = f_{Q_m} := f_Q,$$

for all n, m. We estimate $(\alpha_{\Delta_n}, \beta_{Q_n})$ by the maximum likelihood estimation, as depicted in the subpanel of Fig. 1.16(a).

Next, we determine the distribution information of the renewal process in terms of the gamma distributions. Introducing the blebbing time

$$T_n = T_{n-1} + \Delta_n, \quad T_0 = 0,$$

then one can write the renewal process by

$$X(t) = \sum_{T_n \le t} Q_n H(t - T_n), \tag{1.24}$$

where $H(t)$ is the Heaviside function giving one if $t > 0$ otherwise zero. For given $T_1 = \Delta_1 = \tau_1$ and $Q_1 = \eta_1$, we have

$$X(t) = \begin{cases} 0, & t < \tau_1 \\ \eta_1 + X^*(t - \tau_1), & t \ge \tau_1 \end{cases}, \tag{1.25}$$

where $X^*(t)$ is identical with $X(t)$. Thus, applying conditional expectation theorem gives

$$\begin{aligned} M_X(\xi, t) := \mathbb{E}[e^{\xi X(t)}] &= \mathbb{E}\left[\mathbb{E}[e^{\xi X(t)} | T_1 = \tau_1, Q_1 = \eta_1]\right] \\ &= \int_t^\infty f_\Delta(\tau) d\tau + \mathbb{E}\left[\mathbf{1}_{\tau_1 \le t} \mathbb{E}[e^{\xi Q_1} e^{\xi X^*(t - T_1)} | T_1 = \tau_1, Q_1 = \eta_1]\right]. \end{aligned} \tag{1.26}$$

Since Q_1 and T_1 are independent, we have

$$M_X(\xi, t) = \int_t^\infty f_\Delta(\tau) d\tau + M_Q(\xi) \int_0^t M_X(\xi, t - \tau) f_\Delta(\tau) d\tau. \tag{1.27}$$

Since the moments of the approximation process satisfies

$$\mathcal{M}_k(t) := \mathbb{E}[X^k(t)] = \left. \frac{\partial^k \widetilde{M}_X(\xi, t)}{\partial \xi^k} \right|_{\xi = 0},$$

for $k = 1, 2, \cdots$, taking derivatives with respect to ξ gives

$$\mathcal{M}_k(t) = \sum_{j=0}^{k} \mathbb{E}[Q^{k-j}] \int_0^t \mathcal{M}_j(t-\tau) f_\Delta(\tau) d\tau. \tag{1.28}$$

Average speed of the approximation process can be calculated by performing Laplace transformation. Taking Laplace transformation to (1.28)

$$\widetilde{\mathcal{M}}_k(s) = \widetilde{f}_\Delta(s) \sum_{j=0}^{k} \binom{k}{j} \mathbb{E}[Q^{k-j}] \widetilde{\mathcal{M}}_j(s), \tag{1.29}$$

and solving for $\widetilde{\mathcal{M}}_k(s)$ yields

$$\mathcal{M}_k(s) = \frac{\widetilde{f}_\Delta(s)}{1 - \widetilde{f}_\Delta(s)} \left(\sum_{j=1}^{k-1} \binom{k}{j} \mathbb{E}[Q^{k-j}] \mathcal{M}_j(s) + \frac{q_k}{s} \right), \tag{1.30}$$

in accordance with $q_0 = 1$ and $\mathcal{M}_0(s) = s^{-1}$. In particular, the first moment takes the form of

$$\mathcal{M}_1(s) = \frac{\mathbb{E}[Q] \widetilde{f}_\Delta(s)}{s \left(1 - \widetilde{f}_\Delta(s)\right)}. \tag{1.31}$$

Performing integration by parts and l'Hospital rule yields

$$\begin{aligned} \lim_{ttoo\infty} \frac{\mathcal{M}_1(t)}{t} &= \lim_{s \to 0} s \int_s^\infty \widetilde{\mathcal{M}}_1(s') ds' \\ &= \lim_{s \to 0} s^2 \widetilde{\mathcal{M}}_1(s). \end{aligned} \tag{1.32}$$

Substituting (1.31) into the above equation and another application of the l'Hospital rule gives

$$\begin{aligned} \lim_{t \to \infty} \frac{\mathcal{M}_1(t)}{t} &= \mathbb{E}[Q] \lim_{s \to 0} \frac{s \widetilde{f}_\Delta(s)}{\left(1 - \widetilde{f}_\Delta(s)\right)} \\ &= \mathbb{E}[Q] \lim_{s \to 0} \frac{\widetilde{f}_\Delta(s) + s \widetilde{f}'_\Delta(s)}{-\widetilde{f}'_\Delta(s)} = \frac{\mathbb{E}[Q]}{\mathbb{E}[\Delta]} := v_\infty, \end{aligned} \tag{1.33}$$

according to the fact that

$$\widetilde{f}'_{\Delta}(s) = -\int_0^{\infty} t f_{\Delta}(t) e^{-st} dt \to -\mathbb{E}[\Delta],$$

as $s \to 0$. One can also calculate the asymptotic limit of the variance of the approximation process. Similar to (1.32), one can have

$$\begin{aligned}\lim_{t\to\infty} \frac{\mathbb{E}[(X(t) - v_{\infty}t)^2]}{t} &= \lim_{t\to\infty} \frac{\mathcal{M}_2(t) - (v_{\infty}t)^2}{t} \\ &= \lim_{s\to 0} s^2 \left(\widetilde{\mathcal{M}}_2(s) - \frac{2v_{\infty}^2}{s^3} \right). \end{aligned} \tag{1.34}$$

Substituting the Laplace transform of the second moment

$$\mathcal{M}_2(s) = \frac{1}{s} \left[\frac{\mathbb{E}[Q^2]\ \widetilde{f}_{\Delta}(s)}{1 - \widetilde{f}_{\Delta}(s)} + 2 \left(\frac{\mathbb{E}[Q]\widetilde{f}_{\Delta}(s)}{1 - \widetilde{f}_{\Delta}(s)} \right)^2 \right], \tag{1.35}$$

into (1.34) and performing l'Hospital rules yields

$$\begin{aligned}\lim_{t\to\infty} \frac{\mathbb{E}[(X(t) - v_{\infty}t)^2]}{t} &= \lim_{s\to 0} s \left[\frac{\mathbb{E}[Q^2]\ \widetilde{f}_{\Delta}(s)}{1 - \widetilde{f}_{\Delta}(s)} + 2 \left(\frac{\mathbb{E}[Q]\widetilde{f}_{\Delta}(s)}{1 - \widetilde{f}_{\Delta}(s)} \right)^2 \right] - \frac{2v_{\infty}^2}{s} \\ &= \frac{\mathbb{E}[Q^2] + 2v_{\infty}^2 \left(\mathbb{E}[\Delta^2] - 2\mathbb{E}[\Delta]^2 \right)}{\mathbb{E}[\Delta]} := \sigma_{\infty}^2. \end{aligned} \tag{1.36}$$

The asymptotic behavior of the approximation process can be matched by the following stochastic differential equation

$$dY_t = v_{\infty} dt + \sigma_{\infty} dW_t, \tag{1.37}$$

where W_t is a Wiener process.

Numerical comparison in Fig. 1.16(b) shows that the first moments of the original stochastic model and our approximation by solving (1.28) are in a good agreement. In particular, the asymptotic slope for both processes converges to the value in (1.33) as

$t \to \infty$.

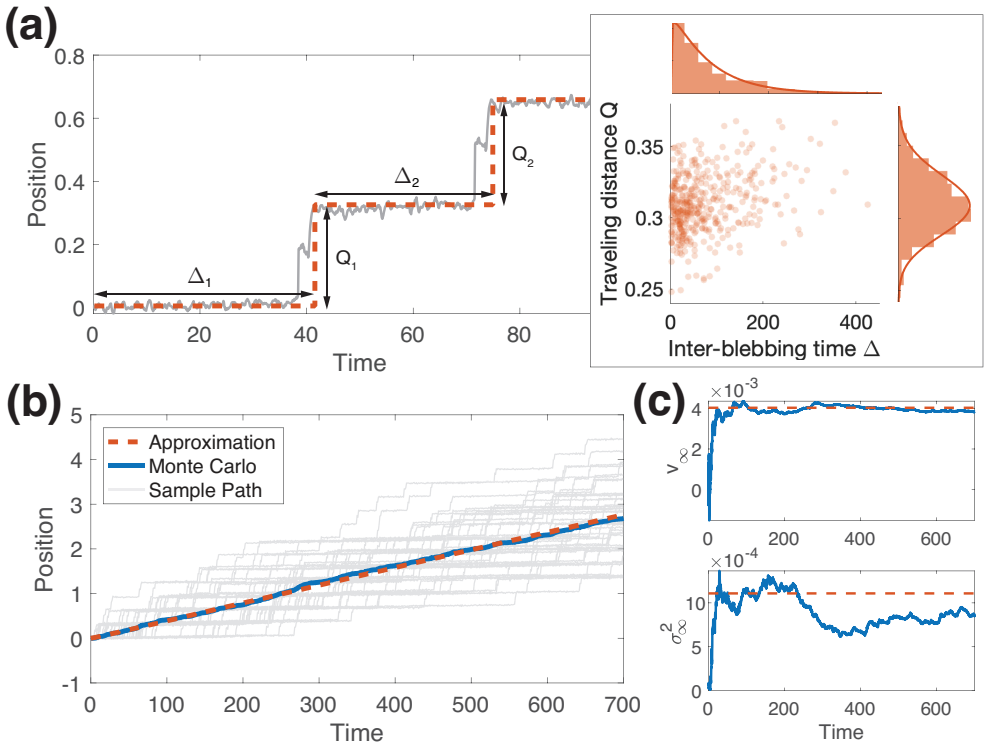

Figure 1.16: Approximation of the biased stochastic model. (a) Nucleus position $x_N(t)$ is approximated by a renewal process $X(t)$ with inter-blebbing time Δ_n and traveling distance Q_n for $n = 1, 2, \cdots$. Statistics of the first bleb event and the following events (*red dots*) are independent and identically distributed. (b) Average nucleus position as a function of time. The first moment of the original process (*blue curve*) comes from averaging a total of 48 sample paths (*gray curves*). Corresponding curve for the approximation processes (*red-dotted curve*) are computed by numerically solving (1.28) for $k = 1$. (c) Time-averaged speed (*top*) and variance (*bottom*) of the original process is compared with the asymptotic speed and variance of the approximation process by (1.33) and (1.36). Parameters used here are $\Omega_f = 40$, $\Omega_b = 32$, and others are the same as Fig. 1.4.

1.5 Discussion

The model presented here considers the bleb formation and healing cycle together with the mechanics of the system to produce bleb-driven cell migration. We investigate the size of the blebs, the time from formation to healing, and, for the first time, the distance traveled in individual blebbing events. The stochastic model allows sustained cell travel by repeated

blebbing.

This is the first model to allow elucidation of the determinants of distance traveled during a bleb in terms of biophysical parameters such as adhesion kinetics and myosin contractility. We find that myosin contractility, and the molecular reach and strength of adhesions determine the distance traveled by the cell with a single bleb (Figure 1.7). Our model makes predictions about how the distance traveled changes with experimental perturbations, such as changes in myosin contractility that could be induced by changes in blebbistatin [51].

We also investigate the effect of varying biophysical parameters on bleb size and healing time. In this case, we find that changes in the molecular reach of adhesions, in the nondimensional parameter D, affect the time taken for the bleb to heal (as in [26]). In contrast with the results in [26], where increases in M abolish blebbing, increases in myosin contractility in our model lead to a case where the bleb forms, but never heals (see Figure 1.5 (b)). This can be interpreted as cell death, or can be thought of as the cell healing being beyond scales of interest. In our case, it is decreases in myosin contractility M that abolish blebbing.

The stochastic version of the model allows for sustained travel. In this case, excitability of the system, which was crucial for the deterministic model presented as well as for previous efforts [26], is no longer necessary, as bistability suffices (see Figure 1.13). When the cell is biased to travel in the front direction, contraction at the back leads to a net movement forward towards the healing bleb [24], so that in the deterministic case the overall distance travel decreases as the difference between the front and back values of myosin contractility M lead to a decrease in distance traveled. In the stochastic case however, the basin of attraction of the steady state becomes smaller, so that even though individual events produce less movements as M increases, the overall distance traveled over longer times is larger. It is also possible for the stochastic model to generate sustained travel in the bistable case, as the system is able to produce enough noise to escape both basins of attraction in tandem.

From a theoretical perspective, we studied a stochastic hybrid system that involves an excitable deterministic system (cell migration dynamics) and a Markov chain on some discrete space (adhesion proteins assembly and turnover). Spontaneous excitation (cell bleb event) is initiated by escaping the deterministic basin of attraction. Such escape time problems have been studied in the context of cellular neuroscience by applying Kramer's rate theory [19], [20] and the large deviation theory [41], [15], [32]. Instead of the analytic approximations, we directly obtain the escape time distribution by Monte Carlo simulation and focus on analyzing the resulting behavior driven by the series of excitation events.

The framework presented here can be extended to 2D and 3D bleb-driven migration by extending the mechanical model and utilizing the immersed boundary method to combine this motility model with previous efforts that considered the role of fluid pressure inside and outside the cell, such as [47].

CHAPTER 2 : Bleb-driven Migration in 2D

2.1 Introduction

In this Chapter, we extend the framework presented in Chapter 1 to the 2D case. We formulate the model and use the Immersed Bounday Method (IBM) [35] for simulation. We present preliminary results and make suggestions to refine the model and numerical algorithm. This 2D model fully combines the turnover model of [26] with the computational fluid dynamics model of [47].

2.2 Model Formulation

This 2D model follows the same rationale as the 1D version, extending the turnover model from [26] to the vector case to consider the Euclidean distance between the membrane and cortex locations ($\mathbf{X}_M(\theta)$ and $\mathbf{X}_C(\theta)$).

$$\frac{\partial c}{\partial t} = \omega a - rc \tag{2.1}$$

$$\frac{\partial a}{\partial t} = \frac{k_{on} c}{c_0 + c} \exp\left(\frac{-|\mathbf{X}_M - \mathbf{X}_C|}{\delta}\right) - k_{off} a \exp\left(\frac{\kappa |\mathbf{X}_M - \mathbf{X}_C|}{f_0}\right) \tag{2.2}$$

The membrane experiences three forces: tension $\mathbf{F}_T^M$, bending $\mathbf{F}_B^M$, and adhesion to the cortex $\mathbf{F}_{AD}^M$, with

$$\mathbf{F}_T^M = \frac{\partial}{\partial \theta}(T_M \boldsymbol{\tau}_M), \qquad T_M = g_m + \kappa_m \left(\left|\frac{\partial \mathbf{X}_M}{\partial \theta}\right| - l\right), \quad \boldsymbol{\tau}_M = \frac{\partial \mathbf{X}_M}{\partial \theta}\left|\frac{\partial \mathbf{X}_M}{\partial \theta}\right|^{-1} \tag{2.3}$$

$$\mathbf{F}_{AD}^M = -(a\kappa + \kappa_c)\left(|\mathbf{X}_M - \mathbf{X}_C| - \delta\right)\frac{\mathbf{X}_M - \mathbf{X}_C}{|\mathbf{X}_M - \mathbf{X}_C|} = -\mathbf{F}_{AD}^C \tag{2.4}$$

$$\mathbf{F}_B^M = -\varepsilon \frac{\partial^4 \mathbf{X}_M}{\partial \theta^4} \tag{2.5}$$

Force balance at the membrane is then given by

$$\mathbf{u} - \frac{\partial \mathbf{X}_M}{\partial t} = f_w - \pi \mathbf{n}, \qquad f_w = -\zeta \hat{\mathbf{F}}_M \qquad \hat{\mathbf{F}}_M = \mathbf{F}_M \left| \frac{\partial \mathbf{X}_M}{\partial \theta} \right|^{-1}, \quad \mathbf{F}_M = \mathbf{F}_T^M + \mathbf{F}_{AD}^M \tag{2.6}$$

where f_w gives water flow across the membrane and $\pi \mathbf{n}$ gives osmotic pressure.

The cortex similarly experiences two forces: tension $\mathbf{F}_T^C$, and adhesion to the membrane $\mathbf{F}_{AD}^C = -\mathbf{F}_{AD}^M$, with

$$\mathbf{F}_T^C = \frac{\partial}{\partial \theta}(T_C \boldsymbol{\tau}_C), \qquad T_C = g_c + \sigma c \left(\left| \frac{\partial \mathbf{X}_C}{\partial \theta} \right| - \beta \right), \quad \boldsymbol{\tau}_C = \frac{\partial \mathbf{X}_C}{\partial \theta} \left| \frac{\partial \mathbf{X}_C}{\partial \theta} \right|^{-1} \tag{2.7}$$

Force balance at the cortex is then

$$\eta_c c \left(\frac{\partial \mathbf{X}_C}{\partial t} - \mathbf{u} \right) = \mathbf{F}_C = \mathbf{F}_T^C + \mathbf{F}_{AD}^C \tag{2.8}$$

In this case, we cannot eliminate the pressure and fluid velocity, and simulate Stokes flow in full,

$$\begin{cases} \mu \Delta \mathbf{u} - \nabla p - \xi \mathbf{u} + \mathbf{f} = 0 \\ \nabla \cdot \mathbf{u} = 0 \end{cases} \tag{2.9}$$

where $\mathbf{f}$ combines the forces on the membrane and cortex that affect the fluid field,

$$\mathbf{f} = \mathbf{f}_{AD}^M + \mathbf{f}_T^M + \mathbf{f}_B^M + \mathbf{f}_{AD}^C + \mathbf{f}_T^C \tag{2.10}$$

All parameters are defined in Table 2.5. The estimates provided on Table 2.5 are the ones used in the simulations shown in this work, but extensive parameter exploration is still needed to properly calibrate this model.

Table 2.5: Model Parameters

Symbol	Dimensions	Meaning	Estimate
ω	(A.U.) μm^2 s^{-1}	cortex assembly rate constant	0.12
r	s^{-1}	cortex turnover rate constant	0.1
k_{on}	μm^{-2}s^{-1}	adhesion assembly rate	100
k_{off}	s^{-1}	adhesion turnover rate	10
c_0	(A.U.)	cortex thickness at adhesion saturation	1
δ	μm	adhesion length between cortex and membrane	0.3
κ	pN μm^{-1}	adhesion spring constant	400
f_0	pN	adhesion breaking strength	800
ξ	Pa s μm^{-2}	ratio of dynamic viscosity and permeability	10^{-4}
κ_m	Pa μm^{-1}	hydrostatic pressure scale	350
ζ	μm^2 s^{-1}Pa^{-1}	water permeability constant	0.003
σ	Pa (A.U)$^{-1}$ μm^{-1}	actin-myosin contractility	6.94
β	μm	cortex rest length	2.5
l	μm	membrane rest length	8
η_c	Pa s μm^{-1} (A.U)$^{-1}$	cortex drag factor	0.1
μ	Pa s	dynamic viscosity	1
g_m	pNμm^{-1}	membrane surface tension	0
g_c	pNμm^{-1}	cortex surface tension	10^{-8}
π	μms^{-1}	osmotic pressure factor	0
κ_c	pN μm^{-3}	base adhesion spring constant	7
ε	pN	bending stiffness	10^{-5}

2.3 Numerical Method

Note that the lower case forces are located on the Cartesian grid where the fluid equations are solved, while the upper case forces are located on the Lagrangian grid that defines the cell membrane and cortex locations. This is consistent with the IBM formulation for the simulation algorithm. For the flow field $\mathbf{u}$ and the pressure p we use a regular Cartesian grid with grid spacing h. The grid points θ on the Lagrangian mesh, or the corresponding position $(X(\theta), Y(\theta))$ are the immersed boundary points.

1. Update adhesion and cortex densities

$$c^{i,n+1}\left(\frac{1}{\Delta t}+r\right)=\frac{c^{i,n}}{\Delta t}+\omega a^{i,n}$$

$$\frac{a^{i,n+1}-a^{i,n}}{\Delta t}=\frac{k_{on}c^{i,n}}{c_0+c^{i,n}}\exp\left(-\frac{|\mathbf{X}_M-\mathbf{X}_C|^{i,n}}{\delta}\right)-k_{off}a^{i,n+1}\exp\left(\frac{\kappa|\mathbf{X}_M-\mathbf{X}_C|^{i,n}}{f_0}\right)$$

2. Solve for the fluid field using the IBM. Compute the relevant forces using a fully explicit discretization.

   (a) Given $\mathbf{X}_M^n$ and $\mathbf{X}_C^n$, compute

$$\mathbf{F}_M^n=\mathbf{F}_{AD}^M+\mathbf{F}_T^M+\mathbf{F}_B^M$$

$$\mathbf{F}_C^n=\mathbf{F}_{AD}^C+\mathbf{F}_T^C$$

   (b) Spread $\mathbf{F}_M^n$ and $\mathbf{F}_C^n$ onto the fluid mesh using

$$\mathbf{f}_i=\sum_\theta \mathbf{F}_i^n\delta_h(\mathbf{x}-\mathbf{X}^n)\Delta\theta$$

   where $i=M,C$, and combine them to obtain $\mathbf{f}^n=\mathbf{f}_M^n+\mathbf{f}_C^n$. Here,

$$\delta_h(r)=\frac{1}{h}\phi\left(\frac{r}{h}\right),$$

$$\phi(r) = \begin{cases} \frac{1}{8}(3 - 2|r| + \sqrt{1 + 4|r| - 4r^2}, & |r| \leq 1 \\ \frac{1}{8}(5 - 2|r| - \sqrt{-7 + 12|r| - 4r^2}, & 1 < |r| \leq 2 \\ 0 & 2 < |r| \end{cases}$$

(c) Use $\mathbf{f}^n$ to solve for $\mathbf{u}^n$ and p^n.

(d) Use $\mathbf{u}^n$ to compute $\mathbf{U}^n$ using

$$\mathbf{U}^n = \sum_{\mathbf{x}} \mathbf{u}^n \delta_h(\mathbf{x} - \mathbf{X}^n) h^2$$

3. Update membrane positions:

$$\begin{aligned} \frac{\mathbf{X}_M^{i,n+1} - \mathbf{X}_M^{i,n}}{\Delta t} &= \mathbf{U}^i \\ &+ \zeta \Bigg(\frac{1}{\Delta\theta} \left[\left(g_m + \kappa_m \left(\frac{|\mathbf{X}_M^{i+1,n} - \mathbf{X}_M^{i,n}|}{\Delta\theta} - l \right) \right) \frac{\mathbf{X}_M^{i+1,n+1} - \mathbf{X}_M^{i,n+1}}{|\mathbf{X}_M^{i+1,n} - \mathbf{X}_M^{i,n}|} \right] \\ &- \frac{1}{\Delta\theta} \left[\left(g_m + \kappa_m \left(\frac{|\mathbf{X}_M^{i,n} - \mathbf{X}_M^{i-1,n}|}{\Delta\theta} - l \right) \right) \frac{\mathbf{X}_M^{i,n+1} - \mathbf{X}_M^{i-1,n+1}}{|\mathbf{X}_M^{i,n} - \mathbf{X}_M^{i-1,n}|} \right] \\ &- (a^i \kappa + \kappa_c) \left(|\mathbf{X}_M^{i,n} - \mathbf{X}_C^{i,n}| - \delta \right) \frac{\mathbf{X}_M^{i,n} - \mathbf{X}_C^{i,n}}{|\mathbf{X}_M^{i,n} - \mathbf{X}_C^{i,n}|} \\ &- \frac{\varepsilon}{(\Delta\theta)^4} \left(\mathbf{X}_M^{i+2,n+1} - 4\mathbf{X}_M^{i+1,n+1} + 6\mathbf{X}_M^{i,n+1} - 4\mathbf{X}_M^{i-1,n+1} + \mathbf{X}_M^{i-2,n+1} \right) \Bigg) \\ &\cdot \frac{\Delta\theta}{|\mathbf{X}_M^{i,n} - \mathbf{X}_M^{i-1,n}|} + \pi \mathbf{n}^{i,n} \end{aligned}$$

4. Update cortex positions:

$$\begin{aligned}
\eta_c c^i \frac{\mathbf{X}_C^{i,n+1} - \mathbf{X}_C^{i,n}}{\Delta t} &= \eta_c c^i \mathbf{U}^i \\
&- \frac{a^i \kappa \left(|\mathbf{X}_M^{i,n} - \mathbf{X}_C^{i,n}| - \delta \right)}{|\mathbf{X}_M^{i,n} - \mathbf{X}_C^{i,n}|} (\mathbf{X}_M^{i,n} - \mathbf{X}_C^{i,n+1}) \frac{\Delta\theta}{|\mathbf{X}_C^{i,n} - \mathbf{X}_C^{i-1,n}|} \\
&- \left(g_c + \sigma \frac{c^{i+1} + c^i}{2} \left(\frac{|\mathbf{X}_C^{i+1,n} - \mathbf{X}_C^{i,n}|}{\Delta\theta} - \beta \right) \right) \frac{\mathbf{X}_C^{i+1,n+1} - \mathbf{X}_C^{i,n+1}}{|\mathbf{X}_C^{i+1,n} - \mathbf{X}_C^{i,n}||\mathbf{X}_C^{i,n} - \mathbf{X}_C^{i-1,n}|} \\
&+ \left(g_c + \sigma \frac{c^i + c^{i-1}}{2} \left(\frac{|\mathbf{X}_C^{i,n} - \mathbf{X}_C^{i-1,n}|}{\Delta\theta} - \beta \right) \right) \frac{\mathbf{X}_C^{i,n+1} - \mathbf{X}_C^{i-1,n+1}}{|\mathbf{X}_C^{i,n} - \mathbf{X}_C^{i-1,n}|^2}
\end{aligned}$$

2.4 Simulation Results

Using the algorithm detailed in Section 2.3, we simulate cell blebbing in 2D. In this case, we removed a sector of adhesions to allow the bleb to form. As seen in Figure 2.17, after the adhesions are removed, allowing the cell membrane to expand. After some time, the cortex starts to recover and adhesions reform, tethering the membrane and cortex and allowing the membrane to retract.

In these preliminary results, there is a build-up of numerical error around the simulated cell membrane. This is likely due to the fact that the turnover model is very stiff. One possibility to resolve this is to incorporate a filter for the noise. Another option is to implement an implicit version of the IBM, although this could be computationally taxing. Osmotic pressure and bending forces on the membrane were included in an attempt to resolve this, but thus far we have not find a set of parameters that would allow the bleb to form and remove the noise.

With further work, this model can be used to study the combination of the turnover and computational fluid dynamics models to develop a stochastic model for cell blebbing in 2D.

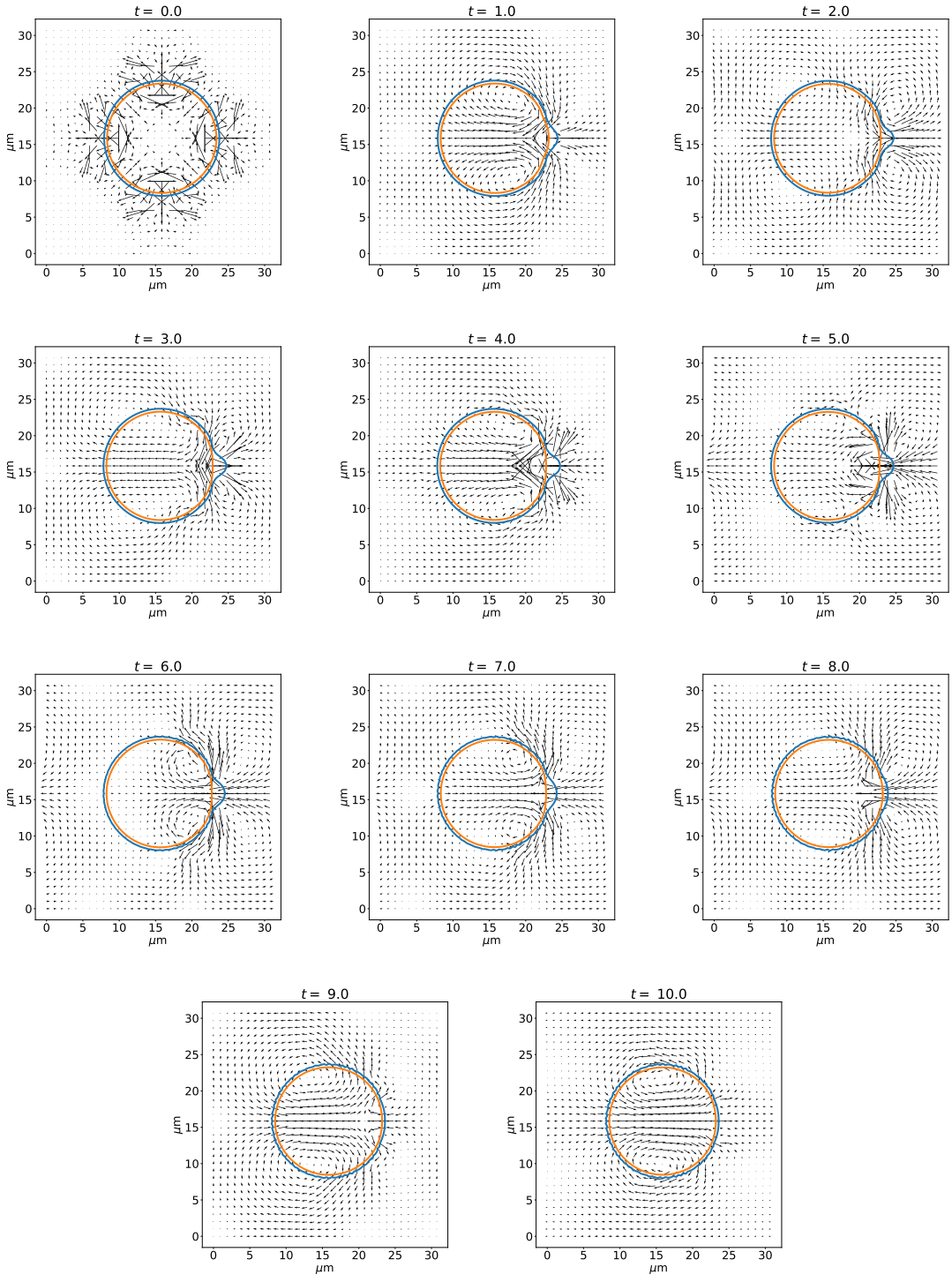

Figure 2.17: Sample 2D simulation showing the membrane and cortex locations, and the fluid flow field, as a bleb forms and heals back. Parameters are as listed in Table 2.5.

CHAPTER 3 : Cell Volume Control

3.1 Introduction

In this chapter, we discuss the modeling of cell volume control via a modified pump-leak model. Volume regulation in vertebrates involves the adjustment (in time scales from minutes to hours) of cellular volume in response to external challenges or during the execution of cellular functions. Biochemical reactions and equilibria depend on the concentrations of the molecules involved in the reactions, and so cells must avoid short-term changes in volume that will globally affect concentrations and interfere with cellular functions. Volume regulation is achieved in mammalian cells by transporting ions such as sodium, potassium and chloride, and small organic osmolytes, using plasma membrane channels and transporters. Some of these are shown in Figure 3.19. While most cells in mammals are protected from large osmotic disturbances, there are some, such as those in the gastrointestinal tract or distal kidney tubules, which can be exposed to large changes in osmolarity outside the cell. Furthermore, a pathological decrease in extracellular sodium ion levels (hyponatraemia) can lead to cerebral oedema. Sometimes, osmotic changes may also originate in the cytoplasm due for example to the breakdown of macromolecules into their building blocks [18]. The actual rate of osmotic cell swelling or shrinkage can vary between cell types because of differences in the water permeability of their plasma membranes.

Short-term regulatory volume changes (known as Regulatory Volume Decrease (RVD) and Regulatory Volume Increase (RVI)) require a fast reversal of the osmotic gradients that led to cell swelling or shrinkage respectively. There is a considerable redundancy of volume-regulatory effectors [18]. Here, we consider RVI through the combined use of Na^+/H^+ (such as NHE1) and Cl^-/HCO_3^- (AE) exchangers. These are activated by acidic pH. The exact mechanism by which NHE1 regulates cell volume remains elusive [52]. When cell shrinkage in induced by the medium, it is counteracted by the influx of sodium and chloride and the accompanying osmotic driven influx of water which generates cell swelling

to compensate. Throughout the RVI process, sodium is transported into the cell in exchange for protons mediated by NHE1. The net gain of sodium with negligible change in proton concentration results in a net osmotic gain due to the replacement of the extruded protons through a dissociation of cytosolic weak acids. The entrance of water comes after the influx of salt. The intracellular concentration of bicarbonate also increases because the membrane is somewhat permeable to carbon dioxide. This growth in bicarbonate concentration drives chloride into the cell via the anion exchanger (AE). This then leads to a combined gain of sodium and chloride while extruding protons and bicarbonate. These recombine in the extracellular space to produce water and carbon dioxide. This CO_2 can re-enter and diffuse into the cell and is thus osmotically irrelevant. The overall effect is that CO_2 is 'converted' to NaCl, which drives water into the cell. A schematic of this mechanism is shown in Figure 3.18. It appears that this is the primary mechanism driving RVI [52]. Another option for RVI involves $Na^+/K^+/2Cl^-$ (NKCC) cotransporters, which transport one sodium, one potassium and two chlorine ions into the cell, and is also electroneutral. NKCC is activated by cell shrinkage, and the influx of salt drives water into the cell, thus increasing the volume.

In this work, we develop a model of cell volume control including NHE and AE, as well as passive ion channels and reaction terms for the combination and dissociation of carbon dioxide and water. This model is based on the pump-leak model [28], and is thermodynamically consistent. We also model the sodium potassium pump (NaK-ATPase), which is active (requires energy from ATP) and is therefore necessary for the dynamics of the model. For the purpose of comparing the different possible mechanisms, we include also a model of the NKCC symporter. Each of the exchangers and symporters can act independently, thus allowing for a comparison of the effects of the different mechanisms for RVI.

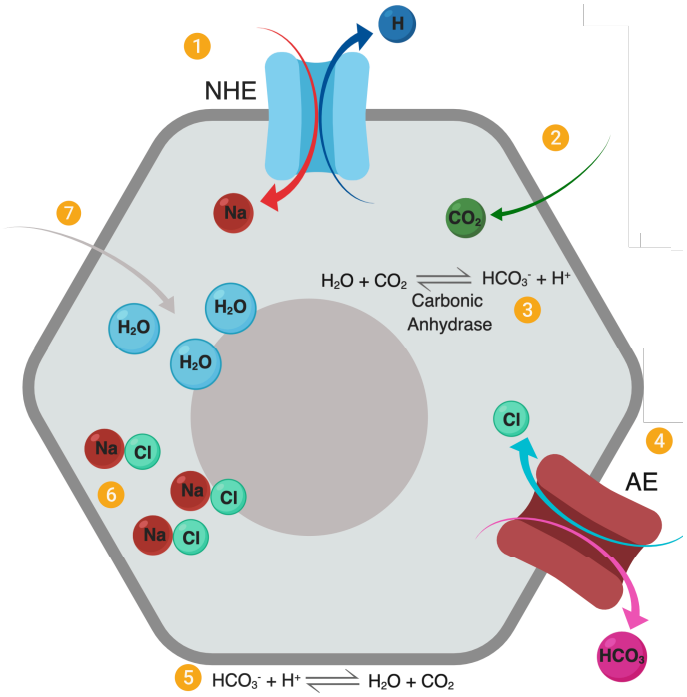

Figure 3.18: A schematic of the steps involved in RVI through the Na-H Exchanger mechanism.

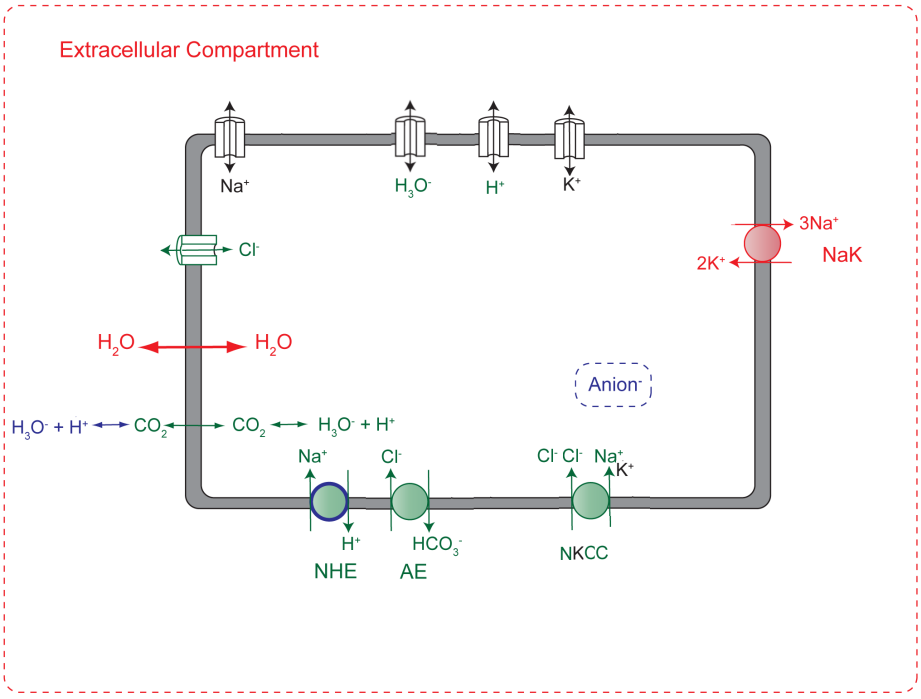

Figure 3.19: A schematic showing the main channels and transporters. We consider the Sodium-Hydrogen Exchanger, an Anion Exchanger, the NKCC cotransporter and permeable channels. Adapted from [37].

3.2 Model Formulation

In this Section, we formulate a system of ODEs based on the pump-leak model for cell volume. The main novel feature is the inclusion of CO_2, and the reaction catalysed by carbonic anhydrase.

Consider N species of ions and let c_k, $k = 1, \ldots, N$ be the intracellular concentration of the k-th species of ions. Let c_{CO_2} be the intracellular concentration of carbon dioxide. We let c_k^e, and c_{CO_2}, be the extracellular concentrations of these species, which are assumed to be positive and constant independent of time. Let v be the volume of the cell. The balance equation for the ions can be written as

$$\frac{d}{dt}(vc_k) = -J_k(\phi, \mathbf{c}, \mathbf{c}^e) - p_k(\phi, \mathbf{c}, \mathbf{c}^e) + R_k(\mathbf{c}), \qquad k = 1, \ldots, N. \tag{3.1}$$

Here, we have written the transmembrane flux as the sum of the passive fluxes J_k and the active flux p_k. The active flux, typically generated by ionic pumps requires energy expenditure from ATP, whereas the passive flux, carried by ionic channels and transporters, does not. The flux functions J_k and p_k depend on the transmembrane potential ϕ as well as the vector of intracellular and extracellular concentrations $\mathbf{c} = (c_1, \ldots, c_N)^T$ and $\mathbf{c}^e = (c_1^e, \ldots, c_N^e)^T$, where $\cdot^T$ denotes the transpose. We also have solute generation due to reactions R_k. Since $\mathbf{c}^e$ is assumed constant, it only appears as parameters in the above differential equation. We consider also dissolved carbon dioxide (CO_2), with balance equation:

$$\frac{d}{dt}(vc_{CO_2}) = -k(c_{CO_2} - c_{CO_2}^e) + \frac{c_{CO_2} - c_{CO_2}^e}{\ln \frac{c_{CO_2}}{c_{CO_2}^e}}(1 - \sigma_{CO_2})\frac{dv}{dt} + R_{CO_2}. \tag{3.2}$$

The derivation of 3.2, satisfying the Onsager reciprocity principle, is shown in Appendix B.1. We consider the following ions: H^+, Na^+, Cl^-, and HCO_3^-. The reversible reaction of

interest is

$$\mathrm{H_2O} + \mathrm{CO_2} \underset{\mathrm{k_{-1}}}{\overset{\mathrm{k_1}}{\rightleftharpoons}} \mathrm{H^+} + \mathrm{HCO_3}^-, \tag{3.3}$$

so we have the following generation due to the reaction:

$$\begin{aligned} R_w &= R_{CO_2} = -k_1 c_w c_{CO_2} + k_{-1} c_{H^+} c_{HCO_3^-} \\ R_{H^+} &= R_{HCO_3^-} = k_1 c_w c_{CO_2} - k_{-1} c_{H^+} c_{HCO_3^-} \\ R_{Na^+} &= R_{Cl^-} = 0 \end{aligned} \tag{3.4}$$

where k_1 and k_{-1} are the reaction rates in each direction, and we assume the concentration of water c_w to be constant, and neglect water throughout the model (fluctuations will be too small compared to the amounts of water).

The passive flux J_k has three parts:

$$J_k = r_k + j_k + s_k. \tag{3.5}$$

We have the Hodgkin-Huxley flux

$$r_k = g_k \left(F z_k \phi + RT \ln \left(\frac{c_k}{c_k^e} \right) \right), \tag{3.6}$$

where F is the Faraday constant, R is the ideal gas constant, and T is the temperature. We also have j_k, which refers to the NHE or AE exchangers. Following the work in [53], [46] and [28]:

$$\begin{aligned} j_{Na^+} &= -j_{H^+} = \frac{G_{Na^+H^+}(c_{Na^+} c^e_{H^+} - c^e_{Na^+} c_{H^+})}{K_{Na^+} K_{H^+} \Sigma_{Na^+H^+}} \\ j_{Cl^-} &= -j_{HCO_3^-} = \frac{G_{Cl^-HCO_3^-}(c_{Cl^-} c^e_{HCO_3^-} - c^e_{Cl^-} c_{HCO_3^-})}{K_{Cl^-} K_{HCO_3^-} \Sigma_{Cl^-HCO_3^-}} \end{aligned} \tag{3.7}$$

where

$$\Sigma_{kj} = \left(1 + \frac{c_k}{K_k} + \frac{c_j}{K_j}\right)\left(\frac{c_k^e}{K_k} + \frac{c_j^e}{K_j}\right) + \left(1 + \frac{c_k^e}{K_k} + \frac{c_j^e}{K_j}\right)\left(\frac{c_k}{K_k} + \frac{c_j}{K_j}\right); \tag{3.8}$$

here, K_i are dissociation constants, G_{jk} are the permeability coefficients for the antiporters. Finally, s_k refers to the NKCC symporter. Following the work in [17], s_k for K^+, Na^+, and Cl^-, is given by

$$s_k = P_s \frac{c^e_{Na^+} c^e_{K^+} (c^e_{Cl^-})^2 - c_{Na^+} c_{K^+} c^2_{Cl^-}}{\left(\frac{c_{Na^+}}{K^s_{Na^+}} + 1\right)\left(\frac{c_{K^+}}{K^s_{K^+}} + 1\right)\left(\frac{c_{Cl^-}}{K^s_{Cl^-}} + 1\right)^2}, \tag{3.9}$$

where P_s is the permeability coefficient of the NKCC symporter, and K^s_k are the saturability values for each ion k. We consider the active flux for sodium and potassium generated by the Na-K pump (ATPase) modeled by:

$$p_{Na^+} = 3p, \qquad p_{K^+} = -2p \tag{3.10}$$

where p is a small constant. This is the simplest model for p_k, used in simulations here, but more realistic ones will be explored in future work. As a convention, we take fluxes to be positive when they go from inside to outside the cell.

Equations 3.2 and 3.3 are supplemented by

$$0 = \sum_k F z_k c_k + F\frac{zA}{v} = \sum_k F z_k c^e_k, \tag{3.11}$$

$$\frac{dv}{dt} = -j_w(\mathbf{c}, \mathbf{c}^e, v), \tag{3.12}$$

where

$$j_w = \zeta(\pi_w + p_w) \tag{3.13}$$

with osmotic and hydraulic pressures

$$\pi_w = RT\left(\sum_k c_k^e - \left(\sum_k c_k + \frac{A}{v}\right) - \sigma_{CO_2}\left(c_{CO_2} - c_{CO_2}^e\right)\right), \qquad p_w = h(v). \tag{3.14}$$

Here, $\zeta > 0$ is the hydraulic conductivity of water through the membrane, $A > 0$ is the total amount of impermeable organic molecules inside the cell, with average valence z, and reflection coefficient σ_i.

It is also interesting to consider the fast reaction limit, where the reaction terms R_k and R_{CO_2} become constants that satisfy the algebraic constraint

$$c_{CO_2} = K c_{H^+} c_{HCO_3^-}, \tag{3.15}$$

where $K = \frac{k_{-1}}{k_1 c_w}$.

3.3 Free Energy Identity

In this Section, we show that the system described above satisfies a free energy identity. The fact that we can derive this identity shows that the model is thermodynamically consistent, and we have accounted for all the physics in the problem. It is also useful to find the energy used in volume regulation, and can be modified in future work to get a Lyapunov function to use in existence and stability of steady states.

Proposition 1. *Let v, c_k, c_{CO_2}, and ϕ, satisfy the model equations 3.1-3.12. Then, the following equality holds:*

$$\frac{d}{dt}(v\sigma) = -\pi_w j_w - \sum_k \mu_k J_k - k_{-1} c_{H^+} c_{HCO_3^-} (Q-1)\log Q, \tag{3.16}$$

where

$$\sigma = RT\left(\sum_k c_k\left(\ln\frac{c_k}{c_k^e} - 1\right) + c_k^e + c_A(\ln c_A - 1) + c_{CO_2}\left(\ln\frac{c_{CO_2}}{c_{CO_2}^e} - 1\right) + c_{CO_2}^e\right), \tag{3.17}$$

$Q = \frac{c_{CO_2}}{K c_{H^+} c_{HCO_3^+}}$, *and* $K = \frac{k_{-1}}{k_1 c_w}$ *is the reaction equilibrium constant.*

In the above, we have labeled fluxes by J_k for simplicity, and treat CO_2 the same way as the ions (with $z_{CO_2} = 0$).

Proof. We view σ as a function of c_k, c_{CO_2}, and c_A, with $c_A = \frac{A}{v}$. Note that

$$\frac{d}{dt}(vc_A) = \frac{dA}{dt} = 0. \tag{3.18}$$

Define the chemical potential

$$\mu_k = RT \ln \frac{c_k}{c_k^e} + F z_k \phi = \frac{\partial \sigma}{\partial c_k} + F z_k \phi \tag{3.19}$$

for charged solutes and CO_2, and

$$\mu_A = RT \ln c_A + F z \phi = \frac{\partial \sigma}{\partial c_A} + F z \phi, \tag{3.20}$$

for the impermeable anions. Multiply 3.1 by μ_k, 3.2 by $E_{CO_2} + \mu_{CO_2}$, and 3.18 by μ_A, and sum:

$$\sum_k \mu_k \frac{d}{dt}(vc_k) + \mu_A \frac{d}{dt}(vc_A) = -\mu_k (J_k - R_k) \tag{3.21}$$

The left hand side of 3.21 yields

$$\begin{aligned} &\sum_k \mu_k \frac{d}{dt}(vc_k) + \mu_A \frac{d}{dt}(vc_A) \\ &\qquad = \frac{d}{dt}(v\sigma) + \frac{dv}{dt}\left(\sum_k c_k \frac{\partial \sigma}{\partial c_k} + c_A \frac{\partial \sigma}{\partial c_A} - 2\sigma \right) \\ &\qquad = \frac{d}{dt}(v\sigma) - \pi_w \frac{dv}{dt} \end{aligned} \tag{3.22}$$

where we used 3.11, and the fact that

$$\pi_w = \sigma - \left(\sum_k c_k \frac{\partial \sigma}{\partial c_k} + c_A \frac{\partial \sigma}{\partial c_A} \right). \tag{3.23}$$

On the right hand side of 3.21, the reaction terms yield

$$-\sum_k \mu_k R_k = -k_{-1} c_{H^+} c_{HCO_3^-} (Q-1) \log Q, \tag{3.24}$$

where we used 3.11, and $Q = \frac{c_{CO_2}}{K c_{H^+} c_{HCO_3^+}}$, assuming that the reaction is in equilibrium outside the cell. □

3.4 Numerical Simulations

We perform simulations in Python 2.7. We used a backward Euler scheme, and linearized fluxes to get a linear system. The parameters used are in Appendix C.1, with any changes indicated in the corresponding figures. Some preliminary resultsare shown in Figure 3.20. We see that the fluxes affect the system in the way expected: both NHE and NKCC increase the volume, with NHE being somewhat more effective. Increasing the rate of the reaction also increases volume, as there is more CO_2 present. If we eliminate both the fluxes and the reaction, we see that the steady state volume is lower. It seems that the reaction has a greater effect. This could be because the reaction results in a higher osmolyte content, driving osmosis.

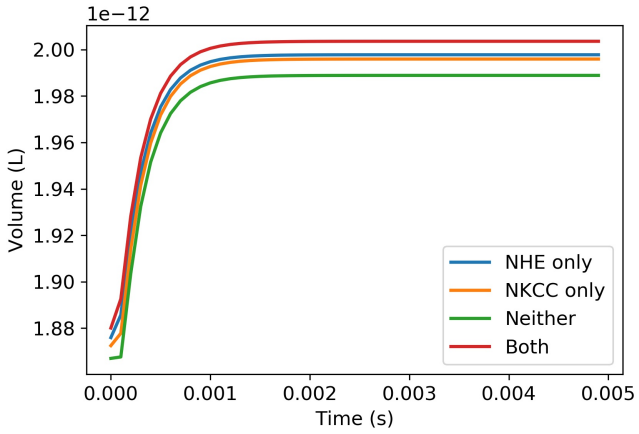

(a)

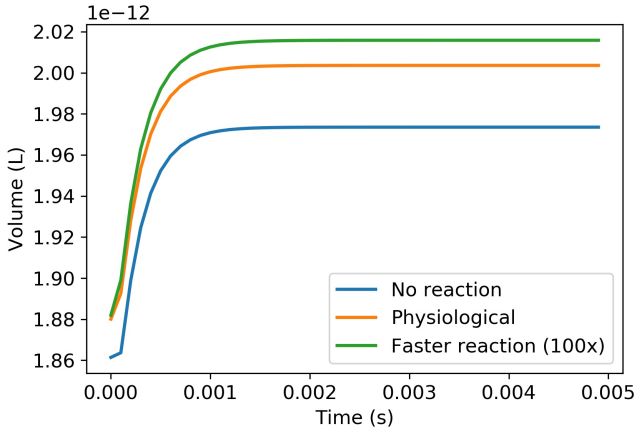

(b)

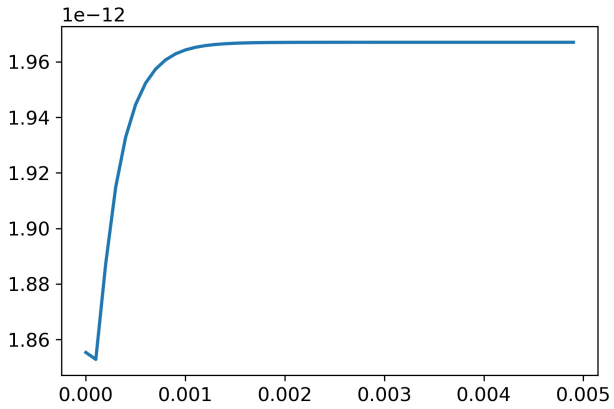

(c)

Figure 3.20: (a) Shows the results of the simultations when varying the channel fluxes present. (b) Shows the results of changing the reaction constants. (c) Shows the results when none of the new fluxes (NHE or NKCC) are present, and the reaction is also blocked.

3.5 Future Work

The next steps in this work will be to quantify the effect of modifying different aspects of the model, such as the amount of carbonic anhydrase (which catalyses the reaction), and the prevalence of different pumps and channels. We will also derive theoretical results concerning the existence and stability of the model, and the effect of the reaction on the steady state(s). It appears that the only published theoretical results related to this model are those shown in [28], but no reactions are considered in that work. The free energy identity in the previous section will be useful both to see how much energy is required with varying pumps, and as a Lyapunov function when looking for steady states.

CHAPTER 4 : Electrodiffusion and Actin-Driven Cell Migration

4.1 Introduction

There are currently two main approaches in biophysics that relate to the issue of cell migration. On the one hand, there is a purely mechanical approach built around the so-called 'treadmill model' ([44], [10], among others), in which the moving cell develops a protrusion at the leading edge using actin, adheres it to the surrounding matrix, removes the adhesion from the rear, and uses cytoskeletal contraction to pull the cell forward. On the other hand, there is the 'osmotic engine model', which describes a polarized cell moving by permeating water through the membrane [49]; this approach involves the flow of ions across the membrane. Evidence [22], [43] has further shown that electrodiffusion also plays an important role in cell migration. In particular, [22] presents results that show that without actin polymerization and myosin contraction, electric fields can also drive cell migration, even when the cell is not polarized.

We expect that cell functions such as migration are regulated by complex processes involving both mechanics and electrophysiology. For instance, there is experimental evidence showing that actin filaments undergo reorganization following membrane depolarization in bovine eye endothelial and epithelial cells, suggesting a functional role of membrane potential in cytoskeletal organization [3]. However, the interplay of mechanical and electrophysiological effects is not well understood. While the mechanics of cell division are known, for example, there is currently no explanation for the drastic changes in membrane potential during this process, with the cell becoming depolarized or hyperpolarized at different stages [3]. Another case where changes in membrane potential are not understood include the wide range of potentials that can be exhibited by cells: fully differentiated cells have a membrane potential of ~ -70mV, while embryonic cells are at ~ -10mV, and cancer cells can be ~ -30mV. Interestingly, cells with a lower potential rarely develop into cancer, and cells like heart cells never do. Right now, there is no satisfying explanation of why this is

the case.

There are several mathematical models that treat cell movement [44], [10]. These models focus on myosin contraction, adhesion, and actin polymerization. Also in the literature is the osmotic engine model, which describes a cell moving in a narrow 1D channel by permeating water through the cell, which must be polarized [49]. Ion fluxes and transmembrane potential have been incorporated with some success in models for eukaryotic cells, and have thus far been applied to cell volume control [36], [31], and tissue-level modelling of cortical spreading depression [29], but not to cell motion.

In this chapter we develop a system of partial differential equations (PDEs) to model cell migration in one dimension, combining an ionic electrodiffusion model with a cell movement model. We treat osmotic water flow, electrodiffusion, and actin polymerization in a unified framework with a deformable and capacitance-carrying membrane. The resulting system of equations is a highly coupled system of PDEs in a moving domain. Furthermore, this model possesses a thermodynamic structure, satisfying a free energy identity.

The framework described here can also be used to address other related problems such as understanding the role of certain proteins in cell volume control [52] or how cells move apart during cytokinesis [21].

The remainder of this Chapter is organised as follows. In Section 4.2, we introduce the model. In Section 4.3, we show that the model satisfies a free energy identity in which the sum of the entropic free energy, the elastic energy, and the actin network energy density are dissipated through bulk diffusion, transmembrane chemical fluxes, osmotic water flow, and network phase fluxes. In Section 4.5, we develop a computational scheme to simulate the system, and study its convergence.

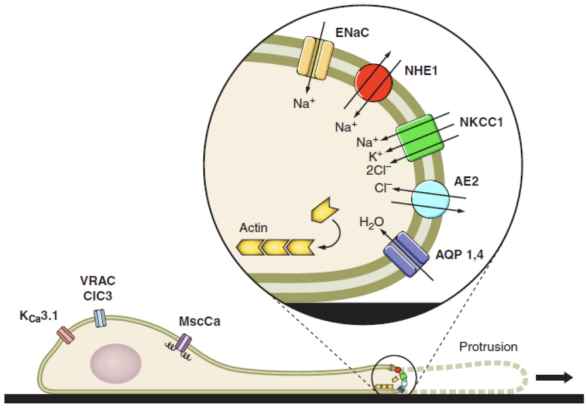

Figure 4.21: A schematic showing the role of ion channels in cell movement, from [42]. Different ion channels/water channels are expressed at the tip of a crawling cell, all of which affect cell movement.

4.2 1D Model Formulation

In this Section, we formulate a system of PDEs that governs the diffusion of electrolytes, actin polymerization, and osmotic water flow within a moving domain bounded by a membrane. The approach used here is similar to those in [31] and [30].

Consider a bounded domain $\Omega \subset \mathbb{R}$ where the cell lives. The cell membrane location is the set $\Gamma \subset \Omega$, which contains two points. The membrane divides Ω into three regions. Let $\Omega_i \subset \Omega$ be the intracellular region bounded by Γ, and let $\Omega_e \subset \Omega \setminus (\Omega_i \cap \Gamma)$ be the extracellular regions. We will denote the two immersed boundary points by X_f and X_b.

In the intracellular region, the unknowns will be the concentration of each ionic species c_k, $k = 1, \ldots, N$, the electrostatic potential ϕ, the concentration of the actin network phase θ, the fluid velocity u, and the hydrostatic pressure p. In the extracellular region, the unknowns will be u, p, c_k, and the electrostatic potential ϕ. Another unknown quantity is the membrane location $X(s,t)$ where s is the material coordinate of the membrane (or the actin cortex). We will denote the jump of a quantity α across the membrane by $[\alpha] = \alpha_{|\Gamma_i} - \alpha_{|\Gamma_e}$.

Let ω be the entropic part of the free energy per unit volume of this solution. Here, the following expression for ω is adopted:

$$\omega = \sum_{k=1}^{N} k_B T c_k \ln c_k, \tag{4.1}$$

where k_B is the Boltzmann constant, and T is temperature. This is valid when the ionic solution is sufficiently dilute and leads to linear diffusion of the solute.

Given ω, we can write the chemical potential of each species:

$$\mu_k = \frac{\partial \omega}{\partial c_k} + q z_k \phi = \sigma_k + q z_k \phi, \tag{4.2}$$

where q is the elementary charge, and z_k is the valence of species k.

Assuming electroneutrality, we can write the following algebraic condition:

$$\sum_{k=1}^{N} q z_k c_k = 0, \tag{4.3}$$

in Ω_i and Ω_e.

For the ionic concentration in Ω, we will have

$$\frac{\partial c_k}{\partial t} + u \frac{\partial c_k}{\partial x} = \frac{\partial}{\partial x} \left(c_k \frac{D_k}{k_B T} \frac{\partial \mu_k}{\partial x} \right), \tag{4.4}$$

where D_k is the diffusion coefficient of species k. Note that with the above choice of ω, we recover the Poisson-Nerst-Plank model. We shall impose Dirichlet boundary conditions on $\partial\Omega$. We have boundary conditions

$$\begin{aligned} -c_k \frac{D_k}{k_B T} \frac{\partial \mu_k}{\partial x} &= -f_w^f c_k + f_k^f \\ c_k \frac{D_k}{k_B T} \frac{\partial \mu_k}{\partial x} &= f_w^b c_k + f_k^b \end{aligned} \tag{4.5}$$

on X_f and X_b respectively, where f_k is the chemical flux through the membrane, and f_w is

the water flux through the membrane.

We now turn to the network phase concentration. This is modelled, in Ω_i, by

$$\frac{\partial \theta}{\partial t} + \frac{\partial}{\partial x}(\theta v) = 0 \tag{4.6}$$

subject to

$$\begin{aligned} \theta\left(\frac{\partial X_f}{\partial t} - v\right) &= j^f_{\text{actin}} \\ -\theta\left(\frac{\partial X_b}{\partial t} - v\right) &= j^b_{\text{actin}} \end{aligned} \tag{4.7}$$

at X_f and X_b. Here, v is the velocity of the network phase, which satisfies

$$-\frac{\partial \sigma}{\partial x} - \eta_s \theta v - \eta\theta(v-u) = 0, \tag{4.8}$$

where σ is the network pressure. We will assume that σ is of the form

$$\sigma = \sigma_n(\theta) + \sigma_a, \tag{4.9}$$

where σ_n and σ_a are the network and active parts respectively.

Now, we discuss force balance. Inside the cell, we use a Brinkman equation, which in one dimension reduces to

$$-\frac{\partial p}{\partial x} + \eta\theta(v-u) = 0, \tag{4.10}$$

where η is the friction coefficient between the actin network and the cytosolic fluid. Note that by incompressibility, u is constant in x. We impose the following boundary conditions on X_f and X_b:

$$\begin{aligned} \sigma + p - (p_\infty + d_g u) &= k(X_f - X_b) \\ \sigma + p - (p_\infty - d_g u) &= k(X_f - X_b) \end{aligned} \tag{4.11}$$

at X_f and X_b respectively, where d_g is the fluid drag coefficient and p_∞ is the pressure far from the cell. We also have

$$\begin{aligned} \frac{\partial X_f}{\partial t} - u &= -f_w^f \\ \frac{\partial X_b}{\partial t} - u &= f_w^b \end{aligned} \tag{4.12}$$

Note that the second condition is just the continuity condition.

We assume that the membrane capacitance $C_m(x)$ satisfies

$$C_m(x) = 0. \tag{4.13}$$

For the solute flux on X_f and X_b, we use the following constitutive relation:

$$f_k = j_k + a_k, \tag{4.14}$$

where j_k and a_k are the passive and active fluxes respectively. Some possible choices of j_k include

$$j_k^{HH} = g_k[\mu_k] = g_k k_B T[\ln c_k] + g_k z_k q[\phi], \tag{4.15}$$

$$j_k^{GHK} = P_k z_k \phi' \left(\frac{c_{k_{|\Gamma_i}} \exp(z_k \phi') - c_{k_{|\Gamma_e}}}{\exp(z_k \phi') - 1} \right), \qquad \phi' = \frac{q[\phi]}{k_B T}, \tag{4.16}$$

where g_k and P_k are positive and might depend on gating variables.

In the case of water flux, we let $f_w = j_w + a_w$ where j_w is passive flux, and a_w is active flux. One possibility for j_w is

$$j_w = -\zeta \left(N_A k_B T \sum_{k=1}^{N} [c_k] - [p] \right), \tag{4.17}$$

where N_A is Avogadro's number, and $\zeta = \frac{\partial j_w}{\partial [\psi_w]}_{|_{[\psi_w]=0}}$, with $[\psi_w] = [p] - [\pi_w]$, where $[\pi_w] = \sum_{k=1}^{N} [c_k] k_B T$ is the osmotic water pressure.

If we assume a constant amount of network actin, we must impose the condition

$$\sum_{\Gamma} j_{\text{actin}}\, dm_{\Gamma} = 0. \tag{4.18}$$

By convention, we take fluxes going from inside to outside the cell to be positive.

We further assume that the mechanical force is of the form

$$F_{\text{elastic}} = k(X_f - X_b), \tag{4.19}$$

and the capacitance force is

$$F_{\text{capacitance}} = 0. \tag{4.20}$$

4.3 Free Energy Identity

In this Section, we show that the system described above satisfies a free energy identity.

Theorem 1. *Suppose c_k, θ, p, v, X, and ϕ, are smooth functions that satisfy the equations and boundary conditions described in Section 4.2. Then, c_k, θ, p, v, X, and ϕ, satisfy the*

following free energy identity:

$$
\begin{aligned}
&\frac{d}{dt}(G + e_n + E_{elastic}) = -(I_f + I_n + I_m) + (J_n + J_m),\\
&G = \int_\Omega \omega \, dx, \qquad e_n = \int_{\Omega_i} e_n \, dx,\\
&I_f = \int_\Omega \sum_{k=1}^{N} c_k \frac{D_k}{k_B T} \left(\frac{\partial \mu_k}{\partial x}\right)^2 dx + 2 d_g u^2,\\
&I_n = \int_{\Omega_i} \eta_s \theta v^2 \, dx + \int_{\Omega_i} \eta \theta (v-u)^2 \, dx,\\
&I_m = \sum_{k=1}^{N} \big(([c_k]^f - (p_\infty + d_g u - p^{f,i}))f_w^f + ([c_k]^b\\
&\quad - (p_\infty - d_g u - p^{b,i}))f_w^b + [\mu_k]^f f_k^f + [\mu_k]^b f_k^b\big),\\
&J_n = \int_{\Omega_i} \sigma_a \frac{\partial v}{\partial x} \, dx,\\
&J_m = \frac{1}{\theta}(j_{actin}^f + j_{actin}^b)\sigma_a + \left(\frac{de_n}{d\theta}\right)^f j_{actin}^f + \left(\frac{de_n}{d\theta}\right)^b j_{actin}^b.
\end{aligned}
\tag{4.21}
$$

The identity 4.21 can be viewed as a free energy balance. The free energy consists of the contributions from entropy (G), the network energy density (e_n), and the membrane elasticity (E_{elastic}). The change in the free energy is through bulk fluxes (I_f), membrane fluxes (I_m), network phase fluxes (I_n), myosin contraction (J_n), and actin polymerization (J_m). The terms I_f, I_n, and I_m, are positive and represent a dissipation of free energy. The term J_n and J_m represent energy input.

Proof. Consider equation 4.4. Multiply by μ_k, integrate over Ω_i, and sum over k:

$$
\sum_{k=1}^{N} \int_{\Omega_i} \mu_k \frac{\partial c_k}{\partial t} \, dx + \sum_{k=1}^{N} \int_{\Omega_i} \mu_k u \frac{\partial c_k}{\partial x} \, dx = \sum_{k=1}^{N} \int_{\Omega_i} \mu_k \frac{\partial}{\partial x}\left(c_k \frac{D_k}{k_B T} \frac{\partial \mu_k}{\partial x}\right) dx. \tag{4.22}
$$

The right hand side is

$$
\int_{\Omega_i} \mu_k \frac{\partial}{\partial x}\left(c_k \frac{D_k}{k_B T} \frac{\partial \mu_k}{\partial x}\right) dx = \int_{\Gamma_i} \mu_k c_k \frac{D_k}{k_B T} \frac{\partial \mu_k}{\partial x} \, dm_\Gamma - \int_{\Omega_i} c_k \frac{D_k}{k_B T} \left(\frac{\partial \mu_k}{\partial x}\right)^2 dx
$$

Consider now the left hand side of 4.22:

$$\sum_{k=1}^{N} \mu_k \frac{\partial c_k}{\partial t} + \mu_k u \frac{\partial c_k}{\partial x} = \sum_{k=1}^{N} \frac{\partial \omega}{\partial c_k} \left(\frac{\partial c_k}{\partial t} + u \frac{\partial c_k}{\partial x} \right) = \frac{\partial \omega}{\partial x},$$

which, integrating over Ω_i gives

$$\int_{\Omega_i} \frac{\partial \omega}{\partial t} + u \frac{\partial \omega}{\partial x}\, dx = \int_{\Omega_i} \frac{\partial \omega}{\partial t}\, dx + \int_{\Gamma_i} \omega u\, dx = \frac{d}{dt} \int_{\Omega_i} \omega\, dx + \int_{\Gamma_i} \omega \left(u - \frac{\partial X}{\partial t} \right) dm_\Gamma$$

Performing a similar calculation over Ω_e and adding this to the above, we have

$$\begin{aligned} &\frac{d}{dt} \int_\Omega \omega\, dx + \int_\Gamma [\omega] \left(u - \frac{\partial X}{\partial t} \right) dm_\Gamma \\ &\qquad = \sum_{k=1}^{N} \int_\Gamma \left[\mu_k c_k \frac{D_k}{k_B T} \frac{\partial \mu_k}{\partial x} \right] dm_\Gamma - \sum_{k=1}^{N} \int_\Omega c_k \frac{D_k}{k_B T} \left(\frac{\partial \mu_k}{\partial x} \right)^2 dx. \end{aligned}$$

Using 4.11 and 4.12,

$$\begin{aligned} \frac{d}{dt} \int_\Omega \omega\, dx + ([\omega]^f f_w^f + [\omega^b] f_w^b) &= \sum_{k=1}^{N} [\mu_k (f_w^f c_k - f_k^f)]^f - [\mu_k (-f_w^b c_k + f_k^b)]^b \\ &\quad - \sum_{n=1}^{N} \int_\Omega c_k \frac{D_k}{k_B T} \left(\frac{\partial \mu_k}{\partial x} \right)^2 dx, \end{aligned}$$

so that

$$\begin{aligned} \frac{d}{dt} \int_\Omega \omega\, dx &= -[\omega]^b f_w^b - [\omega]^f f_w^f + \sum_{n=1}^{N} \left([\mu_k c_k]^f f_w^f - [\mu_k]^f f_k^f - [-\mu_k c_k]^b f_w^b - [\mu_k]^b f_k^b \right) \\ &\quad - \sum_{k=1}^{N} \int_\Omega c_k \frac{D_k}{k_B T} \left(\frac{\partial \mu_k}{\partial x} \right)^2 dx \\ &= \sum_{k=1}^{N} \left(-[\omega]^b f_k^b + [\mu_k c_k]^b f_w^b - [\omega]^f f_w^f + [\mu_k c_k]^f f_w^f - [\mu_k]^f f_k^f - [\mu_k]^b f_k^b \right) \\ &\quad - \sum_{k=1}^{N} \int_\Omega c_k \frac{D_k}{k_B T} \left(\frac{\partial \mu_k}{\partial x} \right)^2 dx. \end{aligned} \tag{4.23}$$

Note that

$$-[\omega] + [\mu_k c_k] = [c_k], \tag{4.24}$$

and so

$$\frac{d}{dt}\int_\Omega \omega\, dx = \sum_{k=1}^{N}\left(-[c_k]^b f_w^b - [c_k]^f f_w^f - [\mu_k]^f f_k^f - [\mu_k]^b f_k^b\right) - \sum_{k=1}^{N}\int_\Omega c_k \frac{D_k}{k_B T}\left(\frac{\partial \mu_k}{\partial x}\right)^2 dx. \tag{4.25}$$

Consider 4.8 and 4.10. Multiply them by v and u respectively and add:

$$\int_{\Omega_i}\left(-v\frac{\partial \sigma}{\partial x} - u\frac{\partial p}{\partial x}\right) dx = \int_{\Gamma_i} -v\sigma - up\, dm_\Gamma - \int_{\Omega_i} -\sigma\frac{\partial v}{\partial x}\, dx, \tag{4.26}$$

where we've used the fact that u is constant in x. At the front,

$$\begin{aligned} -v\sigma - up &= \frac{1}{\theta} j^f_{\text{actin}} - \frac{\partial X_f}{\partial t}\sigma - \left(\frac{\partial X_f}{\partial t} + f_w^f\right) p \\ &= \frac{1}{\theta} j^f_{\text{actin}}\sigma + f_w^f(p_\infty + d_g u - p) - d_g u^2 - p_\infty u - k(X_f - X_b)\frac{\partial X_f}{\partial t}, \end{aligned} \tag{4.27}$$

while at the back,

$$\begin{aligned} v\sigma + up &= \frac{1}{\theta} j^b_{\text{actin}}\sigma + \frac{\partial X_b}{\partial t}\sigma + \left(\frac{\partial X_b}{\partial t} - f_w^b\right) p \\ &= \frac{1}{\theta} j^b_{\text{actin}} + f_w^b(p_\infty - d_g u - p) - d_g u^2 + p_\infty u + k(X_f - X_b)\frac{\partial X_b}{\partial t}. \end{aligned} \tag{4.28}$$

Then, we have

$$\begin{aligned} &\frac{1}{\theta}({}^j f_{\text{actin}} + j^b_{\text{actin}})\sigma + f_w^f(p_\infty + d_g u - p) + f_w^b(p_\infty - d_g u - p) - 2d_g u^2 \\ &\qquad - k(X_f - X_b)\left(\frac{\partial X_f}{\partial t} - \frac{\partial X_b}{\partial t}\right) + \int_{\Omega_i}\sigma\frac{\partial v}{\partial x}\, dx = \int_{\Omega_i}\eta_s\theta v^2\, dx + \int_{\Omega_i}\eta\theta(v-u)^2\, dx, \end{aligned} \tag{4.29}$$

and

$$\frac{d}{dt}\left(\frac{1}{2}(X_f - X_b)^2\right) = \frac{1}{\theta}(j^f_{\text{actin}} + j^b_{\text{actin}})\sigma + f^f_w(p_\infty + d_g u - p) + f^b_w(p_\infty - d_g u - p) - 2d_g u^2 \\ - \int_{\Omega_i} \eta_s \theta v^2 \, dx - \int_{\Omega_i} \eta\theta(v-u)^2 \, dx + \int_{\Omega_i} \sigma \frac{\partial v}{\partial x} \, dx \tag{4.30}$$

We introduce a network energy density $e_n(\theta)$ satisfying

$$\theta \frac{de_n}{d\theta} - e_n = \theta^2 \frac{d}{d\theta}\left(\frac{e_n}{\theta}\right) = \sigma_n(\theta). \tag{4.31}$$

We have

$$\begin{aligned}
\frac{d}{dt}\int_{\Omega_i} e_n \, dx &= \int_{\Omega_i} \frac{\partial e_n}{\partial t} \, dx + \int_\Gamma e_n \frac{\partial X}{\partial t} \, dm_\Gamma = -\int_{\Omega_i} \frac{de_n}{d\theta}\frac{\partial}{\partial x}(\theta v) \, dx + \int_\Gamma e_n \frac{\partial X}{\partial t} \, dm_\Gamma \\
&= \int_{\Omega_i} v \frac{\partial \sigma_n}{\partial x} \, dx + \int_\Gamma -\sigma_n \frac{\partial X}{\partial t} + \frac{de_n}{d\theta}\theta\left(\frac{\partial X}{\partial t} - v\right) \, dm_\Gamma \\
&= \int_\Gamma v\sigma_n \, dm_\Gamma - \int_{\Omega_i} \sigma_n \frac{\partial v}{\partial x} \, dx + \int_\Gamma -\sigma_n \frac{\partial X}{\partial t} + \frac{de_n}{d\theta} j_{\text{actin}} \, dm_\Gamma \\
&= -\frac{1}{\theta} j^f_{\text{actin}} \sigma_n - \frac{1}{\theta} j^b_{\text{actin}} \sigma_n - \int_{\Omega_i} \sigma_n \frac{\partial v}{\partial x} \, dx + \left(\frac{de_n}{d\theta}\right)^f j^f_{\text{actin}} + \left(\frac{de_n}{d\theta}\right)^b j^b_{\text{actin}}.
\end{aligned} \tag{4.32}$$

Combining these results, we obtain 4.21. □

4.4 Linear Theory

In this Section, we solve the model equations at steady state. That is, we assume that the cell is moving at a constant speed

$$\frac{\partial X_f}{\partial t} = \frac{\partial X_b}{\partial t} = v_0, \tag{4.33}$$

and that the state of the cell is stationary with respect to the coordinate system moving at speed v_0. The cell has length $X_f - X_b = L$. We look for a closed-form expression for v_0.

Suppose $c_k = c_k^*$ are constant, and the fluxes $f_w = f_k = j_{\text{actin}} = 0$, so that the cell is at rest. Then,

$$v_0 = v = u = 0, \tag{4.34}$$

and $\theta = \theta^*$, $\sigma = \sigma^*$, $p = p^*$, and $\phi = \phi^*$ are all constant. We assume the following flux relation for the ion channel currents:

$$j_k^{b,f} = \sum_{l=1}^{N} G_{kl}\mu_l^{b,f}, \qquad \mu_l^{b,f} = \ln\left(\frac{c_l}{c_l^{b,f}}\right) + \frac{qz_l}{k_B T}(\phi - \phi^{b,f}). \tag{4.35}$$

Here, μ_l is the chemical potential difference across the membrane, and G_{kl} are constants. In matrix form, this can be written as

$$\mathbf{j}^{b,f} = G\boldsymbol{\mu}^{b,f}, \tag{4.36}$$

where G is the matrix whose entries are given by G_{kl}, $\mathbf{j}^{b,f} = (j_1^{b,f}, \ldots, j_N^{b,f})^T$ is the vector of ion channel currents and likewise for $\boldsymbol{\mu}^{b,f}$. The second law of thermodynamics asserts that $(G + G^T)/2$ must be positive definite, and Onsager reciprocity requires that G be symmetric. The above includes as a special case the relation 4.15, which we can write as

$$j_k^{b,f} = g_k\mu_k^{b,f}, \qquad g_k > 0. \tag{4.37}$$

In this case, G is diagonal. The added generality of 4.35 or 4.36 covers the case of passive membrane transporters such as the Na-K-Cl cotransporter. We take the pump currents to be constants:

$$a_k^f = a_k^b = \text{constant} = a_k^0. \tag{4.38}$$

This is a frequently used simplification which is justified if the substrate concentration is not low and ATP is found in abundance.

We let $-\frac{L}{2} < x < \frac{L}{2}$ rewrite equation 4.5 as

$$\begin{aligned} -D_k\left(\frac{\partial c_k}{\partial x} + \frac{qz_k}{k_BT}c_k\frac{\partial \phi}{\partial x}\right) &= -c_k f_w^f + f_k^f; \\ D_k\left(\frac{\partial c_k}{\partial x} + \frac{qz_k}{k_BT}c_k\frac{\partial \phi}{\partial x}\right) &= -c_k f_w^b + f_k^b; \end{aligned} \tag{4.39}$$

For steady state solutions, $\frac{\partial c_k}{\partial t} = 0$, and $(c_k v_0 + f_k)$ is a constant, where the fluxes f_k are constants to be determined. By convention, the flux is positive in the outward direction (from inside to outside the cell). We now impose a small active flux

$$\begin{aligned} a_k^b &= a_k^0 - \frac{\beta_k}{2} \\ a_k^f &= a_k^0 + \frac{\beta_k}{2,} \end{aligned} \tag{4.40}$$

where $\beta > 0$, $\beta \ll 1$. We want to know how the concentration, voltage, and velocity of the cell change under this small imposed difference. Let

$$c_k = c_k^* + d_k, \qquad \phi = \phi^* + \psi. \tag{4.41}$$

The functions d_k and ψ are deviations of the concentrations and voltage from c_k^* and ϕ^* respectively and are assumed small. The functions f_k and v_0 are small quantities, since their values is the absence of this small flux are 0. We now write all equations assuming these quantities are small (retain only terms that are linear in the small quantities). Equations 4.39 and 4.3 yield

$$-D_k\left(\frac{\partial d_k}{\partial x} + \frac{qz_k}{k_BT}c_k^*\frac{\partial \psi}{\partial x}\right) = -f_w c_k^* + f_k, \tag{4.42}$$

$$\sum_{k=1}^{N} z_k d_k = 0. \tag{4.43}$$

To obtain the second equation, we used

$$\sum_{k=1}^{N} z_k c_k^* = 0. \tag{4.44}$$

At steady state, we had

$$\sum_{l=1}^{N} G_{kl}\mu_l^{0,f} + a_k^0 = 0, \tag{4.45}$$

while now

$$f_k^f = \sum_{l=1}^{N} G_{kl}\mu_l^f + a_k^0 + \frac{\beta_k}{2}. \tag{4.46}$$

Subtracting these,

$$f_k^f = \sum_{l=1}^{N} G_{kl}\left(\ln\left(\frac{c_l^* + d_l^f}{c_l^*}\right) + \frac{qz_l}{k_BT}\psi^f\right) + \frac{\beta_k}{2}, \tag{4.47}$$

where $d_k^f = d_k(L/2)$, and we used $\phi^f = \phi^b = 0$. Since d_k^f is a small quantity, we can linearize further to get

$$f_k^f = \sum_{l=1}^{N} G_{kl}\left(\frac{d_l^f}{c_l^*} + \frac{qz_l}{k_BT}\psi^f\right) + \frac{\beta_k}{2}. \tag{4.48}$$

Similarly, we have

$$-f_k^b = \sum_{l=1}^{N} G_{kl}\left(\frac{d_l^b}{c_l^*} + \frac{qz_l}{k_BT}\psi^f\right) - \frac{\beta_k}{2}, \tag{4.49}$$

where $d_k^b = d_k(-L/2)$.

Now, let us solve for the deviations. Take the derivative of 4.43 with respect to x and use 4.42 to eliminate derivatives in d_k. Then

$$\left(\sum_{k=1}^{N} \frac{qz_k^2}{k_BT}c_k^*\right)\frac{\partial\psi}{\partial x} = -\sum_{k=1}^{N} \frac{z_k}{D_k}(f_k^f - f_w c_k^*). \tag{4.50}$$

This shows that ψ is a linear function of x. From this and 4.42 we also find that d_k are linear functions in x. By symmetry, we must have

$$d_k = \frac{2d_k^f}{L}x, \qquad \psi = \frac{2\psi^f}{L}x, \qquad d_k^b = -d_k^f, \qquad \psi^b = -\psi^f. \tag{4.51}$$

Substituting this back into 4.42, we have

$$-2\frac{D_k}{L}\left(d_k^f + \frac{qz_k}{k_BT}c_k^*\psi^f\right) + f_w c_k^* = \sum_{l=1}^{N} G_{kl}\left(\frac{d_l^f}{c_l^*} + \frac{qz_l}{k_BT}\psi^f\right) + \frac{\beta_k}{2}. \tag{4.52}$$

Define the matrix H whose entries H_{kl} are given by

$$H_{kl} = G_{kl} + 2\frac{D_k}{L}c_l^*\delta_{kl}, \tag{4.53}$$

where δ_{kl} is the Kronecker delta function. Using 4.48, we have

$$d_k^f + \frac{qz_k}{k_BT}c_k^*\psi^f = -\sum_{l=1}^{N}\left(-f_w(H^{-1})_{kl}c_l^* + (H^{-1})_{kl}\frac{\beta_l}{2}\right). \tag{4.54}$$

Summing over k,

$$\sum_{k=1}^{N} d_k^f = -\sum_{k=1}^{N}\sum_{l=1}^{N}\left(-f_w(H^{-1})_{kl}c_l^* + (H^{-1})_{kl}\frac{\beta_l}{2}\right), \tag{4.55}$$

and $d_k^b = -d_k^f$.

At steady state, to first order, 4.6 is

$$\frac{\partial}{\partial x}(\theta^* v) = 0, \tag{4.56}$$

and so v is constant in x. We also rewrite 4.8 and 4.10 to first order as

$$-\frac{\partial \sigma}{\partial x} - \eta_s\theta^* v - \eta\theta^*(v-u) = 0, \tag{4.57}$$

and

$$-\frac{\partial p}{\partial x} + \eta\theta^*(v-u) = 0. \tag{4.58}$$

Adding 4.57 and 4.58, and integrating, we have

$$-\int_{X_b}^{X_f}\left(\frac{\partial p}{\partial x}+\frac{\partial \sigma}{\partial x}\right)dx=\int_{X_b}^{X_f}\eta_s\theta^* v\,dx. \tag{4.59}$$

Since $\theta^* v$ is constant in x and using 4.11, we find

$$u=-\frac{\eta_s\theta^* L}{2d_g}v. \tag{4.60}$$

Also, by 4.7, given that v is constant, we must have

$$j^f_{\text{actin}}=-j^b_{\text{actin}}, \tag{4.61}$$

and

$$v=-\frac{j^f_{\text{actin}}}{\theta^*}+v_0, \tag{4.62}$$

$$u=\frac{\eta_s\theta^* L}{2dg}\left(\frac{j^f_{\text{actin}}}{\theta^*}-v_0\right). \tag{4.63}$$

Putting these into 4.58, we find that

$$p(x)=-\eta\left(1+\eta_s\frac{\theta^* L}{2d_g}\right)(j^f_{\text{actin}}-\theta^* v_0)x+B_p. \tag{4.64}$$

By 4.12,

$$-f^f_w=f^b_w, \tag{4.65}$$

assuming $a^f_w=a^b_w=a_w$, and fixing the outside concentration at c^*_k, we have

$$[p]^f=-[p]^b, \tag{4.66}$$

so

$$p^f-(p_\infty+d_g u)=-(p^b-(p_\infty-d_g u))\Rightarrow\frac{p^f+p^b}{2}=p^*, \tag{4.67}$$

and $B_p = p^*$. Hence,

$$[p]^f = -\eta \left(1 + \frac{\eta_s \theta^* L}{2 d_g}\right) (j^f_{\text{actin}} - \theta^* v_0) \frac{L}{2} - d_g u. \tag{4.68}$$

Assuming the outside concentration is fixed at c_k^*, we also have

$$\sum_{k=1}^{N} [c_k]^f = -\sum_{k=1}^{N} \sum_{l=1}^{N} \left(-f_w (H^{-1})_{kl} c_l^* + (H^{-1})_{kl} \frac{\beta_l}{2}\right). \tag{4.69}$$

Combining now 4.12, 4.63, 4.68, and 4.69, and solving for v_0, we find

$$v0 = \frac{-\frac{1}{2}\zeta N_A k_B T \langle \mathbf{e}, H^{-1}\boldsymbol{\beta}\rangle + \frac{j^f_{\text{actin}} L}{2}\left(\frac{\eta_s \theta^*}{d_g}(1 + \zeta N_A k_B T \langle \mathbf{e}, H^{-1}\mathbf{c}^*\rangle) + \zeta\left(\eta_s \theta^* + \eta\left(1 + \frac{\eta_s \theta^* L}{2 d_g}\right)\right)\right)}{\left(1 + \frac{\eta_s \theta^* L}{2 d_g}\right)(1 + \zeta N_A k_B T \langle \mathbf{e}, H^{-1}\mathbf{c}^*\rangle) + \zeta \frac{L\theta^*}{2}\left(\eta_s + \eta\left(1 + \frac{\eta_s \theta^* L}{2 d_g}\right)\right)} \tag{4.70}$$

4.5 Numerical Method

In this Section, we develop a numerical scheme that allows for the solution of the model equations. We use a splitting scheme for time stepping, alternating between the update of X, c_k and ϕ, σ and θ, and p. For each of these substeps, a backward Euler type time discretization is used. Computations were performed in Python 2.

Let L be the length of the domain, Δx be the spatial grid size, and N_x be the number of grid points so that $N_x \Delta x = L$. We let the time step be Δt. Let X_f^n, X_b^n, c_k^{ln}, ϕ^{ln}, σ^{ln}, θ^{ln}, p^{ln}, and u^n be the discretized values of X, c_k, ϕ, σ, θ, p and u at the l-th grid point at time $t = n\Delta t$.

To ensure stability, we use a CFL-type condition, requiring that Δt satisfy

$$\Delta t < \frac{1}{v_b} \Delta x, \tag{4.71}$$

where v_b is a characteristic velocity of the system - in this case, we have two possibilities:

the fluid velocity u, or the boundary velocity. We choose the more restrictive one of the two conditions.

We set initial conditions for c_k, θ, X_f and X_b. We assume the following relations to define σ:

$$\sigma_n(\theta) = -N_A k_B T \rho_0 \left(\frac{\theta_0}{\theta} - \frac{\theta}{2\theta_0} \right), \qquad \sigma_a(x) = k_a x, \tag{4.72}$$

where ρ_0 is the initial network density, k_a is the active network pressure flux, and θ_0 is the initial concentration θ. Thus, we can compute the initial value of σ. We can use equation 4.8 to find v and put it into 4.10 to obtain

$$-\frac{\partial p}{\partial x} - \frac{\eta}{\eta + \eta_s} \frac{\partial \sigma}{\partial x} + \left(\frac{\eta^2 \theta}{\eta + \eta_s} - \eta\theta \right) u = 0. \tag{4.73}$$

To find p and u at time $t = 0$, we discretize as follows:

$$\frac{p^{(l+1)0} - p^{l0}}{\Delta x} = \frac{\eta}{\eta + \eta_s} \left(\frac{\partial \sigma}{\partial x} \right)^{l0} - \left(\frac{\eta^2}{\eta + \eta_s} \theta^{l0} - \eta\theta^{l0} \right) u^0, \tag{4.74}$$

with boundary conditions

$$\begin{aligned} \sigma^{L0} + p^{L0} - (p_\infty + d_g u^0) &= k(X_f^0 - X_b^0), \\ \sigma^{R0} + p^{R0} - (p_\infty - d_g u^0) &= k(X_f^0 - X_b^0). \end{aligned} \tag{4.75}$$

We solve for p and u only in $X_b < x < X_f$.

Once we have initial values for all variables, we proceed as follows.

Step 1 In the first substep, we update the position of the moving boundaries X_f and X_b.

Combining equations 4.11, 4.12, and 4.17, we have

$$\begin{aligned} \frac{\partial X_f}{\partial t} &= u - \zeta \left[N_A k_B T \sum_{k=1}^{N} [c_k] - k(X_f - X_b) + \sigma \right] - a_w, \\ \frac{\partial X_b}{\partial t} &= u + \zeta \left[N_A k_B T \sum_{k=1}^{N} [c_k] - k(X_f - X_b) + \sigma \right] + a_w. \end{aligned} \tag{4.76}$$

We discretize this as

$$\begin{aligned} X_f^{n+1} &= X_f^n - \Delta t \left(-u^n + \zeta \left[N_A k_B T \sum_{k=1}^{N} [c_k] - k(X_f^n - X_b^n) + \sigma \right] - a_w \right), \\ X_b^{n+1} &= X_b^n + \Delta t \left(u^n + \zeta \left[N_A k_B T \sum_{k=1}^{N} [c_k] - k(X_f^n - X_b^n) + \sigma \right] - a_w \right). \end{aligned} \tag{4.77}$$

Step 2 In the second step, we compute the concentration of the ionic species c_k, and the electrostatic potential ϕ. We discretize equations 4.3 and 4.4 as follows:

$$\frac{c_k^{l(n+1)} - c_k^{ln}}{\Delta t} + u^n \frac{c_k^{(l+1)n} - c_k^{ln}}{\Delta x} = -\frac{1}{\Delta x}(f_k^{l+\frac{1}{2}} - f_k^{l-\frac{1}{2}}), \qquad u^n < 0 \tag{4.78}$$

$$\sum_k z_k c_k^{ln} = \sum_k z_k \frac{\Delta t}{\Delta x} \left(u^n (c_k^{(l+1)n} - c_k^{ln}) - (f_k^{l+\frac{1}{2}} - f_k^{l-\frac{1}{2}}) \right) \tag{4.79}$$

$$\frac{c_k^{l(n+1)} - c_k^{ln}}{\Delta t} + u^n \frac{c_k^{ln} - c_k^{(l-1)n}}{\Delta x} = -\frac{1}{\Delta x}(f_k^{l+\frac{1}{2}} - f_k^{l-\frac{1}{2}}), \qquad u^n > 0 \tag{4.80}$$

$$\sum_k z_k c_k^{ln} = \sum_k z_k \frac{\Delta t}{\Delta x} \left(u^n (c_k^{ln} - c_k^{(l-1)n}) - (f_k^{l+\frac{1}{2}} - f_k^{l-\frac{1}{2}}) \right) \tag{4.81}$$

where we obtained the modified electroneutrality condition by combining 4.3 and 4.4 before discretizing to achieve a more stable method than we would have by simply taking $\sum_k z_k c_k^{l(n+1)} = 0$, and

$$\begin{aligned} f_k^{l+\frac{1}{2}} &= -D_k \left(\frac{c_k^{(l+1)(n+1)} - c_k^{l(n+1)}}{\Delta x} + \frac{q z_k}{k_B T} \frac{c_k^{(l+1)n} + c_k^{ln}}{2} \frac{\phi^{(l+1)(n+1)} - \phi^{l(n+1)}}{\Delta x} \right), \\ f_k^{l-\frac{1}{2}} &= -D_k \left(\frac{c_k^{l(n+1)} - c_k^{(l-1)(n+1)}}{\Delta x} + \frac{q z_k}{k_B T} \frac{c_k^{ln} + c_k^{(l-1)n}}{2} \frac{\phi^{l(n+1)} - \phi^{(l-1)(n+1)}}{\Delta x} \right). \end{aligned} \tag{4.82}$$

Dirichlet boundary conditions are imposed at $\partial\Omega$ - note that for now, we do not have a clear reason to impose these conditions over others, but this ones are chosen solely for convenience and ease of implementation. Upwinding is necessary in the discretization

of the convective flux to achieve a stable scheme.

The grid points immediately before and after each boundary require a special treatment, as values are not continuous across the membrane. We use the quadratic interpolant described in [25] to obtain the solution at these points. On the left side of each boundary, we use

$$\hat{p}^{i+1} = \frac{2(1-\Delta^L)}{2+\Delta^L}p^{i-2} - \frac{3(1-\Delta^L)}{1+\Delta^L}p^{i-1} + \frac{6}{(1+\Delta^L)(2+\Delta^L)}p^L, \tag{4.83}$$

where the superscript L denotes the value at the boundary on the left hand side. Similarly, on the right side of each boundary, we use

$$\hat{p}^{i-1} = \frac{6}{(1+\Delta^R)(2+\Delta^R)}p^R - \frac{3(1-\Delta^R)}{1+\Delta^R}p^{i+1} + \frac{2(1-\Delta^R)}{1+\Delta^R}p^{i+2}, \tag{4.84}$$

where the superscript R denote the value at the boundary on the right hand side. Here, Δ^L is the remainder of $\frac{X^{n+1}}{\Delta x}$ and $\Delta^R = 1 - \Delta^L$. A schematic of this interpolation is shown in Figure 4.22.

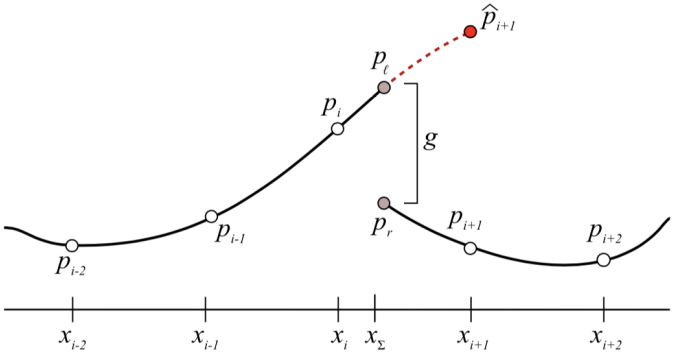

Figure 4.22: A schematic showing the interpolation for values across the membrane, from [25].

At the moving boundaries X_f and X_b, we have boundary conditions prescribed in 4.5.

At X_f, we have

$$\begin{aligned} f_k^{l+\frac{1}{2}} &= c_k^{L(n+1)} \left(\frac{X_f^{n+1} - X_f^n}{\Delta t} - u^n \right) - f_k^f, \\ f_k^{l-\frac{1}{2}} &= -c_k^{R(n+1)} \left(\frac{X_f^{n+1} - X_f^n}{\Delta t} - u^n \right) + f_k^f, \end{aligned} \tag{4.85}$$

where we evaluate $f_k^{l\pm\frac{1}{2}}$ at the points immediately before and after the boundary respectively. Similarly, at X_b, we have

$$\begin{aligned} f_k^{l-\frac{1}{2}} &= -c_k^{R(n+1)} \left(\frac{X_b^{n+1} - X_b^n}{\Delta t} - u^n \right) - f_k^b, \\ f_k^{l+\frac{1}{2}} &= c_k^{L(n+1)} \left(\frac{X_b^{n+1} - X_b^n}{\Delta t} - u^n \right) + f_k^b \end{aligned} \tag{4.86}$$

where we evaluate $f_k^{l\mp\frac{1}{2}}$ at the points immediately after and before the boundary respectively. Recall that we take the convention that the positive flux goes from inside to outside the cell. At these points, we use the simple electroneutrality condition

$$\sum_k z_k c_k^{l(n+1)} = 0. \tag{4.87}$$

We set the above up as a linear problem for efficiency. To improve stability, we create a block diagonal matrix by ordering the equations as $c_1^1, \ldots, c_N^1, \phi^1, c_1^2, \ldots, c_N^2, \phi^2, \ldots, c_1^{N_x}, \ldots, c_N^{N_x}, \phi^{N_x}$. Note that, as set above, the resulting matrix will be exactly singular, as adding any constant to the electrostatic potential ϕ will yield a solution. We hence set $\phi = 0$ at the right end of the domain by replacing the last equation in the system with this condition.

We consider two possibilities for j_k, and hence for f_k, introduced in equations 4.15 and 4.16. These are both non-linear, so in order to incorporate them into our linear

system, we use a linearization of these expressions. Thus, equation 4.15 becomes

$$j_k^{HH} \simeq g_k k_B T([\ln c_k]^n) + g_k z_k q([\phi]^{(n+1)}) + g_k k_B T \left(\frac{c_k^{i(n+1)}}{c_k^{in}} - \frac{c_k^{e(n+1)}}{c_k^{en}} \right), \tag{4.88}$$

where the superscripts i and e denote the interior and exterior of the boundary respectively. To avoid issues when $[\phi] \simeq 0$, we rewrite equation 4.16 as

$$j_k^{GHK} = P_k \frac{x_k}{\sinh(x_k)} [c_k^i \exp(x_k) - c_k^e \exp(-x_k)] \tag{4.89}$$

where $x_k = \frac{z_k q[\phi]}{2k_B T}$. Then, the linearization is

$$\begin{aligned} j_k^{GHK} = &\left(\frac{\partial j_k^{GHK}}{\partial c_k^i} \right)^n c_k^{i(n+1)} + \left(\frac{\partial j_k^{GHK}}{\partial c_k^e} \right)^n c_k^{e(n+1)} \\ &+ \frac{q}{k_B T} \left(\frac{\partial j_k^{GHK}}{\partial \tilde{\phi}} \right)^n (\phi^{i(n+1)} - \phi^{e(n+1)} - [\phi]^n) \end{aligned} \tag{4.90}$$

where $\tilde{\phi} = \frac{q[\phi]}{k_B T}$

$$\begin{aligned} \frac{\partial j_k^{GHK}}{\partial \tilde{\phi}} &= \frac{z_k}{2} \left(j_k^{GHK} \frac{x_k}{\sinh x_k} w_k + c_k^i \frac{\partial j_k^{GHK}}{\partial c_k^i} - c_k^e \frac{\partial j_k^{GHK}}{\partial c_k^e} \right), \\ w_k &= \frac{1}{x_k} \left(\frac{\sinh x_k}{x_k} - \cosh x_k \right). \end{aligned}$$

In this second case, for j_k^{GHK}, we need to know the value of $[\phi]$ at time $t = 0$. However, we do not set initial conditions on ϕ, so in order to use this expression for the flux we would need to solve the system for c_k and ϕ at $t = 0$. Since we set initial conditions for the concentrations c_k, we only need to solve the nonlinear system for ϕ. We do this using Newton's method as follows: we take equation 4.4, multiply by z_k and sum over k, so that it becomes

$$\sum_k z_k \frac{\partial}{\partial x} \left(D_k \left(\frac{\partial c_k}{\partial x} + z_k c_k \frac{\partial \phi}{\partial x} \right) \right) = 0. \tag{4.91}$$

Our discretization is then

$$\sum_k z_k \frac{1}{\Delta x}(f_k^{l+\frac{1}{2}} - f_k^{l-\frac{1}{2}}) = 0, \tag{4.92}$$

where

$$\begin{aligned} f_k^{l+\frac{1}{2}} &= -D_k \left(\frac{c_k^{(l+1)} - c_k^l}{\Delta x} + \frac{qz_k}{k_B T} \frac{c_k^{(l+1)} + c_k^{ln}}{2} \frac{\phi^{(l+1)} - \phi^l}{\Delta x} \right), \\ f_k^{l-\frac{1}{2}} &= -D_k \left(\frac{c_k^l - c_k^{(l-1)}}{\Delta x} + \frac{qz_k}{k_B T} \frac{c_k^{ln} + c_k^{(l-1)}}{2} \frac{\phi^l - \phi^{(l-1)}}{\Delta x} \right), \end{aligned} \tag{4.93}$$

with all quantities evaluated at time 0. At $\partial\Omega$, we have $f_k^{l+\frac{1}{2}} = 0$ at $x = 0$ and $f_k^{l-\frac{1}{2}} = 0$ at $x = L$. For the moving boundaries X, we have

$$\sum_k z_k D_k f_k^{l\pm\frac{1}{2}} + \sum_k z_k f_k = 0. \tag{4.94}$$

Once we have values at $t = 0$ for ϕ, we proceed as before, solving a linear system for all subsequent time steps.

Step 3 In this third step, we solve for the network phase concentration. Rearranging equation 4.8, we can write

$$\theta v = \frac{\eta}{\eta + \eta_s}\theta u - \frac{1}{(\eta + \eta_s)} \frac{\partial \sigma}{\partial \theta} \frac{\partial \theta}{\partial x}, \tag{4.95}$$

so that the equation for the conservation of the network phase 4.6 becomes

$$\frac{\partial \theta}{\partial t} + \frac{\partial}{\partial x}\left(\frac{\eta}{\eta + \eta_s}\theta u - \frac{1}{(\eta + \eta_s)} \frac{\partial \sigma}{\partial \theta} \frac{\partial \theta}{\partial x} \right) = 0. \tag{4.96}$$

Assume σ is of the form 4.9 with σ_n and σ_a as in 4.72. Then, under the assumption that $k_a = 0$ (and therefore that $\sigma_a = 0$),

$$\theta(\sigma_n) = \frac{\theta_0}{N_A k_B T \rho_0} \left(\sigma_n + \sqrt{2(N_A k_B T \rho_0)^2 + \sigma_n^2} \right), \tag{4.97}$$

and

$$\frac{d\theta}{d\sigma_n} = \frac{\theta_0}{N_A k_B T \rho_0}\left(1 + \frac{\sigma_n}{\sqrt{2(N_A k_B T \rho)^2 + \sigma_n^2}}\right). \tag{4.98}$$

Thus, we can solve

$$\frac{\partial \sigma_n}{\partial t} + \frac{\eta}{\eta+\eta_s} u \frac{\partial \sigma_n}{\partial x} - \frac{1}{\eta+\eta_s}\left(\frac{d\theta}{d\sigma_n}\right)^{-1} \frac{\partial^2 \sigma_n}{\partial x^2} = 0, \tag{4.99}$$

with boundary conditions

$$\begin{aligned} \theta(\sigma_n)\left(\frac{\partial X_f}{\partial t} - \frac{\eta}{\eta+\eta_s}u\right) + \frac{1}{\eta+\eta_s}\frac{d\sigma_n}{dx} &= -\frac{1}{\eta+\eta_s}\frac{d\sigma_a}{dx} + j^f_{\text{actin}} \\ -\theta(\sigma_n)\left(\frac{\partial X_b}{\partial t} - \frac{\eta}{\eta+\eta_s}u\right) - \frac{1}{\eta+\eta_s}\frac{d\sigma_n}{dx} &= -\frac{1}{\eta+\eta_s}\frac{d\sigma_a}{dx} + j^b_{\text{actin}} \end{aligned} \tag{4.100}$$

at X_f, X_b.

We discretize equation 4.99 as

$$\begin{aligned} \frac{\sigma_n^{l(n+1)} - \sigma_n^{ln}}{\Delta t} + \frac{\eta}{\eta+\eta_s}u^n \frac{\sigma_n^{(l+1)n} - \sigma_n^{ln}}{\Delta x} &= -\frac{1}{\Delta x}(g^{l+\frac{1}{2}} - g^{l-\frac{1}{2}}), && u^n < 0 \\ \frac{\sigma_n^{l(n+1)} - \sigma_n^{ln}}{\Delta t} + \frac{\eta}{\eta+\eta_s}u^n \frac{\sigma_n^{ln} - \sigma_n^{(l-1)n}}{\Delta x} &= -\frac{1}{\Delta x}(g^{l+\frac{1}{2}} - g^{l-\frac{1}{2}}), && u^n > 0 \end{aligned} \tag{4.101}$$

where

$$\begin{aligned} g^{l+\frac{1}{2}} &= -\frac{1}{\eta+\eta_s}\left(\left(\frac{\partial\theta}{\partial\sigma_n}\right)^{-1}\right)^{ln} \frac{\sigma_n^{(l+1)(n+1)} - \sigma_n^{l(n+1)}}{\Delta x}, \\ g^{l-\frac{1}{2}} &= -\frac{1}{\eta+\eta_s}\left(\left(\frac{\partial\theta}{\partial\sigma_n}\right)^{-1}\right)^{ln} \frac{\sigma_n^{l(n+1)} - \sigma_n^{(l-1)(n+1)}}{\Delta x}. \end{aligned} \tag{4.102}$$

For the boundary conditions at X_f and X_b, we have

$$\begin{aligned}\frac{1}{\eta+\eta_s}\frac{\sigma_n^{l(n+1)}-\sigma_n^{(l-1)(n+1)}}{\Delta x} &= -\frac{1}{\eta+\eta_s}k_a + j^f_{\text{actin}} \\ &\quad - \theta(\sigma_n)^{Ln}\left(\frac{X_f^{n+1}-X_f^n}{\Delta t} - \frac{\eta}{\eta+\eta_s}u^n\right) \\ \frac{1}{\eta+\eta_s}\frac{\sigma_n^{(l+1)(n+1)}-\sigma_n^{l(n+1)}}{\Delta x} &= -\frac{1}{\eta+\eta_s}k_a - j^b_{\text{actin}} \\ &\quad - \theta(\sigma_n)^{Rn}\left(\frac{X_b^{n+1}-X_b^n}{\Delta t} - \frac{\eta}{\eta+\eta_s}u^n\right),\end{aligned} \tag{4.103}$$

where we set l as the point just before and after the boundary respectively. Again, this discretization allows us to solve a linear system.

Once we have σ_n, we can get θ from equation 4.97, and σ from 4.9 and 4.72.

Step 4 In the last step, we solve for the hydrostatic pressure p and the fluid velocity u. We discretize 4.73 as

$$\frac{p^{(l+1)(n+1)}-p^{l(n+1)}}{\Delta x} = -\frac{\eta}{\eta+\eta_s}\left(\frac{\partial\sigma}{\partial x}\right)^{l(n+1)} + \left(\frac{\eta^2}{\eta+\eta_s}\theta^{l(n+1)} - \eta\theta^{l(n+1)}\right)u^{n+1} \tag{4.104}$$

with boundary conditions

$$\begin{aligned}\sigma^{L(n+1)} + p^{L(n+1)} - (p_\infty + d_g u^{n+1}) &= k(X_f^{n+1} - X_b^{n+1}) \\ \sigma^{R(n+1)} + p^{R(n+1)} - (p_\infty - d_g u^{n+1}) &= k(X_f^{n+1} - X_b^{n+1})\end{aligned} \tag{4.105}$$

at X_f and X_b respectively. On the front end of the cell (point labeled R), we approximate its value by the value just before the boundary (R_a):

$$\sigma^{(R_a(n+1))} + p^{R_a(n+1)} - (p_\infty - d_g u^{n+1}) = k(X_f^{n+1} - X_b^{n+1}). \tag{4.106}$$

At the back end of the cell, we use an interpolation as described in Step 2. Again, we solve for p and u only in $X_b < x < X_f$.

4.5.1. Convergence Study

In this section, we look at the behavior of the method described in Step 2 to compute c_k and ϕ. Rather than solving the complete model, we set sinusoidal moving boundaries

$$X_b(t) = 0.4 - 0.3\sin(t), \qquad X_f(t) = 0.6 - 0.3\sin(t), \tag{4.107}$$

and solve only for c_k and ϕ. In order to avoid the use of a non-linear solver at $t = 0$, we use j_k^{HH}.

Suppose that the true solution to the electrodiffusion equations as above is $c_{1,\infty}$, and that

$$||c_{1,2^l} - c_{1,2^{l+1}}||_{L^\infty} \leq \frac{c}{2^{lk}} \tag{4.108}$$

$\forall l$, where k is the order of the scheme, and the second index for the concentration gives the number of grid points. Then,

$$\begin{aligned}
||c_{1,2^l} - c_{1,\infty}|| &= ||c_{1,2^l} - c_{1,2^{l+1}} + c_{1,2^{l+1}} - c_{1,2^{l+2}} + \dots|| \\
&\leq \sum_{m=0}^{\infty} ||c_{1,2^{l+m}} - c_{1,2^{l+m-1}}|| \\
&\leq \sum_{m=0}^{\infty} \frac{\alpha}{2^{(l+m)k}} = \frac{\alpha}{2^{lk}} \left(\frac{1}{1-2^{-k}}\right) \\
&= \tilde{\alpha} \left(\frac{1}{2^l}\right)^k.
\end{aligned}$$

Suppose $||c_{1,N} - c_{1,\infty}||_{L^\infty}$ is monotone decreasing. Then,

$$\log_2 \frac{||c_{1,2^l} - c_{1,2^{l+1}}||_{L^\infty}}{||c_{1,2^{l+1}} - c_{1,2^{l+2}}||_{L^\infty}} = k. \tag{4.109}$$

We fix Δt to satisfy the CFL condition in the most restrictive case (for the finest grid), and run for a total simulation time $T = 1$. We then vary Δx. The results are displayed in Table 4.6.

l	$\max(\lvert c_{1,2^l} - c_{1,2^{l+1}} \rvert)$	k
6	0.125320	0.988260
7	0.063172	0.990485
8	0.031795	0.990638
9	0.016001	–

Table 4.6: Table showing that the order of convergence of our scheme is $k \simeq 1$.

4.5.2. Simulation Results

In this Section, we show some results of the complete simulations. Figure 4.23 shows the positions of the boundaries initially and after running the simulation, while Figure 4.24 shows the profiles of an ionic concentration and of the network concentration at different times.

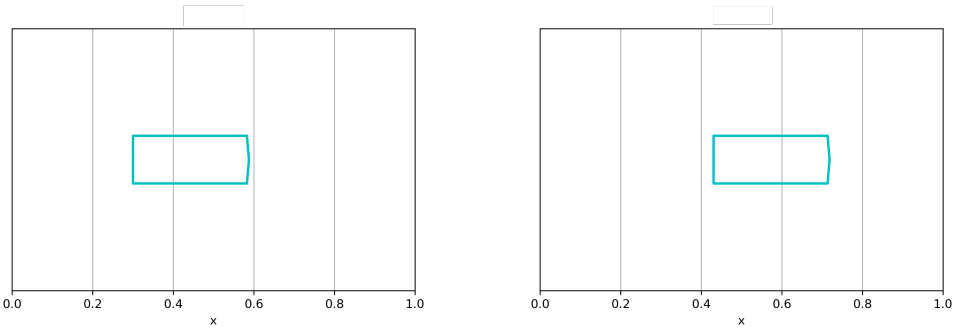

(a) $t = 0$ (b) $t = 2$

Figure 4.23: Cell position at the start and end of the simulation with total time $t = 2$. (This figure shows the position of the boundaries, the rectangles are otherwise artificial).

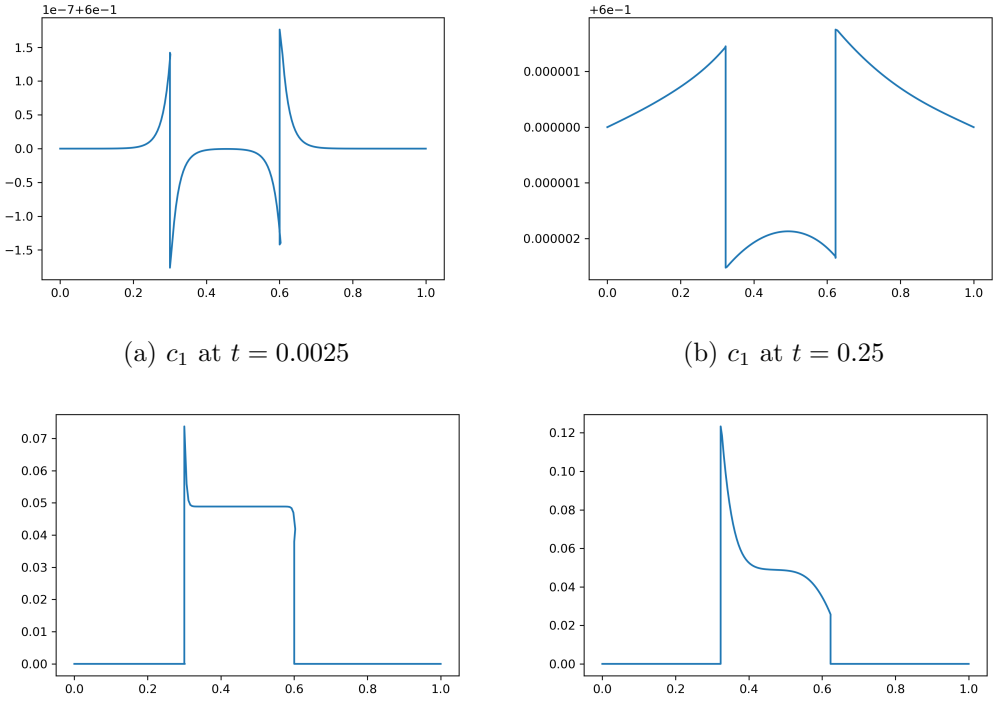

(a) c_1 at $t = 0.0025$

(b) c_1 at $t = 0.25$

(c) θ at $t = 0.0025$

(d) θ at $t = 0.25$

Figure 4.24: Concentration profiles for ion 1 (c_1) and network (θ) at times $t = 0.0025$ and $t = 0.25$.

4.6 2D Model Formulation

In this section, we develop the 2D model that will form the basis of the continuation of this work.

Consider now a bounded domain $\Omega \subset \mathbb{R}^2$ where the cell lives. The cell membrane location is the smooth closed surface $\Gamma \subset \Omega$. The membrane divides Ω into two regions. Let $\Omega_i \subset \Omega$ be the intracellular region bounded by Γ, and let $\Omega_e \subset \Omega \setminus (\Omega_i \cap \Gamma)$ be the extracellular region.

In the intracellular region, the unknowns will be the concentration of each ion species c_k, $k = 1, \ldots, N$, the electrostatic potential ϕ, the concentration of the actin network phase θ, the fluid velocity $\mathbf{u}$, and the hydrostatic pressure p. In the extracellular region, the unknowns will be $\mathbf{u}$, p, c_k, and ϕ. Another unknown quantity is the membrane location

$\mathbf{X}(s,t)$ where s is the material coordinate of the membrane (or the actin cortex). As before, we will denote the jump of a quantity α across the membrane by $[\alpha] = \alpha_{|\Gamma_i} - \alpha_{|\Gamma_e}$.

We retain equations 4.1 and 4.2. For the electrostatic potential in Ω_i and Ω_e, we still have electroneutrality

$$0 = \sum_{k=1}^{N} q z_k c_k. \tag{4.110}$$

Similarly, equation 4.4 becomes

$$\frac{\partial c_k}{\partial t} + \nabla \cdot (\mathbf{u} c_k) = \nabla \cdot \left(c_k \frac{D_k}{k_B T} \nabla \mu_k \right) \tag{4.111}$$

in Ω_i, Ω_e, with boundary conditions

$$\nabla \cdot \left(c_k \frac{D_k}{k_B T} \nabla \mu_k \right) = 0 \tag{4.112}$$

on $\partial\Omega$, and

$$c_k \left(\mathbf{u} - \frac{D_k}{k_B T} \nabla \mu_k \right) \cdot \mathbf{n} = c_k \frac{\partial \mathbf{X}}{\partial t} \cdot \mathbf{n} + f_k \tag{4.113}$$

on Γ_i, Γ_e.

For the network concentration, we modify 4.6 to get

$$\frac{\partial \theta}{\partial t} + \nabla \cdot (\theta \mathbf{v}) = 0 \tag{4.114}$$

in Ω_i, with boundary condition

$$\theta \left(\frac{\partial \mathbf{X}}{\partial t} - \mathbf{v} \right) \cdot \mathbf{n} = j_{\text{actin}} \tag{4.115}$$

on Γ_i. Here, $\mathbf{v}$ is the velocity of the network phase, which satisfies

$$\nabla \sigma - \eta \theta (\mathbf{u} - \mathbf{v}) - \eta_s \theta \mathbf{v} = 0. \tag{4.116}$$

Assuming a constant amount of actin, we must impose the condition

$$\int_{\Gamma} j_{\text{actin}}\, dm_{\Gamma} = 0. \tag{4.117}$$

Outside the cell, in Ω_e, we model the force balance by the incompressible Stoke's equations of fluid flow with an electrostatic force term:

$$\begin{cases} \nabla \cdot (\Sigma_m(\mathbf{u}, p)) = 0 \\ \nabla \cdot \mathbf{u} = 0 \end{cases} \tag{4.118}$$

Inside the cell, in Ω_i, we use again a Brinkmann equation with an electrostatic force term:

$$\begin{cases} \nabla \cdot (\Sigma_m(\mathbf{u}, p)) - \eta\theta(\mathbf{u} - \mathbf{v}) = 0 \\ \nabla \cdot \mathbf{u} = 0 \end{cases} \tag{4.119}$$

Here, Σ_m is the mechanical stress tensor

$$\Sigma_m(\mathbf{u}, p) = \nu(\nabla \mathbf{u} + (\nabla \mathbf{u}))^T) - pI, \tag{4.120}$$

where ν is the viscosity of the electrolyte solution, $(\nabla \mathbf{u})^T$ is the transpose of $\nabla \mathbf{u}$, and I is the identity matrix. Together with these, we have the following boundary conditions:

$$[\mathbf{u}] = 0 \tag{4.121}$$

on $\partial\Omega$ (no-slip),

$$[(\Sigma_m(\mathbf{u}, p))\, \mathbf{n}] = -\sigma \mathbf{n} + \mathbf{F}_{\text{elastic}}, \qquad \text{on } \Gamma_i, \Gamma_e, \tag{4.122}$$

on Γ_i and Γ_e, and the continuity condition

$$\mathbf{u} - \frac{\partial \mathbf{X}}{\partial t} = f_w \mathbf{n}, \qquad \text{on } \Gamma_i, \Gamma_e \tag{4.123}$$

on Γ_i and Γ_e. We assume that the mechanical force can be derived from an energy functional

$$E_{\text{membrane}}(\mathbf{X}) = \int_{\Gamma_{\text{ref}}} \mathcal{E}(\mathbf{X})\, dm_{\Gamma_{\text{ref}}}, \tag{4.124}$$

where $\mathcal{E}$ is the elastic energy density measured with respect to $m_{\Gamma_{\text{ref}}}$, the surface measure of Γ_{ref}. Then, $\mathbf{F}_{\text{membrane}}$ satisfies

$$\frac{d}{dt} E_{\text{membrane}}(\mathbf{X}) = -\int_{\Gamma} \mathbf{F}_{\text{membrane}} \cdot \frac{\partial \mathbf{X}}{\partial t}\, dm_{\Gamma}. \tag{4.125}$$

4.6.1. Free Energy Identity

Combining the work in [31], and [30], we have

$$\begin{aligned}
&\frac{d}{dt}\left(\int_{\Omega_i \cup \Omega_e} \omega\, d\mathbf{x} + \int_{\Gamma_{\text{ref}}} \mathcal{E}(\mathbf{X})\, dm_{\Gamma_{\text{ref}}} + \int_{\Omega_i} e_n\, d\mathbf{x}\right) \\
&\quad = -\int_{\Omega_i \cup \Omega_e} \left(2\nu |\nabla_S \mathbf{u}|2 + \sum_{k=1} N c_k \frac{D_k}{k_B T} |\nabla \mu_k|2\right) d\mathbf{x} \\
&\qquad - \int_{\Gamma} \left([\psi_w] f_w + \sum_{k=1} N[\mu_k] f_k\right) dm_{\Gamma} \\
&\qquad + \int_{\Gamma} \left(-\sigma \frac{\partial \mathbf{X}}{\partial t} \cdot \mathbf{n} + \left(\frac{de_n}{d\theta} + \frac{\sigma_a}{\theta}\right) j_{\text{actin}}\right) dm_{\Gamma} \\
&\qquad + \int_{\Omega_i} \sigma_a \nabla \cdot \mathbf{v} + \mathbf{v} \cdot (\eta\theta(\mathbf{u} - \mathbf{v}) - \eta_s \theta \mathbf{v})\, d\mathbf{x}.
\end{aligned} \tag{4.126}$$

4.6.2. Numerical Method

The next step will be to develop a numerical method to solve the system described above. This method will involve the Immerse Boundary Method for the fluid solver, where we have to solve Stokes' equations in 2D with an elastic immersed structure (the cell membrane). We will also need to account for movement in the membrane, and discontinuities in quantities of interest. A starting point will be the method presented in [54], which considers a similar system, with a single, uncharged solute.

APPENDIX

A.1 1D Bleb Model Numerical Method

We use the following algorithm to solve the system 1.12-1.19:

1. Solve for a and c at $t + \frac{1}{2}\Delta t$:

$$\frac{c^{n+\frac{1}{2}} - c^n}{\frac{1}{2}\Delta t} = \Omega a^{n+\frac{1}{2}} - c^{n+\frac{1}{2}} \tag{A.1}$$

$$\varepsilon \frac{a^{n+\frac{1}{2}} - a^n}{\frac{1}{2}\Delta t} = \frac{c^{n+\frac{1}{2}}}{1+c^n} \exp\left(\frac{-|x_m^n - x_c^n|}{D}\right) - a^{n+\frac{1}{2}} \exp\left(\frac{|x_m^n - x_c^n|}{F}\right) \tag{A.2}$$

2. Solve for $x_m^{f,b}$, $x_c^{f,b}$, x_N, and u at $t + \frac{1}{2}\Delta t$:

$$\begin{aligned}\left(2D_g + \chi(x_m^{f,n+\frac{1}{2}} - x_m^{b,n+\frac{1}{2}})\right) u^{n+\frac{1}{2}} = &- a^{f,n+\frac{1}{2}}(x_m^{f,n+\frac{1}{2}} - x_c^{f,n+\frac{1}{2}}) \\ &- a^{b,n+\frac{1}{2}}(x_m^{b,n+\frac{1}{2}} - x_c^{b,n+\frac{1}{2}}) \\ &- K_m(x_m^{f,n+\frac{1}{2}} - x_N^{n+\frac{1}{2}} - 1) \\ &- K_m(x_m^{b,n+\frac{1}{2}} - x_N^{n+\frac{1}{2}} + 1)\end{aligned} \tag{A.3}$$

$$\gamma_m \left(\frac{x_m^{f,n+\frac{1}{2}} - x_m^{f,n}}{\frac{1}{2}\Delta t} - u^{n+\frac{1}{2}}\right) = -a^{f,n+\frac{1}{2}}(x_m^{f,n+\frac{1}{2}} - x_c^{f,n+\frac{1}{2}}) - K_m(x_m^{f,n+\frac{1}{2}} - x_N^{n+\frac{1}{2}} - 1) \tag{A.4}$$

$$\gamma_m \left(\frac{x_m^{b,n+\frac{1}{2}} - x_m^{b,n}}{\frac{1}{2}\Delta t} - u^{n+\frac{1}{2}}\right) = -a^{b,n+\frac{1}{2}}(x_m^{b,n+\frac{1}{2}} - x_c^{b,n+\frac{1}{2}}) - K_m(x_m^{b,n+\frac{1}{2}} - x_N^{n+\frac{1}{2}} + 1) \tag{A.5}$$

$$\gamma_c c^{f,n+\frac{1}{2}} \frac{x_c^{f,n+\frac{1}{2}} - x_c^{f,n}}{\frac{1}{2}\Delta t} = a^{f,n+\frac{1}{2}}(x_m^{f,n+\frac{1}{2}} - x_c^{f,n+\frac{1}{2}}) - Mc^{f,n+\frac{1}{2}}(x_c^{f,n+\frac{1}{2}} - x_N^{n+\frac{1}{2}} - b) \tag{A.6}$$

$$\gamma_c c^{b,n+\frac{1}{2}} \frac{x_c^{b,n+\frac{1}{2}} - x_c^{b,n}}{\frac{1}{2}\Delta t} = a^{b,n+\frac{1}{2}}(x_m^{b,n+\frac{1}{2}} - x_c^{b,n+\frac{1}{2}}) - Mc^{b,n+\frac{1}{2}}(x_c^{b,n+\frac{1}{2}} - x_N^{n+\frac{1}{2}} + b) \tag{A.7}$$

$$\gamma_N \frac{x_N^{n+\frac{1}{2}} - x_N^n}{\frac{1}{2}\Delta t} = K_m(x_m^{f,n+\frac{1}{2}} - x_N^{n+\frac{1}{2}} - 1) + K_m(x_m^{b,n+\frac{1}{2}} - x_N^{n+\frac{1}{2}} + 1) + Mc^{f,n+\frac{1}{2}}(x_c^{f,n+\frac{1}{2}} - x_N^{n+\frac{1}{2}} - b) + Mc^{b,n+\frac{1}{2}}(x_c^{b,n+\frac{1}{2}} - x_N^{n+\frac{1}{2}} + b) \tag{A.8}$$

3. Solve for all variables at $t + \Delta t$:

$$\frac{c^{n+1} - c^n}{\Delta t} = \Omega \frac{a^{n+1} + a^n}{2} - \frac{c^{n+1} + c^n}{2} \tag{A.9}$$

$$\varepsilon \frac{a^{n+1} - a^n}{\Delta t} = \frac{\frac{c^{n+1}+c^n}{2}}{1 + c^{n+\frac{1}{2}}} \exp\left(\frac{-|x_m^{n+\frac{1}{2}} - x_c^{n+\frac{1}{2}}|}{D}\right) - \frac{a^{n+1} + a^n}{2} \exp\left(\frac{|x_m^{n+\frac{1}{2}} - x_c^{n+\frac{1}{2}}|}{F}\right) \tag{A.10}$$

$$\begin{aligned}(2D_g + \chi(x_m^{f,n+\frac{1}{2}} - x_m^{b,n+\frac{1}{2}}))u' = &-a^{f,n+\frac{1}{2}}\left(\frac{x_m^{f,n+1} + x_m^{f,n}}{2} - \frac{x_c^{f,n+1} + x_c^{f,n}}{2}\right) \\ &- a^{b,n+\frac{1}{2}}\left(\frac{x_m^{b,n+1} + x_m^{b,n}}{2} - \frac{x_c^{b,n+1} + x_c^{b,n}}{2}\right) \\ &- K_m\left(\frac{x_m^{f,n+1} + x_m^{f,n}}{2} - \frac{x_N^{n+1} - x_N^n}{2} - 1\right) \\ &- K_m\left(\frac{x_m^{b,n+1} + x_m^{f,n}}{2} - \frac{x_N^{n+1} - x_N^n}{2} + 1\right)\end{aligned} \tag{A.11}$$

$$\begin{aligned}\gamma_m\left(\frac{x_m^{f,n+1} - x_m^{f,n}}{\Delta t} - u'\right) = &-a^{f,n+\frac{1}{2}}\left(\frac{x_m^{f,n+1} + x_m^{f,n}}{2} - \frac{x_c^{f,n+1} + x_c^{f,n}}{2}\right) \\ &- K_m\left(\frac{x_m^{f,n+1} + x_m^{f,n}}{2} - \frac{x_N^{n+1} - x_N^n}{2} - 1\right)\end{aligned} \tag{A.12}$$

$$\begin{aligned}\gamma_m\left(\frac{x_m^{b,n+1} - x_m^{b,n}}{\Delta t} - u'\right) = &-a^{b,n+\frac{1}{2}}\left(\frac{x_m^{b,n+1} + x_m^{b,n}}{2} - \frac{x_c^{b,n+1} + x_c^{b,n}}{2}\right) \\ &- K_m\left(\frac{x_m^{b,n+1} + x_m^{b,n}}{2} - \frac{x_N^{n+1} - x_N^n}{2} + 1\right)\end{aligned} \tag{A.13}$$

$$\begin{aligned}\gamma_c c^{f,n+\frac{1}{2}} \frac{x_c^{f,n+1} - x_c^{f,n}}{\Delta t} =& a^{f,n+\frac{1}{2}} \left(\frac{x_m^{f,n+1} + x_m^{f,n}}{2} - \frac{x_c^{f,n+1} + x_c^{f,n}}{2} \right) \\ & - M c^{f,n+\frac{1}{2}} \left(\frac{x_c^{f,n+1} + x_c^{f,n}}{2} - \frac{x_N^{n+1} + x_N^{n}}{2} - b \right)\end{aligned} \tag{A.14}$$

$$\begin{aligned}\gamma_c c^{b,n+\frac{1}{2}} \frac{x_c^{b,n+1} - x_c^{b,n}}{\Delta t} =& a^{b,n+\frac{1}{2}} \left(\frac{x_m^{b,n+1} + x_m^{b,n}}{2} - \frac{x_c^{b,n+1} + x_c^{b,n}}{2} \right) \\ & - M c^{b,n+\frac{1}{2}} \left(\frac{x_c^{b,n+1} + x_c^{f,n}}{2} - \frac{x_N^{n+1} + x_N^{n}}{2} + b \right)\end{aligned} \tag{A.15}$$

We can check convergence, for instance, by running the simulation for a fixed time and comparing the distance d traveled in each case as $\Delta t = 1/2^l$ gets smaller. The order of convergence is then given by

$$\log_2 \left(\frac{|d_{2^l} - d_{2^{l+1}}|}{|d_{2^{l+1}} - d_{2^{l+2}}|} \right) = k \tag{A.16}$$

The result of this is shown in Table A1, given convergence of order 2.

Table A1: The simulation was run to $T = 10.0$, and distance d traveled was compared. This shows the order of convergence is $k \approx 2$. Parameters used here are $\Omega = 40$, $\varepsilon = 0.01$, $D = 0.15$, $F = 0.99$, $M = 0.0081$, $b = 0$, $\gamma_m = 0.8 \times 10^{-3}$, $K_m = 0.1$, $\gamma_N = 10^{-6}$, $\gamma_c = 10^{-4}$, $D_g = 10^{-11}$, $\chi = 10^{-6}$.

l	$\lvert d_{2^l} - d_{2^{l+1}} \rvert$	k
10	$2.8436e-5$	1.7861
11	$8.2452e-6$	1.8330
12	$2.31426e-6$	2.0532
13	$5.5763e-7$	2.1849
14	$1.2263e-7$	2.1732
15	$2.7191e-8$	2.1792
16	$6.0035e-9$	$--$

We may also inspect convergence visually by plotting the solution for each Δt, as shown in

Figure A1.

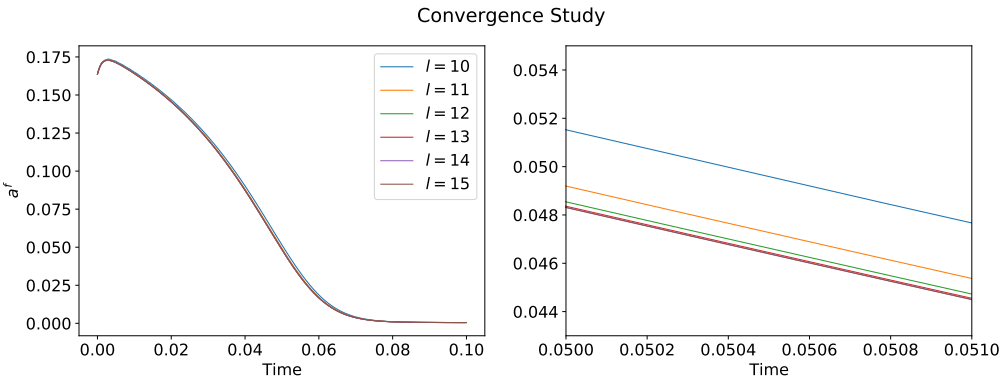

Figure A1: Parameters used here are $\Omega = 40$, $\varepsilon = 0.01$, $D = 0.15$, $F = 0.99$, $M = 0.0081$, $b = 0$, $\gamma_m = 0.8 \times 10^{-3}$, $K_m = 0.1$, $\gamma_N = 10^{-6}$, $\gamma_c = 10^{-4}$, $D_g = 10^{-11}$, $\chi = 10^{-6}$.

A.2 Single Point Dynamics

Consider the following simplification to the system defined by equations 1.12 - 1.19: assume the cell to be symmetric, so that $x_m = x_m^f = -x_m^b$, $x_c = x_c^f = -x_c^b$, $x_N = 0$, and $a = a^f = a^b$, $c = c^f = c^b$. In this case, neglecting fluid drag terms, we get the following force balance equations:

$$0 = a(x_m - x_c) + K_m(x_m - 1) \tag{A.17}$$

$$0 = a(x_m - x_c) - Mc(x_c - b) \tag{A.18}$$

In the particular case where $b = 0$, this recovers a simplified version of the model presented in [26]. Solving for x_m and x_c, we get

$$\begin{aligned} x_m &= \tfrac{(a+Mc)K_m+Mcab}{aMc+aK_m+McK_m}, \\ x_c &= \tfrac{aK_m}{aMc+aK_m+McK_m} + \tfrac{Mca^2b}{(a+Mc)(aMc+aK_m+McK_m)} + \tfrac{Mcb}{a+Mc}, \end{aligned} \tag{A.19}$$

so that the model is reduced to two ODEs:

$$\begin{aligned} \tfrac{\partial c}{\partial t} &= \Omega a - c \\ \varepsilon \tfrac{\partial a}{\partial t} &= \tfrac{c}{1+c} \exp\left(\tfrac{-1}{D}(x_m - x_c)\right) - a\left(\tfrac{1}{F}(x_m - x_c)\right) \end{aligned} \tag{A.20}$$

As presented in [26], this system exhibits four different behaviors: monostable, bistable, oscillatory, and excitable. Sample trajectories of each are shown in Figure A2. Of most interest to us is the excitable regime, where sufficiently large perturbations in the system drive the formation of blebs, rather than immediately returning to steady state.

A.2.1. Single Point Dynamics (Stochastic)

Let

$$g(c, a) = \frac{c}{1+c} \exp\left(-\frac{1}{D} \frac{cMK_m}{aMc + aK_m + cMK_m}\right), \tag{A.21}$$

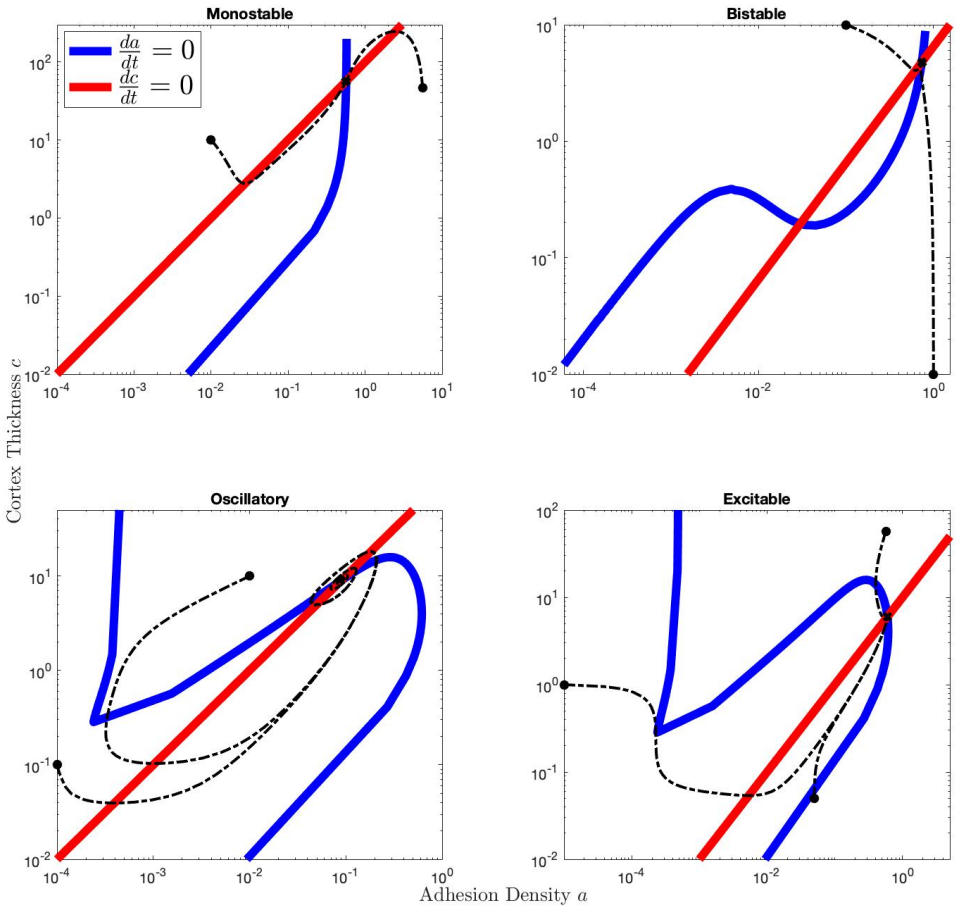

Figure A2: Range of behaviors of the system given different parameter sets, visualized by the nullclines for system A.20. Also plotted are sample paths. The monostable parameters are $\Omega = 100$, $\epsilon = 0.1$, $F = 6.3$, $M = 0.09$, $K_m = 0.08$, and $D = 0.23$. The bistable parameters are $\Omega = 6.5$, $\epsilon = 0.1$, $F = 2.9$, $M = 0.43$, $K_m = 0.016$, and $D = 0.19$. The oscillatory parameters are $\Omega = 100$, $\epsilon = 0.1$, $F = 1$, $M = 0.007$, $K_m = 0.1$, and $D = 0.15$. The excitable parameters are $\Omega = 10$, $\epsilon = 0.1$, $F = 1$, $M = 0.007$, $K_m = 0.1$, and $D = 0.15$. These values were obtained from [26].

$$h(c, a) = a \exp\left(\frac{1}{F} \frac{cMK_m}{aMc + aK_m + cMK_m}\right). \tag{A.22}$$

The Kolmogorov forward equations are given by

$$\frac{\partial p_k}{\partial t} = \hat{g}(c, \alpha(k-1))p_{k-1} - \hat{g}(c, \alpha k)p_k - \hat{h}(c, \alpha k)p_k + \hat{h}(c, \alpha(k+1))p_{k+1}, \tag{A.23}$$

where $\hat{g}$ and $\hat{h}$ are modifications of g and h that we need to determine.

Introduce the rescaled variable $x = \frac{\alpha k}{K}$ and transition rates $\alpha K G(x) = g(c, Kx)$, and $\alpha K H(x) = h(Kx)$. If we multiply both sides by $\frac{\alpha k}{K}$ and summing over k,

$$\frac{\partial}{\partial t}\sum_k p_k = \alpha K \sum_{k=0}^{K}[G(x) - H(x)]p_k. \tag{A.24}$$

In the limit as $K \to \infty$, statistical correlations can be ignored so that we can take the mean-field limit to get a deterministic equation for the fraction x of formed adhesions:

$$\frac{\partial x}{\partial t} = G(x) - H(x). \tag{A.25}$$

Thus,

$$\frac{da}{dt} = \hat{g}(c, a) - \hat{h}(c, a), \tag{A.26}$$

and we recover the original ODE by setting $\hat{g}(c, \alpha k) = \frac{1}{\alpha} g(c, \alpha k)$ and $\hat{h}(c, \alpha k) = \frac{1}{\alpha} h(c, \alpha k)$.

Figure A3 shows stochastic simulations using Gillespie's algorithm for increasing values of k in the ODE case as described in the text. As expected, increasing k gives a closer approximation to the deterministic path.

A.2.2. Mesoscopic Limit

We can also determine the statistical correlation by the system-size expansion [4], [27]. Consider the master equation A.23. If K is sufficiently large but still small enough to have the intrinsic fluctuation, the dynamics of the adhesion density is governed by a stochastic differential equation (SDE). We refer to this equation as the mesoscopic equation. Here we determine the mesoscopic equation by using the system-size expansion.

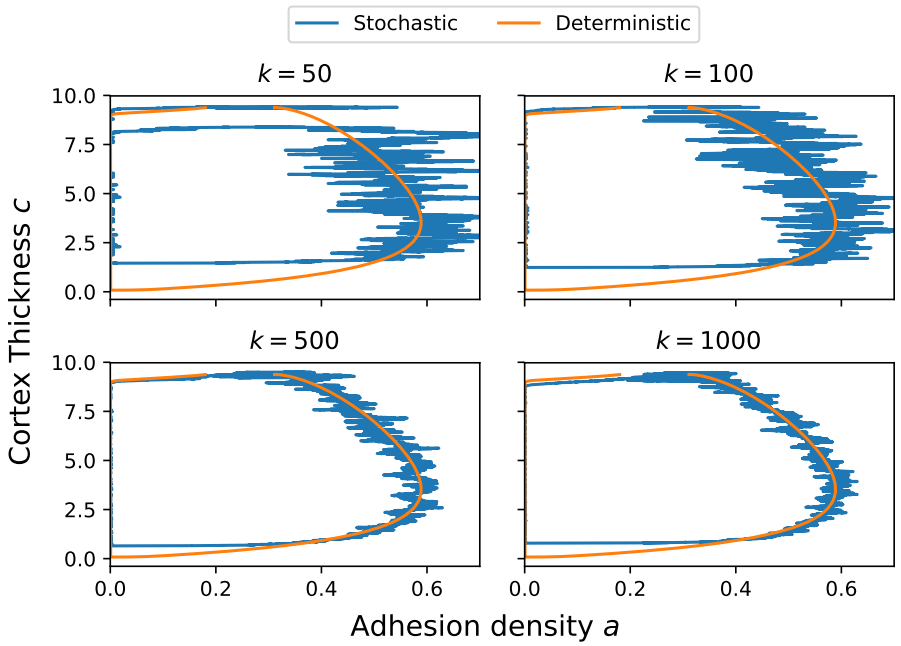

Figure A3: Stochastic simulation of the ODE system A.20, and a sample deterministic path. As k increases, the stochastic path resembles the deterministic path more closely. The parameters here are $\Omega = 30$, $\epsilon = 0.01$, $F = 0.9$, $b = 0$, $M = 0.007$, $K_m = 0.2$, and $D = 0.15$.

The basic idea of the system-size expansion is to set $x = \frac{k}{K}$ and $p_k(t) \to p(x,t)$ treated as a continuous function so that any smooth function $f(x)$ is Taylor expanded by

$$f\left(x - \frac{s}{K}\right) = f(x) - K^{-1}s\frac{\partial f}{\partial x} + \frac{1}{2}K^{-2}s^2\frac{\partial^2 f}{\partial x^2} + \mathcal{O}(K^{-3}). \tag{A.27}$$

Taking

$$\tilde{g}_c(x) = \frac{1}{K}\hat{g}(Kx), \qquad \tilde{h}_c(x) = \frac{1}{K}\hat{h}(Kx), \tag{A.28}$$

and carrying out a Taylor expansion of the master equation A.23 to second order, yields a Fokker-Plank (FP) equation of the Ito form,

$$\partial_t p(x,t) = -\frac{\partial}{\partial x}[\mu_c(x)p(x,t)] + \frac{1}{K}\frac{\partial^2}{\partial x^2}[V_c^2(x)p(x,t)], \tag{A.29}$$

where $\mu_c = \tilde{g}_c - \tilde{h}_c$ and $V_c^2 = \frac{\tilde{g}_c + \tilde{h}_c}{2}$. The FP equation A.29 corresponds to the Ito SDE

$$dX_t = -\mu_c(X_t)dt + \frac{1}{K^{\frac{1}{2}}} V_c(X_t) dW_t. \tag{A.30}$$

Since we desire $\alpha \mu_c \left(\frac{a_t}{\alpha}\right) = g(c,a) - h(c,a)$, we deduce that

$$da_t = -[g(c,a_t) - h(c,a_t)]dt + \frac{1}{K^{\frac{1}{2}}} \sqrt{\frac{\alpha}{2}[g(c,a_t) + h(c,a_t)]} dW_t. \tag{A.31}$$

A.2.3. Modeling a Section of the Membrane

One can extend the single point dynamics to a section of membrane by making a small modification to equation A.32, adding a spatial derivative, so that the simplified system becomes:

$$\frac{\partial c}{\partial t} = \Omega a - c \tag{A.32}$$

$$\epsilon \frac{\partial a}{\partial t} = \frac{c}{1+c} \exp\left(\frac{-|x_m - x_c|}{D}\right) - a \exp\left(\frac{|x_m - x_c|}{F}\right) \tag{A.33}$$

$$0 = a(x_m - x_c) + K_m(x_m - 1) \tag{A.34}$$

$$0 = a(x_m - x_c) - Mc(x_c - b) + \gamma \frac{\partial^2 y_m}{\partial x^2} \tag{A.35}$$

Equations 1.12-1.13 are as before, reproduced here for convenience.

This system allows us to reproduce the result in [26], as shown in Figure A4, and introduce stochasticity, as shown in Figure A5. This is done by applying the same method as for a single point, for multiple individual points along the membrane, each with its own $a - c$ system. However, in this model, the cortex does not move at all, and once the bleb heals, the membrane returns to its reference position, so that the cell does not travel.

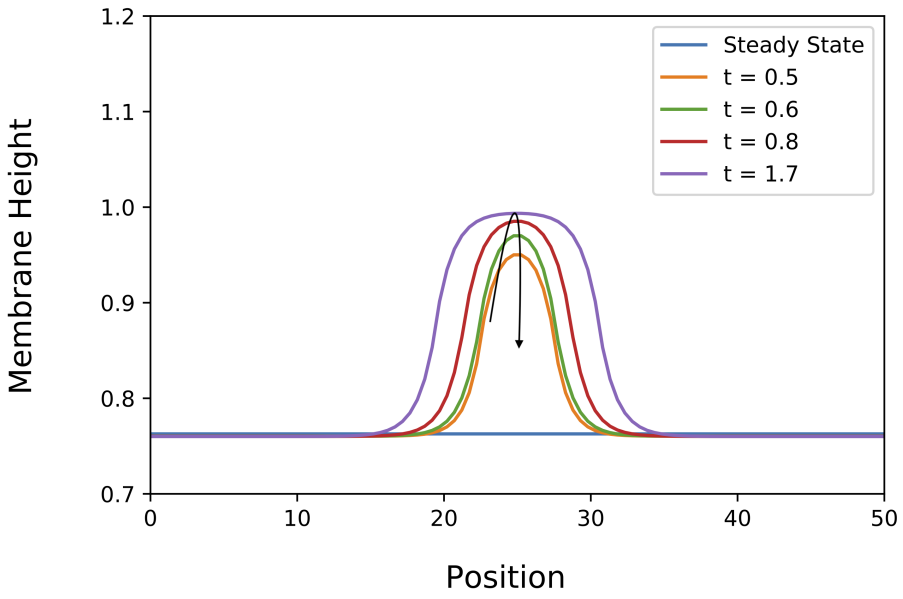

Figure A4: Simulation of the hybrid system A.32. The parameters here are $\gamma = 0.25$, $\Omega = 30$, $\epsilon = 0.01$, $F = 3.0$, $M = 0.007$, $K_m = 0.2$, and $D = 0.15$.

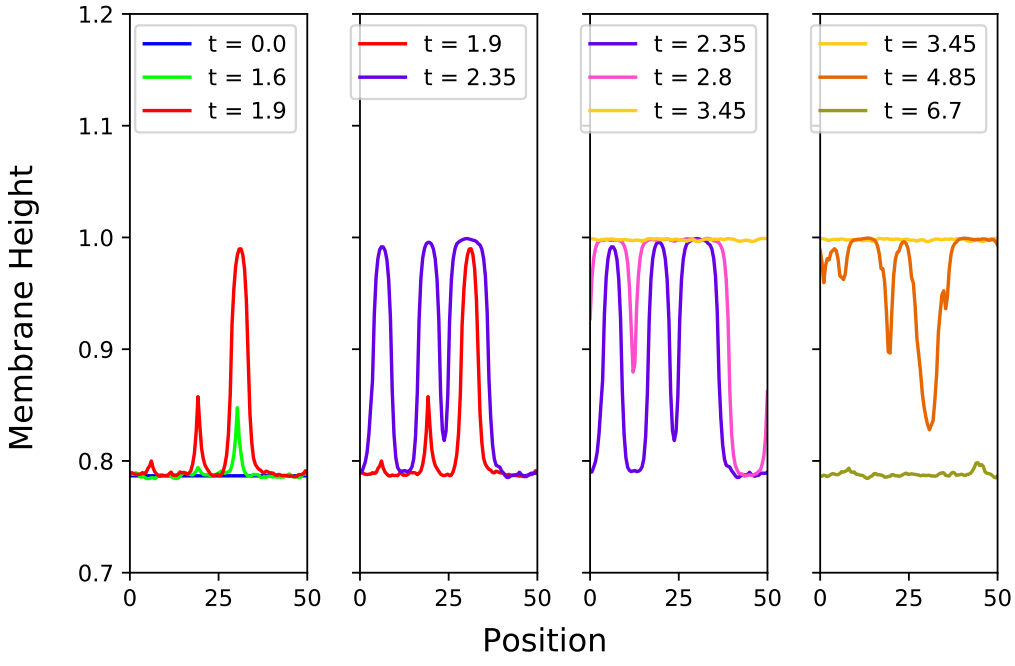

Figure A5: Stochastic simulation of the hybrid system A.32. The parameters here are $\gamma = 0.1$, $\Omega = 30$, $\epsilon = 0.01$, $F = 0.9$, $M = 0.007$, $K_m = 0.2$, and $D = 0.15$. We set $\alpha = 0.3125 \times 10^{-3}$, with steady state value of $a = 0.3125$ (hence $k = 1000$).

A.3 Parameter Study

Figure A6 shows the effect of varying each dimensionless parameter on the distance traveled by the cell, and the duration of the blebbing event. The ranges shown correspond only to the excitable regime.

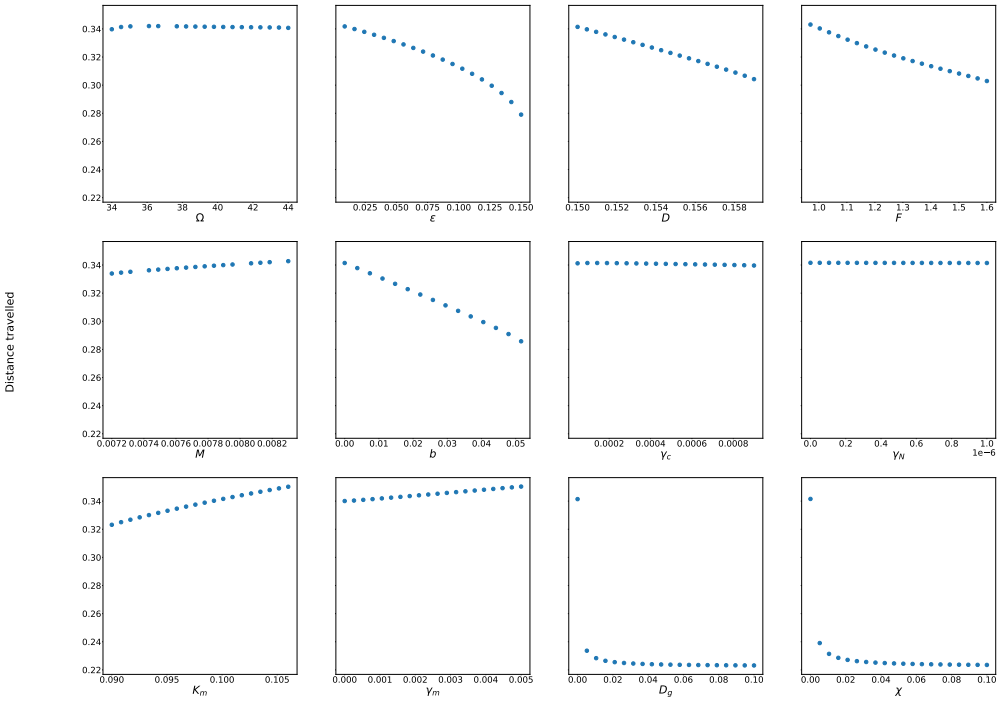

(a)

Figure A7 shows the effect of varying each dimensionless parameter on the distance traveled by the cell. The ranges shown correspond only to the excitable regime.

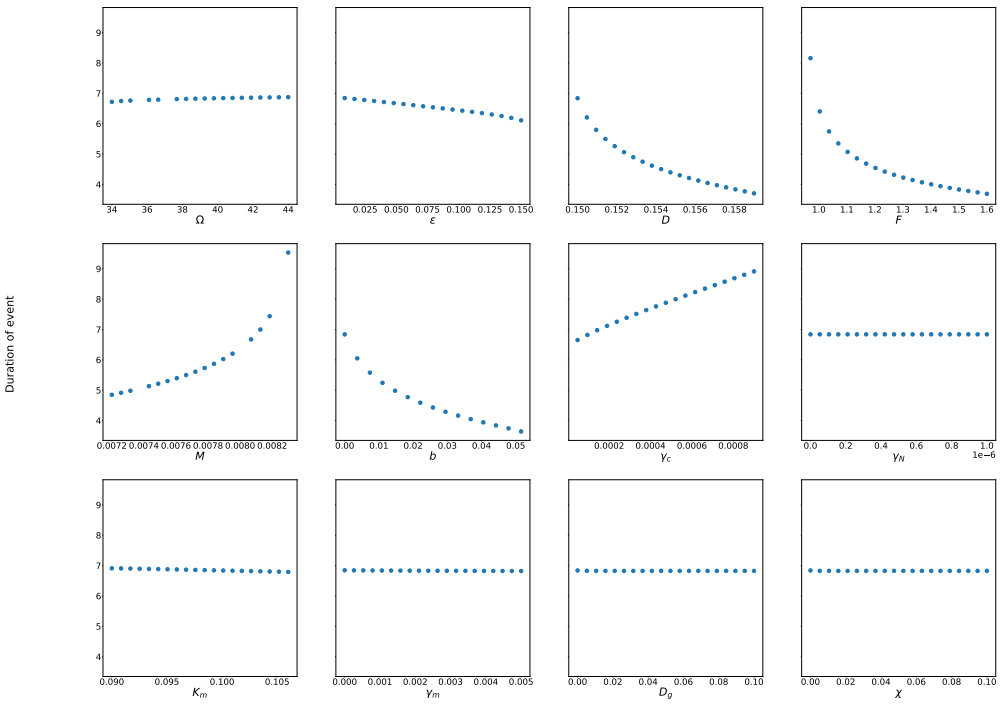

(b)

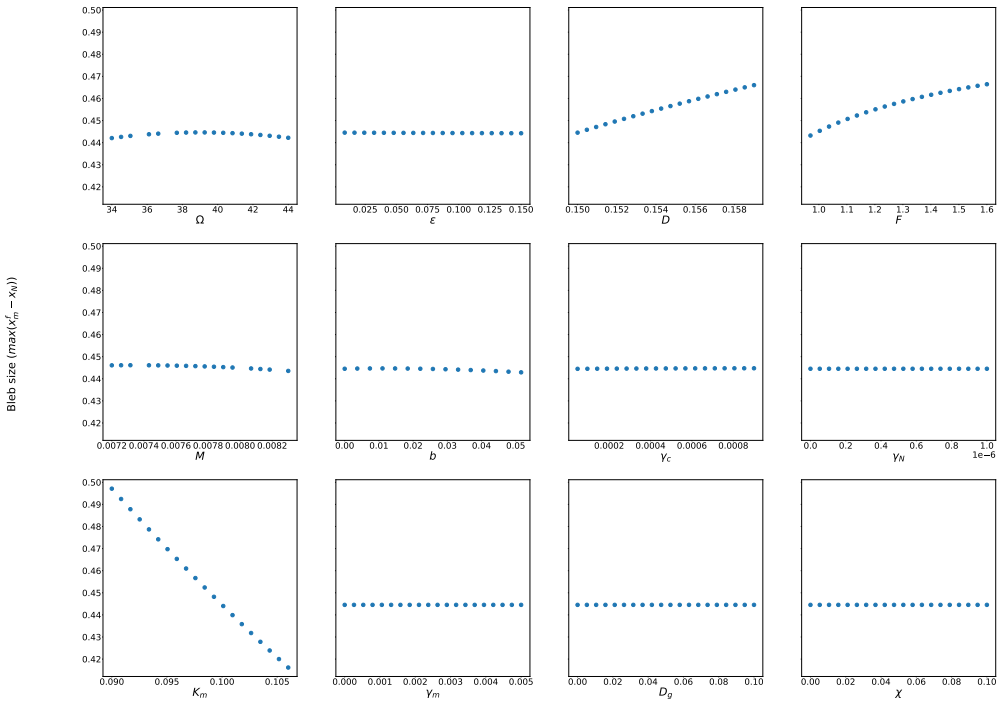

(c)

Figure A6: (a) Distance traveled by the cell upon perturbation. (b) Duration of blebbing event. (c) Bleb size, as measured by the largest difference between x_N and x_m^f (subtracting the steady state separation). In each case, the indicated parameter was varied, and the rest were fixed with the following values: $\Omega = 40$, $\varepsilon = 0.01$, $D = 0.15$, $F = 0.99$, $M = 0.0081$, $b = 0$, $\gamma_m = 0.8 \times 10^{-3}$, $K_m = 0.1$, $\gamma_N = 10^{-6}$, $\gamma_c = 10^{-4}$, $D_g = 10^{-11}$, $\chi = 10^{-6}$.

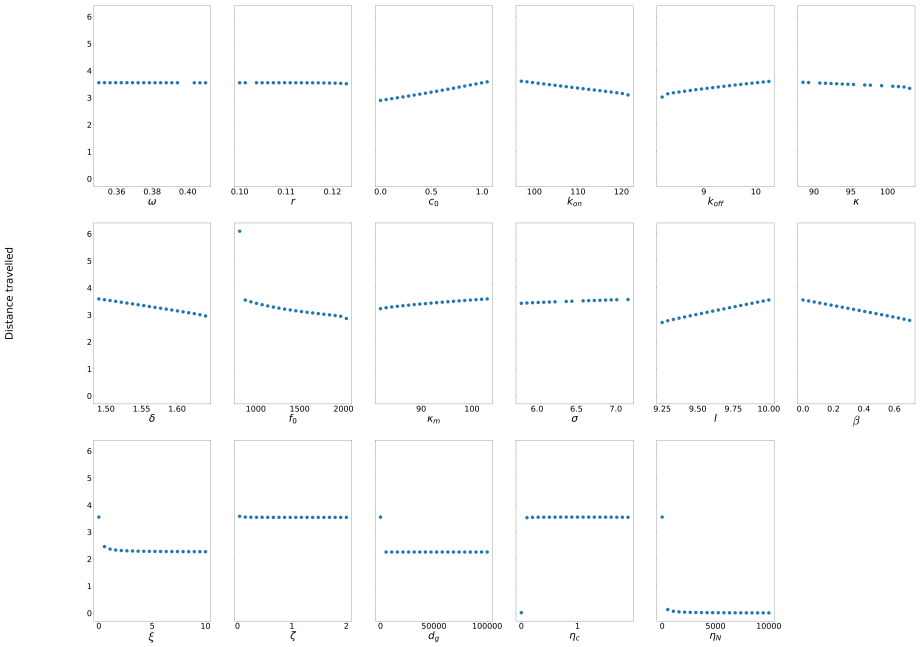
Distance travelled
ω
r
c_0
k_{on}
k_{off}
κ
δ
f_0
κ_m
σ
l
β
ξ
ζ
d_p
η_c
η_N

(a)

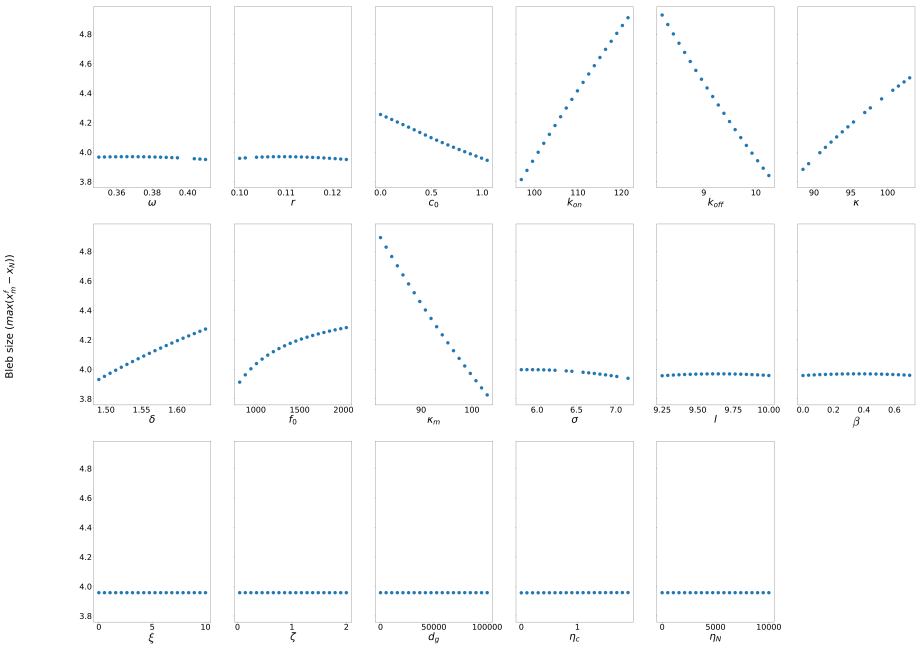

(b)

Figure A7: (a) Distance traveled by the cell upon perturbation. (b) Bleb size, as measured by the largest difference between x_N and x_m^f (subtracting the steady state separation). In each case, the indicated parameter was varied, and the rest were fixed with the following values: $\omega = 0.4$, $r = 0.1$, $k_{on} = 100$, $k_{off} = 10$, $c_0 = 1$, $\delta = 1.5$, $\kappa = 90$, $f_0 = 873$, $\xi = 10^{-4}$, $\kappa_m = 100$, $d_g = 10^{-7}$, $\zeta = 0.14$, $\sigma = 6.93$, $\beta = 0$, $l = 10$, $\eta_c = 0.9$, $\eta_N = 0.009$.

APPENDIX

B.1 Deriving the Equations for CO_2

The equations for CO_2 must satisfy the following conditions:

$$\pi_w j_w + \mu \geq 0, \tag{B.1}$$

and for $c \sim c^e$ we must have

$$\frac{d}{dt}\begin{bmatrix} vc \\ v \end{bmatrix} = -\begin{bmatrix} j \\ j_w \end{bmatrix} = \begin{bmatrix} L_{11} & L_{12} \\ L_{21} & L_{22} \end{bmatrix}\begin{bmatrix} \mu \\ \pi_w \end{bmatrix} \tag{B.2}$$

where L is a positive definite matrix with entries L_{ij}. For notational simplicity, we use $c = c_{CO_2}$. We have

$$\pi_w = c^e - c - \frac{A}{v}, \qquad \mu = \ln\left(\frac{c}{c^e}\right). \tag{B.3}$$

We set

$$\begin{aligned} \frac{d}{dt}(vc) &= -k(c - c^e) + \frac{c + c^e}{2} l \frac{dv}{dt}, \\ \frac{dv}{dt} &= -\zeta\left(\sigma(c^e - c) - \frac{A}{v}\right), \end{aligned} \tag{B.4}$$

where l is a constant to be determined. Now, we can rewrite B.4 as

$$\begin{aligned} \frac{d(vc)}{dt} &= -\left(k + \frac{1}{2}(c + c^e)l\zeta(1 - \sigma)\right)(c - c^e) - \frac{1}{2}(c + c^e)l\zeta\pi_w, \\ \frac{dv}{dt} &= -\zeta((1 - \sigma)(c - c^e)) - \zeta\pi_w. \end{aligned} \tag{B.5}$$

Then,

$$\frac{d}{dt}\begin{bmatrix} vc \\ v \end{bmatrix} = -\begin{bmatrix} k + \frac{1}{2}(c + c^e)l\zeta(1 - \sigma)\frac{c - c^e}{\ln\frac{c}{c^e}} & \frac{1}{2}(c + c^e)l\zeta \\ \zeta(1 - \sigma)\frac{c - c^e}{\ln\frac{c}{c^e}} & \zeta \end{bmatrix}\begin{bmatrix} \ln\frac{c}{c^e} \\ \pi_w \end{bmatrix}. \tag{B.6}$$

We require $L_{12} = L_{21}$ as $c \to c^e$. Since

$$\frac{c - c^e}{\ln \frac{c}{c^e}} = \left(\frac{d}{dc} \ln c_{c_e} \right)^{-1} = c^e \text{ as } c \to c^e, \tag{B.7}$$

$$\zeta(1-\sigma)c^e = c^e l \zeta, \tag{B.8}$$

and

$$l = (1-\sigma). \tag{B.9}$$

To symmetrize L, we take the average of L_{12} and L_{21}:

$$L_s = \begin{bmatrix} k + \frac{1}{2}\bar{c}\zeta(1-\sigma^2)\hat{c} & \frac{1}{2}(\bar{c}+\hat{c})(1-\sigma)\zeta \\ \frac{1}{2}(\bar{c}+\hat{c})(1-\sigma)\zeta & \zeta \end{bmatrix} \tag{B.10}$$

with

$$\bar{c} = \frac{c + c^e}{2}, \qquad \hat{c} = \frac{c - c^e}{\ln \frac{c}{c^e}}. \tag{B.11}$$

Then

$$\det L_s = k\zeta - \frac{1}{4}(\bar{c} - \hat{c})^2(1-\sigma)^2\zeta. \tag{B.12}$$

We need $\det L \geq 0$, so we must set $\bar{c} = \hat{c}$. Note that these are approximately equal, and so our equations are

$$\begin{aligned} \frac{d}{dt}(vc) &= -k(c - c^e) + \frac{c - c^e}{\ln \frac{c}{c^e}}(1-\sigma)\frac{dv}{dt}, \\ \frac{dv}{dt} &= -\zeta \left(\sigma(c^e - c) - \frac{A}{v} \right). \end{aligned} \tag{B.13}$$

APPENDIX

C.1 Parameter Values

Parameters	Descriptions	Values	Sources
R (J/mol K)	Ideal gas constant	8.31451	Constant
T (K)	Absolute temperature	300	Constant
F (sA/mol)	Faraday constant	96485.3329	Constant
v_0 (L)	Initial Volume	$2 * 10^{-12}$	Assumed
c^e_{0,Na^+} (mM)	Extracellular concentration of Na^+	140	Ref.[18]
c^e_{0,K^+} (mM)	Extracellular concentration of K^+	5	Ref. [18]
c^e_{0,Cl^-} (mM)	Extracellular concentration of Cl^-	125	Ref. [18]
c^e_{0,H^+} (M)	Extracellular concentration of H^+	$10^{-7.4}$	Ref. [18]
c^e_{0,HCO_3^-} (mM)	Extracellular concentration of HCO_3^-	25	Ref. [18]
c^e_{0,CO_2} (M)	Extracellular concentration of CO_2	$10^{-7.2}$	Estimate
c^i_{0,Na^+} (mM)	Intracellular concentration of Na^+	10	Ref. [18]
c^i_{0,K^+} (mM)	Intracellular concentration of K^+	140	Ref. [18]
c^i_{0,Cl^-} (mM)	Intracellular concentration of Cl^-	40	Ref. [18]
c^i_{0,H^+} (M)	Intracellular concentration of H^+	$10^{-7.2}$	Ref. [18]
c^i_{0,HCO_3^-} (mM)	Intracellular concentration of HCO_3^-	20	Ref. [18]
c^i_w (M)	Intracellular concentration of water	55	Constant
c^i_{0,CO_2} (M)	Intracellular concentration of CO_2	10^{-7}	Estimate
A (mM)	Concentration of impermeable anions	90	Assumed

z_{Na}	Valence of Na^+	$+1$	Constant
z_K	Valence of K^+	$+1$	Constant
z_{Cl}	Valence of Cl^-	-1	Constant
z_{H^+}	Valence of H^+	1	Constant
$z_{HCO_3^-}$	Valence of HCO_3^-	-1	Constant
z	Average valence of anions	-1	Assumed
g_{Na^+} ($mol^2/Kg/m^3$)	Passive Na^+ channel constant	7.5×10^{-9}	Ref. [23]
g_{K^+} ($mol^2/Kg/m^3$)	Passive K^+ channel constant	2.5×10^{-7}	Ref. [23]
g_{Cl^-} ($mol^2/Kg/m^3$)	Passive Cl^- channel constant	1.25×10^{-7}	Ref.[23]
g_{H^+} ($mol^2/Kg/m^3$)	Passive H^+ channel constant	1.00×10^{-9}	Estimate
$g_{HCO_3^-}$ ($mol^2/Kg/m^3$)	Passive HCO_3^- channel constant	1.00×10^{-8}	Estimate
K_{Na^+} (mM)	Dissociation constant for Na^+	100	Ref. [46]
K_{H^+} (μM)	Dissociation constant for H^+	0.5	Ref. [46]
K_{Cl^-} (mM)	Dissociation constant for Cl^-	10	Ref. [46]
$K_{HCO_3^-}$ (mM)	Dissociation constant for HCO_3^-	1	Ref. [46]
$G_{Na^+H^+}$ ($mol/s/m^2$)	Permeability of Na^+/H^+ antiporter	5×10^{-14}	Ref. [46]
$G_{Cl^-HCO_3^+}$ ($mol/s/m^2$)	Permeability of Cl^-/HCO_3^- antiporter	1.5×10^{-12}	Ref. [46]
ζ (m/s/Pa)	Water permeability constant	3.0×10^{-11}	Ref. [23]
k_1 ($M/s/m^2$)	Forward reaction rate	3×10^{-2}	Ref. [12]

k_{-1} (M/s/m^2)	Backward reaction rate	12	Ref. [12]
σ	Reflection coefficient for CO_2	0.45	Estimate
k (cm^3/s)	Constant for CO_2	$1.87 \times 10^{-}20$	Estimate
G_p (mol/V/s/m^2)	Permeability coefficient for Na-K ATPase	4.38×10^{-5}	Ref. [46]
K_{pNa} (mM)	Saturation constant for intracellular Na	25	Ref. [46]
K_{pK} (mM)	Saturation constant for intracellular K	1.4	Ref. [46]
P_s (m/V/s/M^{-3})	Permeability coefficient for NKCC	5.26×10	Ref. [17]
K^s_K (mM)	Saturability value for intracellular K	7.5	Ref. [17]
K^s_{Na} (mM)	Saturability value for intracellular Na	3.8	Ref. [17]
K^s_{Cl} (mM)	Saturability value for intracellular Cl	26	Ref. [17]

BIBLIOGRAPHY

[1] M. Biro, Y. Romeo, S. Kroshwald, M. Bovellan, A. Boden, J. T. Tcherkezian, P. P. Roux, G. Charras, and E. K. Paluch. Cell Cortex Composition and Homeostasis Resolved by Integrating Proteomics and Quantitative Imaging. *Cytoskeleton*, 70(741–754), 2013.

[2] H. Blaser, M. Reichman-Fried, I. Castanon, K. Dumstrei, F. L. Marlow, K. Kawakami, L. Solnica-Krezel, C.-P. Heisenberg, and E. Raz. Migration of Zebrafish Primordial Germ Cells: A Role for Myosin Contraction and Cytoplasmic Flow. *Developmental Cell*, 11(5):613–627, Nov. 2006.

[3] W. J. Brackenbury and M. Yang. Membrane potential and cancer progression. *Frontiers in Physiology*, 4:1–10, July 2013.

[4] P. C. Bressloff. *Stochastic Processes in Cell Biology.* Springer, New York, 2014.

[5] P. C. Bressloff and H. Kim. Search-and-capture model of cytoneme-mediated morphogen gradient formation. *Physical Review E*, 99(5):052401, 2019.

[6] G. T. Charras, M. Coughlin, T. J. Mitchison, and L. Mahadevan. Life and Times of a Cellular Bleb. *Biophysical Journal*, 94(5):1836–1853, Mar. 2008.

[7] G. T. Charras, C.-K. Hu, M. Coughlin, and T. J. Mitchison. Reassembly of contractile actin cortex in cell blebs. *Journal of Cell Biology*, 175(3):477–490, Nov. 2006.

[8] G. T. Charras and E. K. Paluch. Blebs lead the way: how to migrate without lamellipodia. *Nature Reviews Molecular Cell Biology*, 9:730–736, Sept. 2008.

[9] J. G. Cyster and S. R. Schwab. Sphingosine-1-Phosphate and Lymphocyte Egree from Lymphoid Organs. *Annual Review of Immunology*, 30:69–94, 2012.

[10] G. Danuser, J. Allard, and A. Mogilner. Mathematical Modeling of Eukaryotic Cell Migration: Insights Beyond Experiments. *Annual Review of Cell and Developmental Biology*, 29(1):501–528, Oct. 2013.

[11] J. L. Doob. Renewal theory from the point of view of the theory of probability. *Transactions of the American Mathematical Society*, 63(3):422–438, 1948.

[12] W. Dreybrodt, J. Lauckner, L. Zaihua, U. Svensson, and D. Buhmann. The kinteics of the reaction $C0_2 + H_2O \rightarrow H^+ + HCO_3^-$ as one of the rate limiting steps for the dissolution of calcite in the system $H_2O - C0_2 - CaCO_3$. *Geochimica et Cosmochimica Acta*, 60:3375–3381, May 1996.

[13] L. Dupré, R. Houmadi, C. Tang, and J. Rey-Barroso. T Lymphocyte Migration: An Action Movie Starring the Actin and Associated Actors. *Frontiers in Immunology*, 6(10):1704, Nov. 2015.

[14] O. T. Fackler and R. Grosse. Cell motility through plasma membrane blebbing. *Journal of Cell Biology*, 181(6):879–884, June 2008.

[15] M. I. Freidlin and A. D. Wentzell. *Random perturbations of dynamical systems.* Springer, 1998.

[16] M. Fritzsche, R. Thorogate, and G. Charras. Quantitative Analysis of Ezrin Turnover Dynamics in the Actin Cortex. *Biophysical Journal*, 106(2):343–353, Jan. 2014.

[17] T. Hartmann and A. S. Verkman. Model of ion transport regulation in chloride-secreting airway epithelial cells. *Biophysical Journal*, 58(2):391–401, Aug. 1990.

[18] T. J. Jentsch. VRACs and other ion channels and transporters in the regulation of cell volume and beyond. *Nature Publishing Group*, 17(5):293–307, Apr. 2016.

[19] J. P. Keener and J. M. Newby. Perturbation analysis of spontaneous action potential initiation by stochastic ion channels. *Physical Review E*, 84(1):011918, 2011.

[20] I. Khovanov, A. Polovinkin, D. Luchinsky, and P. McClintock. Noise-induced escape in an excitable system. *Physical Review E*, 87(3):032116, 2013.

[21] Y. Li, J. Graham, C. Wolgemuth, D. Wirtz, and S. X. Sun. Going with the Flow: Water Flux and Cell Shape During Cytokinesis. *Proceedings of the National Academy of Sciences*, 104(51):20167–20172, Dec. 2007.

[22] Y. Li, Y. Mori, and S. X. Sun. Flow-Driven Cell Migration under External Electric Fields. *Physical Review Letters*, 115(26):211, Dec. 2015.

[23] Y. Li, Y. Mori, and S. X. Sun. Flow-Driven Cell Migration under External Electric Fields. *Physical Review Letters*, 115(26):211, Dec. 2015.

[24] F. Y. Lim, K. H. Chiam, and L. Mahadevan. The size, shape, and dynamics of cellular blebs. *EPL*, 100:1–6, Oct. 2012.

[25] P. Macklin and J. S. Lowengrub. A New Ghost Cell/Level Set Method for Moving Boundary Problems: Application to Tumor Growth. *Journal of Scientific Computing*, 35(2-3):266–299, Feb. 2008.

[26] K. Manakova, H. Yan, J. Lowengrub, and J. Allard. Cell Surface Mechanochemistry and the Determinants of Bleb Formation, Healing, and Travel Velocity. *Biophysical Journal*, 110(7):1636–1647, Apr. 2016.

[27] A. J. McKane, T. Biancalani, and T. Rogers. Stochastic pattern formation and spontaneous polarisation: the linear noise approximation and beyond. *Bull of Math Biol*, 76:895–921, 2014.

[28] Y. Mori. Mathematical Properties of Pump-Leak Models of Cell Volume Control. *Journal of Mathematical Biology*, 64:873–916, Oct. 2012.

[29] Y. Mori. A Multidomain Model for Ionic Electrodiffusion and Osmosis with an Application to Cortical Spreading Depression. *Physica D: Nonlinear Phenomena*, 308:94–108, July 2015.

[30] Y. Mori. A Model of Cell Movement incorporating Osmosis and Actin Polymerization. pages 1–6, Mar. 2017.

[31] Y. Mori, C. Liu, and R. S. Eisenberg. A Model of Electrodiffusion and Osmotic Water Flow and its Energetic Structure. *Physica D: Nonlinear Phenomena*, 240:1835–1852, Sept. 2011.

[32] J. M. Newby, P. C. Bressloff, and J. P. Keener. Breakdown of fast-slow analysis in an excitable system with channel noise. *Physical review letters*, 111(12):128101, 2013.

[33] E. Paluch, M. Piel, J. Prost, M. Bornens, and C. Sykes. Cortical Actomyosin Breakage Triggers Shape Oscillations in Cells and Cell Fragments. *Biophysical Journal*, 89(1):724–733, July 2005.

[34] E. K. Paluch and E. Raz. The role and regulation of blebs in cell migration. *Current Opinion in Cell Biology*, 25(5):582–590, Oct. 2013.

[35] C. Peskin. The immersed boundary method. *Acta Numerica*, 11:479 – 517, 2002.

[36] C. Poignard, A. Silve, F. Campion, L. M. Mir, O. Saut, and L. Schwartz. Ion fluxes, transmembrane potential, and osmotic stabilization: a new dynamic electrophysiological model for eukaryotic cells. *European Biophysics Journal*, 40(3):235–246, Nov. 2010.

[37] B. N. Roberts and D. J. Christini. NHE Inhibition Does Not Improve Na+ or Ca2+ Overload During Reperfusion: Using Modeling to Illuminate the Mechanisms Underlying a Therapeutic Failure. *PLoS Computational Biology*, 7(10):e1002241, Oct. 2011.

[38] T. F. Robertson, P. Chengappa, D. Gomez Atria, C. F. Wu, L. Avery, N. H. Roy, I. Maillard, R. J. Petrie, and J. K. Burkhardt. Lymphocyte egress signal sphingosine-1-phosphate promotes ERM-guided, bleb-based migration. *Journal of Cell Biology*, 220(6), Mar. 2021.

[39] V. Ruprecht, S. Wieser, A. Callan-Jones, M. Smutny, H. Morita, K. Sako, V. Barone, M. Ritsch-Marte, M. Sixt, R. Voituriez, and C.-P. Heisenberg. Cortical Contractility Triggers a Stochastic Switch to Fast Amoeboid Cell Motility. *Cell*, 160(4):673–685, Feb. 2015.

[40] M. Schaks, G. Giannone, and K. Rottner. Actin Dynamics in Cell Migration. *Essays in Biochemistry*, 63(5):483–495, Sept. 2019.

[41] Z. Schuss. *Theory and applications of stochastic processes: an analytical approach*, volume 170. Springer Science & Business Media, 2009.

[42] A. Schwab, A. Fabian, P. J. Hanley, and C. Stock. Role of Ion Channels and Transporters in Cell Migration. *Physiological Reviews*, 92(4):1865–1913, Oct. 2012.

[43] A. Schwab, A. Fabian, P. J. Hanley, and C. Stock. Role of Ion Channels and Transporters in Cell Migration. *Physiological Reviews*, 92(4):1865–1913, Oct. 2012.

[44] D. Shao, H. Levine, and W.-J. Rappel. Coupling actin flow, adhesion, and morphology in a computational cell motility model . *PNAS*, pages 1–6, Apr. 2012.

[45] E. M. Smith, J. Hennen, Y. Chen, and J. D. Mueller. In Situ Quantification of Protein Binding to the Plasma Membrane. *Biophysical Journal*, 108(11):2648–2657, June 2015.

[46] Y. Sohma, M. A. Gray, Y. Imai, and B. E. Argent. A Mathematical Model of the Pancreatic Ductal Epithelium. *The Journal of Membrane Biology*, 154:53–67, Nov. 1996.

[47] W. Strychalski and R. D. Guy. A computational model of bleb formation. *Mathematical Medicine and Biology*, 30(2):115–130, June 2013.

[48] W. Strychalski and R. D. Guy. Intracellular Pressure Dynamics in Blebbing Cells. *Biophysical Journal*, 110(5):1168–1179, Jan. 2016.

[49] J. Tao, Y. Li, D. K. Vig, and S. X. Sun. Cell Mechanics: A Dialogue. pages 1–18, Oct. 2016.

[50] H. Tasnim, G. M. Fricke, J. R. Byrum, J. O. Sotiris, J. L. Cannon, and M. E. Moses. Quantitative Measurement of naïve T cell association With Dendritic cells, Frcs, and Blood Vesselsin lymph nodes. *Frontiers in Immunology*, 9:1–13, July 2018.

[51] J.-Y. Tinevez, U. Schulze, G. Salbreux, J. Roensch, J.-F. Joanny, and E. Paluch. Role of cortical tension in bleb growth. *PNAS*, 106:18581–18586, Nov. 2009.

[52] P. G. Vallés, V. Bocanegra, A. Gil Lorenzo, and V. V. Costantino. Physiological Functions and Regulation of the Na^+/H^+ Exchanger [NHE1] in Renal Tubule Epithelial Cells. *Kidney and Blood Pressure Research*, 40(5):452–466, Oct. 2015.

[53] A. M. Weinstein. A Kinetically Defined Na +/H + Antiporter within a Mathematical Model of the Rat Proximal Tubule. *Journal of General Physiology*, 105:617–641, May 1995.

[54] L. Yao and Y. Mori. A numerical method for osmotic water flow and solute diffusion with deformable membrane boundaries in two spatial dimension. *Journal of Computational Physics*, 350:728–746, Mar. 2017.

[55] L. Yizeng, L. Yao, Y. Mori, and S. X. Sun. On the energy efficiency of cell migration in diverse physical environments. *PNAS*, 116:23894–23900, Nov. 2019.

[56] E. Zatulovskiy, R. Tyson, T. Bretschneider, and R. R. Kay. Bleb-driven chemotaxis of Dictyostelium cells. *Journal of Cell Biology*, 204(6):1027–1044, Mar. 2014.